



Title	Study of the regional climatic impacts of tropical explosive volcanism in the Middle East and North Africa region
Author(s)	Muhammad Mubashar Ahmad Dogar
Citation	北海道大学. 博士(環境科学) 乙第7091号
Issue Date	2020-03-25
DOI	10.14943/doctoral.r7091
Doc URL	<a href="http://hdl.handle.net/2115/78553">http://hdl.handle.net/2115/78553</a>
Type	theses (doctoral)
File Information	Muhammad_Dogar.pdf



[Instructions for use](#)

**Study of the regional climatic impacts of tropical explosive volcanism in the  
Middle East and North Africa region**

(熱帯の爆発的火山活動が中東および北アフリカの地域気候に与える影響  
に関する研究)

Dissertation by

**Muhammad Mubashar Ahmad Dogar**

In Partial Fulfillment of the Requirements

For the Degree of

**Doctor of Philosophy**

Hokkaido University, Sapporo, Japan

March 2020

All Rights Reserved

## **ABSTRACT**

### **Study of the regional climatic impacts of tropical explosive volcanism in the Middle East and North Africa region**

**Muhammad Mubashar Ahmad Dogar**

Explosive volcanism is considered as a strong climate forcing with profound global and regional scale direct and indirect radiative impacts. The direct radiative effects of volcanic eruptions resulting in solar dimming, surface cooling and reduction in rainfall are well documented. However, volcanic eruptions also cause indirect climatic impacts that are not well understood. For example, solar dimming induced by volcanic aerosols could cause changes to the updraft branch of Hadley circulation that in turn largely affect surface temperature, evaporation, and precipitation patterns especially in monsoon fed regions such as the Middle Eastern, African, and South Asian tropical rain belt regions. Therefore, understanding the sensitivity of Hadley circulation to volcanism and associated regional impacts is essential, as the Hadley circulation is directly related to the precipitation changes in the tropics and with other large-scale circulations. Likewise, volcanic-induced radiative perturbations potentially interact and modulate the leading teleconnection modes such as El Nino Southern Oscillation and North Atlantic Oscillation that strongly affect global and regional climate. Hence, quantification of magnitude and spatial pattern of these postvolcanic direct and indirect climatic responses is important for a better understanding of climate variability and changes, especially in the tropical rain belt regions.

In earlier literature it is noticed that the studies dealing with volcanism have matured in terms of their global climatic impacts; however, uncertainties remain in their regional impacts. Therefore, the main aim of this research is to improve our understanding of the regional climatic impacts driven by volcanism, especially in the Middle East and North Africa (MENA) region. This study focused on the MENA region, as this region appears to be very sensitive to the effects caused by explosive volcanism. For instance, the winter cooling in the MENA region following the 1991 Pinatubo eruption far exceeded the mean hemispheric temperature anomaly, even causing snowfall in most parts of the Arabian Peninsula region. Similarly, previous studies also reported that the strong volcanic eruptions diminished the solar radiation to such an extent that the resulting cooling caused crops to shrivel and produced famine in Africa and Egypt. Several earlier studies have documented this cooling anomaly over the Middle East after large eruptions with snowy conditions over the Gulf of Aqaba and pointed out that this cooling response is produced as a result of the direct radiative impact of volcanism. However, there is rarely any studies available that looked at the changes caused as a result of the dynamic response of post-eruption circulation changes over MENA, such as caused

by post-eruption El Niño Southern Oscillation, North Atlantic Oscillation, and Indian monsoon changes, and therefore, this dissertation investigated both the volcanic direct radiative impacts and post-eruption circulation impacts (i.e., indirect response) over the MENA region.

A better understanding of volcanic eruption's impact on the global and regional climate allows scientists to better account for the relative contributions of natural and human-induced factors on the long-term warming trends. This suggests that for a better assessment of the climate variations, one needs to consider the contribution caused by major explosive eruptions in our climate system.

For this purpose, I choose the two strongest low-latitude tropical eruptions of the late 20th century, El Chichón of 1982 and Pinatubo of 1991 occurred in the satellite era, which have better observational records. Hence, to better understand MENA climate variability, the climate responses to the El Chichón and Pinatubo volcanic eruptions are analyzed using observations, reanalysis data, and output from the Geophysical Fluid Dynamics Laboratory's High-Resolution Atmospheric Model (HiRAM) with the effectively 50-km and 25-km horizontal grid spacing. This high-resolution modeling technique ensures ample grid resolution for regional climate analysis with the ability to better account for global and regional responses to volcanic direct radiative and circulation impacts. A multiple regression analysis both for the observations and the model output is performed on seasonal summer and winter composites to separate out the contributions from climate trends, El Niño Southern Oscillation (ENSO), North Atlantic Oscillation (NAO), Indian summer monsoon, and volcanic aerosols.

Strong regional temperature and precipitation responses over the MENA region are found in both winter and summer. This study shows that the Northern hemisphere tropical volcanism produces a significant reduction in rainfall and concomitant drought conditions over the Sahel region by weakening the land-sea thermal gradient in boreal summer. Post eruption changes of ENSO and Indian monsoon amplifies the rainfall deficit by shifting the ITCZ southward in the boreal summer. The model and the observations both show that the volcanic-induced positive phase of NAO amplifies post-eruption cooling over MENA in winter. The HiRAM results are consistent with observations in general, however, it underestimates post-eruption NAO and ENSO responses and associated climatic impacts over MENA in winter. This study confirms that the MENA and South Asian climate regime responds vigorously to direct and indirect (through circulation changes) impacts of explosive volcanism. The conducted analysis sheds light on the internal mechanisms of MENA climate variability and helps to selectively diagnose the model deficiencies.

This dissertation develops a sound understanding of the direct and indirect radiative impacts of tropical volcanic eruptions over the MENA region in the winter and summer seasons. In this study, a unified framework that combines the use of high-resolution modeling and multiple regression approach is developed. This study analyzes specifically designed climate model simulations to account for the regional impacts of El Chichón and Pinatubo eruptions. This framework illuminates

the amplified cooling responses over the Arabian Peninsula in winter and volcanic-induced weakening of African monsoon and associated drought conditions over the tropical rain-belt regions of MENA in the summer season. It clarifies the gaps in earlier studies and answers why eruptions caused strong cooling anomalies in winter over the MENA region. Moreover, this study also sheds light on the shift of ITCZ in the summer season that significantly impacts monsoonal precipitation. This improved understanding is expected to advance climate model simulations to account for circulation impacts caused by strong tropical volcanic eruptions. It will help the climate community to better simulate the regional impacts of volcanism. Moreover, it could be very useful for studies dealing with solar radiation management and geoengineering applications.

## **DEDICATION**

To my parents, Saeeda Begum and Muhammad Shafi Dogar

## ACKNOWLEDGEMENTS

I want to take this opportunity to express my sincere gratitude and thanks to the Japanese Society for Promotion of Science (JSPS)'s officials, who believed in my abilities and provided me financial support to conduct this research. My selection as a JSPS RONPAKU Fellow enabled me to achieve my dream and provided me the best environment; mentorship and research facilities required for pursuing higher studies leading to a Ph.D. degree.

First and foremost, I would like to thank my Ph.D. advisor Prof. Tomonori Sato for his great support, guidance, motivation, and encouragement. I am indebted to Prof. Sato for being generous with his time at every stage of this research work, sharing his knowledge, and providing critical comments and suggestions. I am truly blessed to have him as my advisor. I would like to extend my sincere gratitude to Prof. Youichi Tanimoto, Prof. Masatomo Fujiwara, Prof. Fumio Hasebe, Prof. Shiro Tsuyuzaki, and Dr. Masamichi Ohba for their valuable time, comments and suggestions on my dissertation work.

I would also like to thank Mr. Shahbaz Mehmood, Head, Environment and Climatology Section, Global Change Impact Studies Centre (GCISC), Ministry of Climate Change, Islamabad, Pakistan for providing his valuable feedback on my research.

A special thanks go to King Abdullah University of Science and Technology (KAUST)'s high-performance computing (HPC) team who provided me computational resources for conducting the research and remained always quick to solve and respond to climate modeling related computational issues. I am also grateful to Dr. Fred Kucharski, Senior Research Scientist, International Center for Theoretical Physics (ICTP), Italy for helping and supporting me in understanding the theory and usage of global climate models and for his insightful and extensive discussions, suggestions, and thoughtful questions during my research work. I am also thankful to Dr. Udaya Bhasker and Dr. Basit Ali Khan for their enlightening discussions, time and support during my Ph.D. research. I would also like to thank my friends and colleagues, Vu, Hamza Bangalath, Andrew, Jish, Shahid Saghir, Rana Muhammad Bilal, and all others I cannot list one by one, for their support and help.

My extended thanks go to my beloved wife Ms. Amina Shahid and the rest of my family members for their love, and unwavering confidence in me. Finally, my deepest heartfelt gratitude goes to my parents: Mr. Muhammad Shafi Dogar and Mrs. Saeeda Begum, without their prayers, love, and appreciations, none of these accomplishments would have been possible.

## Table of Contents

<b>ABSTRACT .....</b>	<b>1</b>
<b>DEDICATION.....</b>	<b>5</b>
<b>ACKNOWLEDGEMENTS .....</b>	<b>6</b>
<b>LIST OF ABBREVIATIONS .....</b>	<b>9</b>
<b>Chapter 1. Background and Literature Review.....</b>	<b>14</b>
<b>1.1. Explosive Eruptions and Radiative Forcing.....</b>	<b>14</b>
1.1.1. MENA Sensitivity to Explosive Eruptions.....	17
<b>1.2. OBJECTIVES .....</b>	<b>23</b>
<b>Chapter 2. Model and Data.....</b>	<b>26</b>
<b>2.1. GFDL-HiRAM Model .....</b>	<b>26</b>
<b>2.2. Volcanic Radiative Forcing Data.....</b>	<b>27</b>
<b>2.3. Observations and Reanalysis Data.....</b>	<b>29</b>
<b>Chapter 3. Study of Climate Trends and Leading Modes of Climate Variability for the MENA Region.....</b>	<b>31</b>
<b>3.1. Introduction and Motivation .....</b>	<b>31</b>
<b>3.2. Model Climatology.....</b>	<b>32</b>
<b>3.3. Multiple Regression Analysis.....</b>	<b>33</b>
<b>3.4. Temperature and Precipitation Linear Trends .....</b>	<b>37</b>
<b>3.5. Temperature and Precipitation Polynomial Trends.....</b>	<b>40</b>
<b>3.6. Selection of Leading Predictors for MENA Region.....</b>	<b>41</b>
<b>3.7. NAO, ENSO and ISM Impacts.....</b>	<b>42</b>
3.7.1. NAO .....	43
3.7.2. ENSO .....	44
3.7.3. Indian summer monsoon .....	45
<b>3.8. Summary and Conclusions .....</b>	<b>52</b>
<b>Chapter 4. Sensitivity of the Regional Climate in the Middle East and North Africa to Volcanic Perturbations.....</b>	<b>54</b>
<b>4.1. Problem Formulation and Motivations .....</b>	<b>54</b>
<b>4.2. HiRAM Experimental Setup for Volcanic Impact Study .....</b>	<b>58</b>
<b>4.3. Methods .....</b>	<b>59</b>
<b>4.4. Results and Discussion .....</b>	<b>60</b>

4.4.1.	Radiative Impact.....	60
4.4.2.	Total Temperature and Precipitation Response.....	63
4.4.3.	Post-eruption Circulation Impacts.....	69
4.4.4.	Delineating the Effects of NAO, ENSO, ISM and Volcanic Aerosols .....	69
4.4.5.	Winter Climate Response .....	70
4.4.5.1.	ENSO .....	70
4.4.5.2.	NAO .....	72
4.4.5.3.	Volcanic direct impacts .....	74
4.4.6.	Summer Climate Response.....	75
4.4.6.1.	ENSO .....	75
4.4.6.2.	Indian Summer Monsoon .....	77
4.4.6.3.	Volcanic direct impacts .....	78
4.4.7.	Multiple Regression on the 30-Year and 109-Year Datasets .....	81
<b>4.4.8.</b>	<b>Robustness of Climate Responses using Multiple Regression Analysis .....</b>	<b>88</b>
<b>4.5.</b>	<b>Summary and Conclusions .....</b>	<b>91</b>
<b>Chapter 5.</b>	<b>Regional Sensitivity of Hadley Circulation to Post-eruption Anomalies</b>	<b>95</b>
<b>5.1.</b>	<b>Problem Formulation and Motivation.....</b>	<b>95</b>
<b>5.2.</b>	<b>Model, Data and Methodology .....</b>	<b>97</b>
<b>5.3.</b>	<b>Results and Discussion .....</b>	<b>99</b>
5.3.1.	Vertical Wind and Meridional Mass Stream Function Changes .....	99
5.3.2.	Midlatitude Jet Streams Response.....	102
5.3.3.	Wind, Precipitation and Cloud Response.....	104
<b>5.4.</b>	<b>Summary and Conclusions.....</b>	<b>109</b>
<b>Chapter 6.</b>	<b>Summary and Conclusions.....</b>	<b>111</b>
<b>6.1.</b>	<b>Regional Climatic Impact of Volcanism over MENA .....</b>	<b>111</b>
<b>6.2.</b>	<b>Future Research Work.....</b>	<b>113</b>
<b>References.....</b>		<b>115</b>
<b>Appendices.....</b>		<b>136</b>
<b>A.</b>	<b>Post-eruption QBO Impact and Limitation of This Study.....</b>	<b>136</b>
<b>B.</b>	<b>Robustness of Climate Responses using Multiple Regression Analysis .....</b>	<b>136</b>

## LIST OF ABBREVIATIONS

AGCM	Atmospheric General Circulation Model
AOD	Aerosol Optical Depth
AMO	Atlantic Multi-Decadal Oscillation
CFSR	Climate Forecast System Reanalysis
EA	East Atlantic
EA/WR	East Atlantic West Russia
ENSO	El Niño Southern Oscillation
GCM	General Circulation Model
GH	Geopotential Height
GFDL	Geophysical Fluid Dynamics Laboratory
HC	Hadley Cell
HiRAM	High Resolution Atmospheric Model
ICTP	International Center for Theoretical Physics
IMI	Indian summer Monsoon rainfall Index
IOD	Indian Ocean Dipole
IPCC	Intergovernmental Panel on Climate Change
ISM	Indian Summer Monsoon
ITCZ	Inter Tropical Convergence Zone
MENA	Middle East and North Africa
MOM4	Modular Ocean Model version 4
MOZART	Model for OZone and Related chemical Tracers
NAO	North Atlantic Oscillation
NCEP	National Center for Environmental Prediction
PNA	Pacific-North American
SPEEDY	Simplified Parametrizations, primitivE-Equation DYnamics
SST	Sea Surface Temperature
SWNET	shortwave net
UDEL	University of Delaware
WAM	West African Monsoon

## LIST OF FIGURES

- Figure 1.1:** Global mean surface temperature anomalies relative to the period 1901-1950, as observed (black line) and as obtained from climate model simulations with (a) both human-induced and natural factors (red lines) and (b) natural factors only (blue lines) are considered. Vertical gray lines indicate the timings of major volcanic eruptions. The thick red and blue curves show the multi-ensemble means and the thin lighter curves show individual simulations. (Source: IPCC Fourth Assessment Report, WG I; Figure 9.5). **15**
- Figure 1.2:** Nile and Niger River basins with the location of the Aswan (red circle) and Koulikoro (green circle) stations. July-August-September (JAS) averaged discharge on the Nile River at Aswan (red line) between 1870 and 1966 and on the Niger River at Koulikoro (green line) between 1907 and 1981. Also marked is the date of the Katmai eruption. (Source: Oman et al., 2006). **19**
- Figure 1.3:** Selected 50-year intervals of annual Nile River level surrounding the three largest high-latitude volcanic eruptions of the past 2000 yr. All plots show the high river level for each year, and the bottom plot also shows the low river level. Low river level data are missing for Laki and exhibit a large anthropogenic trend before Katmai. (Source: Oman et al., 2006). **20**
- Figure 2.1:** Vertically summed zonal mean Aerosol Optical Depth (AOD) at 550 nm. **28**
- Figure 2.2:** Vertically summed zonal mean extinction coefficient ( $10^{-5} \text{ m}^{-1}$ ) at 550 nm. **29**
- Figure 3.1:** Mean pattern of 2m surface air temperature ( $^{\circ}\text{C}$  in top) and precipitation (mm/day in bottom) in winter (DJF) season produced using CFSR (left panel) and HIRAM simulation (right panel) overlaid with mean wind vectors at 925 hPa. **33**
- Figure 3.2:** Time series of predictors (not standardized) from the observations and HiRAM used in the regression analysis in both seasons a) Indian Monsoon Rainfall Index, b) NINO3.4/DJF, c) NAO Index of Hurrell (1995). **36**
- Figure 3.3:** The spatial distributions of the trends (per decade) of winter (DJF) temperature over the period of 1979-2008 using (a) UDEL, (b) HiRAM output and trend in Precipitation using (c) UDEL and (d) HiRAM output. Hatching indicates statistically significant decadal trends at 95% confidence level. **39**
- Figure 3.4:** The spatial distributions of the trends (per decade) of summer (JJA) temperature over the period of 1979-2008 using (a) UDEL, (b) HIRAM output and trend in Precipitation using (c) UDEL and (d) HIRAM output. Hatching indicates statistically significant decadal trends at 95% confidence level. **40**
- Figure 3.5:** The polynomial trend curve for temperature/precipitation (top/bottom) fields in winter/summer (left/right) computed over MENA region over a longer period of 1900-2008. The anomalies of temperature and precipitation before (red curve) and after removing polynomial trend (green curve) are also shown. **41**
- Figure 3.6:** Winter (DJF) NAO correlation coefficient with surface air-temperature calculated using a) UDEL 30-year winter period, b) Model 30-year winter period, c) UDEL 30-year summer period, d) model 30-year summer period. Hatching shows the statistically significant areas with at least 95% confidence level. **48**
- Figure 3.7:** Winter (DJF) NAO regression coefficient with surface air-temperature (K) calculated using a) UDEL 30-year period, b) Model 30-year period, and with precipitation (mm/day) calculated using c) UDEL 30-year period, d) model 30-year period. Hatching shows the statistically significant areas with at least 95% confidence level. **49**
- Figure 3.8:** Winter (DJF) ENSO regression coefficient with surface air-temperature (K) calculated using a) UDEL 30-year period, b) Model 30-year period, and with precipitation (mm/day) calculated using c) UDEL 30-year period, d) model 30-year period. Hatching shows the statistically significant areas with at least 95% confidence level. **50**
- Figure 3.9:** Summer (JJA) ENSO regression coefficient with surface air-temperature (K) calculated using a) UDEL 30-year period, b) Model 30-year period, and with precipitation (mm/day) calculated using c) UDEL 30-year period, d) model 30-year period. Hatching shows the statistically significant areas with at least 95% confidence level. **51**
- Figure 3.10:** Summer (JJA) ISM regression coefficient of surface air-temperature (K) calculated using a) UDEL 30-year period, b) Model 30-year period, and with precipitation (mm/day) calculated using c) UDEL 30-year period, d) model 30-year period. Hatching shows the statistically significant areas with at least 95% confidence level. **52**

- Figure 4.1:** Total stratospheric aerosol optical depth at 550 nm as a function of time, zonally averaged over the MENA latitudes (data source: Sato et al., 1993). **62**
- Figure 4.2:** Seasonal (DJF and JJA) two-year anomalies of solar net flux ( $W/m^2$ ) composites following the El Chichón and Pinatubo explosive eruptions, calculated for winter using a) CFSR and b) HiRAM outputs, and for summer using c) CFSR and d) HiRAM outputs. Hatching shows the statistically significant areas with at least 95% confidence level. **63**
- Figure 4.3:** Seasonal (DJF and JJA) two-year anomalies of surface air temperature (K) composites following the El Chichón and Pinatubo explosive eruptions, calculated for winter using a) UDEL observations, b) HiRAM output, and for summer using c) UDEL observations, d) HiRAM output. Hatching shows the statistically significant areas with at least 95% confidence level. **64**
- Figure 4.4:** Same as Figure 4.3, but for precipitation anomaly (mm/day). **66**
- Figure 4.5:** Summer (JJA) total vertical regional Hadley Cell mass flux  $M_\phi$  (positive upward,  $10^{-3} \text{ kg m}^{-2}\text{s}^{-1}$ ) averaged over the period 1979-2008 (excluding post-eruption years) using a) CFSR, b) HiRAM outputs, and two-year composited anomalies of  $M_\phi$  ( $10^{-3} \text{ kg m}^{-2}\text{s}^{-1}$ ) following the El Chichón and Pinatubo eruptions calculated using c) CFSR, d) HiRAM outputs. **67**
- Figure 4.6:** ENSO-regressed anomalies of surface air temperature (K) and precipitation (mm/day) composited over two winter (DJF) seasons after both the El Chichón and Pinatubo eruptions. The temperature composites are calculated using a) UDEL observations, b) HiRAM output, and precipitation composites using c) UDEL observations, d) HiRAM output. Hatching shows the statistically significant areas with at least 95% confidence level. **72**
- Figure 4.7:** NAO-regressed anomalies of surface air temperature (K) and precipitation (mm/day) composited over two winter (DJF) seasons after both the El Chichón and Pinatubo eruptions. The temperature composites are calculated using a) UDEL observations, b) HiRAM output, and precipitation composites using c) UDEL observations, d) HiRAM output. Hatching shows the statistically significant areas with at least 95% confidence level. **73**
- Figure 4.8:** Winter (DJF) volcanic residual anomalies (direct volcanic cooling) of surface air temperature (K) and precipitation (mm/day) composited for two winter seasons following both the El Chichón and Pinatubo eruptions. The temperature composites are calculated using a) UDEL observations, b) HiRAM output, and precipitation composites using c) UDEL observations, d) HiRAM output. Hatching shows the statistically significant areas with at least 95% confidence level. **75**
- Figure 4.9:** ENSO-regressed anomalies of surface air temperature (K) and precipitation (mm/day) composited over two summer (JJA) seasons after both the El Chichón and Pinatubo eruptions. The temperature composites are calculated using a) UDEL observations, b) HiRAM output, and precipitation composites using c) UDEL observations, d) HiRAM output. Hatching shows the statistically significant areas with at least 95% confidence level. **76**
- Figure 4.10:** ISM-regressed anomalies of surface air temperature (K) and precipitation (mm/day) composited over two summer (JJA) seasons after both the El Chichón and Pinatubo eruptions. The temperature composites are calculated using a) UDEL observations, b) HiRAM output, and precipitation composites using c) UDEL observations, d) HiRAM output. Hatching shows the statistically significant areas with at least 95% confidence level. **78**
- Figure 4.11:** Volcanic residual anomalies (direct volcanic cooling) of surface air temperature (K) and precipitation (mm/day) composited over two summer (JJA) seasons after both the El Chichón and Pinatubo eruptions. The temperature composites are calculated using a) UDEL observations, b) HiRAM output, and precipitation composites - using c) UDEL observations, d) HiRAM output. Hatching shows the statistically significant areas with at least 95% confidence level. **80**
- Figure 4.12:** NAO regressed anomalies of surface air-temperature (K) and precipitation (mm/day) composited over two winter (DJF) seasons following both the El Chichón and Pinatubo eruptions. The temperature composites are calculated using a) UDEL 30-year period, b) UDEL 109-year period, and precipitation composites using c) UDEL 30-year period, d) UDEL 109-year period. Hatching shows the statistically significant areas with at least 95% confidence level. **82**
- Figure 4.13:** ENSO regressed anomalies of surface air-temperature (K) and precipitation (mm/day) composited for two winter (DJF) seasons following both the El Chichón and Pinatubo eruptions. The temperature composites are calculated using a) UDEL 30-year period, b) UDEL 109-year period, and precipitation composites using c) UDEL 30-year period, d) UDEL 109-year period. Hatching shows the statistically significant areas with at least 95% confidence level. **83**

- Figure 4.14:** ENSO regressed anomalies of surface air-temperature (K) and precipitation (mm/day) composited for two summer (JJA) seasons following both the El Chichón and Pinatubo eruptions. The temperature composites are calculated using a) UDEL 30-year period, b) UDEL 109-year period, and precipitation composites using c) UDEL 30-year period, d) UDEL 109-year period. Hatching shows the statistically significant areas with at least 95% confidence level. **84**
- Figure 4.15:** ISM regressed anomalies of surface air-temperature (K) and precipitation (mm/day) composited for two summer (JJA) seasons following both the El Chichón and Pinatubo eruptions. The temperature composites are calculated using a) UDEL 30-year period, b) UDEL 109-year period, and precipitation composites using c) UDEL 30-year period, d) UDEL 109-year period. Hatching shows the statistically significant areas with at least 95% confidence level. **85**
- Figure 4.16:** Trend regressed anomalies of surface air-temperature (K) and precipitation (mm/day) composited for two winter (DJF) seasons following both the El Chichón and Pinatubo eruptions. The temperature composites are calculated using a) UDEL 30-year period, b) UDEL 109-year period, and precipitation composites using c) UDEL 30-year period, d) UDEL 109-year period. Hatching shows the statistically significant areas with at least 95% confidence level. **86**
- Figure 4.17:** Trend regressed anomalies of surface air-temperature (K) and precipitation (mm/day) composited for two summer (JJA) seasons following both the El Chichón and Pinatubo eruptions. The temperature composites are calculated using a) UDEL 30-year period, b) UDEL 109-year period, and precipitation composites using c) UDEL 30-year period, d) UDEL 109-year period. Hatching shows the statistically significant areas with at least 95% confidence level. **87**
- Figure 5.1:** Zonal-mean omega (vertical velocity in shaded colors; Pa/s) and zonal-mean meridional mass stream function (in contours;  $10^8$  kg/s) mean pattern (a, b) calculated using 1979-2008 period and post-eruption two summer season averaged anomaly pattern following both the El Chichón and Pinatubo eruptions (c, d) from 20th century NOAA reanalysis (left) and HiRAM model at 25 km (right panel). The positive (negative) shaded values in color bar represent the sinking (rising) branch of HC. **101**
- Figure 5.2:** Mean (left panel) and anomaly (right panel) of zonal-mean Omega (vertical velocity in shaded colors; Pa/s) with overlaid zonal-mean wind vectors ( $v$ ;  $-100 \times \text{Omega}$ ) [m/s;  $100 \times \text{Pa/s}$ ] in the latitude-pressure plane. The mean pattern (calculated using the 1979-2008 period) is shown using a) 20CR, c) ERA-Interim, e) HiRAM at 50 km and g) HiRAM at 25 km and the post-eruption (following both the El Chichón and Pinatubo) two summer seasons averaged anomaly pattern is shown using b) 20CR, d) ERA-Interim, f) HiRAM at 50 km and h) HiRAM at 25 km. Positive shaded values in color bar represent sinking motion whereas negative values represent the rising branch of HC. Hatching shows the areas where the mean and anomaly pattern is significant at 95% confidence interval. **102**
- Figure 5.3:** Global zonally averaged zonal wind (m/s) mean pattern using a) 20CR, c) ERA-Interim, e) HiRAM at 50 km, and g) HiRAM at 25 km and anomaly response (averaged for two summer seasons following both the eruptions) using b) 20CR, d) ERA-Interim, f) HiRAM at 50 km, and h) HiRAM at 25 km. Mean response is calculated using 1979-2008 period after excluding two summer seasons following both the eruptions and anomaly for both the eruptions is calculated using this mean. Hatching shows the areas where the mean and anomaly pattern is significant at 95% confidence interval. **103**
- Figure 5.4:** Summer (JJA) mean and post-eruption two summer seasons averaged wind vector (m/s) anomaly (composited for El Chichón and Pinatubo eruptions) from 20 CR (a, b), ERA-Interim (c, d) and HiRAM at 50 km (e, f) and 25 km (g, h) horizontal resolutions. The mean wind vector plots are computed over the 1979-2008 period after excluding two post-eruption summer seasons and anomaly is shown as a composite response averaged over two summers following both the eruptions. **106**
- Figure 5.5:** Post-eruption two summer seasons averaged precipitation anomaly (mm/d) composites following El Chichón and Pinatubo using UDEL (top panel), HiRAM at 50 km (middle panel) and HiRAM at 25 km (bottom panel). Hatching shows the areas where the precipitation anomaly pattern is significant at 95% confidence level. **107**
- Figure 5.6:** Post-eruption two summer seasons averaged total cloud contents anomaly (%) composite following El Chichón and Pinatubo eruptions using HiRAM at 50 km (top panel), at 25 km (middle panel) and low cloud contents anomaly using HiRAM at 25 km (bottom panel). Hatching shows the areas where the cloud contents anomaly pattern is significant at 95% confidence level. **108**

**Figure 5.7:** Summer (JJA) precipitation anomaly (mm/d) averaged over (0-360° E, 3°S-35° N).

**109**

## **Chapter 1. Background and Literature Review**

### **1.1. Explosive Eruptions and Radiative Forcing**

Climatic changes happen as a result of internal variability within the climate system and external factors. The impact of external factors on the climate system can be roughly estimated using the concept of radiative forcing. Radiative forcing is an externally imposed perturbation in the radiative energy budget of the Earth's climate system (Hansen et al., 1997, 2005). One important component of radiative forcing is produced by volcanic eruptions.

Volcanism has long been implicated as a possible cause of weather and climate variations. Considerable discussion on the role of volcanic eruptions in modulating global and regional climate can be found in past reviews (Robock, 2000; Stenchikov et al., 2009; Timmreck, 2012). The impact of strong volcanic eruptions on atmospheric radiative and chemical properties can cause intensive nonlinear responses in the climate system. This places a great deal of importance on understanding the role of volcanic eruptions in causing the climate change and variability at the global and regional scale.

Explosive eruptions tend to inject large quantities of SO<sub>2</sub> and H<sub>2</sub>S into the lower stratosphere where these gases are oxidized to form sulfate aerosol plume. These sulfate aerosols eventually surround the entire globe by the atmospheric circulation, increase the planetary albedo and produce radiative cooling for subsequent one to two years by reflecting the incoming short wave radiation (Robock et al., 1995; 2000; 2002; Stenchikov et al., 1998; Timmreck, 2012).

A better understanding of volcanic eruption's impact on the global climate allows scientists to better understand the relative contributions of natural and human-induced factors on the global warming trend. Based on the observed data and global model simulations earlier studies have emphasized the role of volcanism in attenuating global warming. The climate model simulations conducted using natural forcing factors clearly show that the global temperature is significantly reduced following major explosive volcanic forcing (Figure 1.1). This suggests that for a better assessment of the climate variations, we need to consider the contribution caused by major explosive eruptions in our climate system.

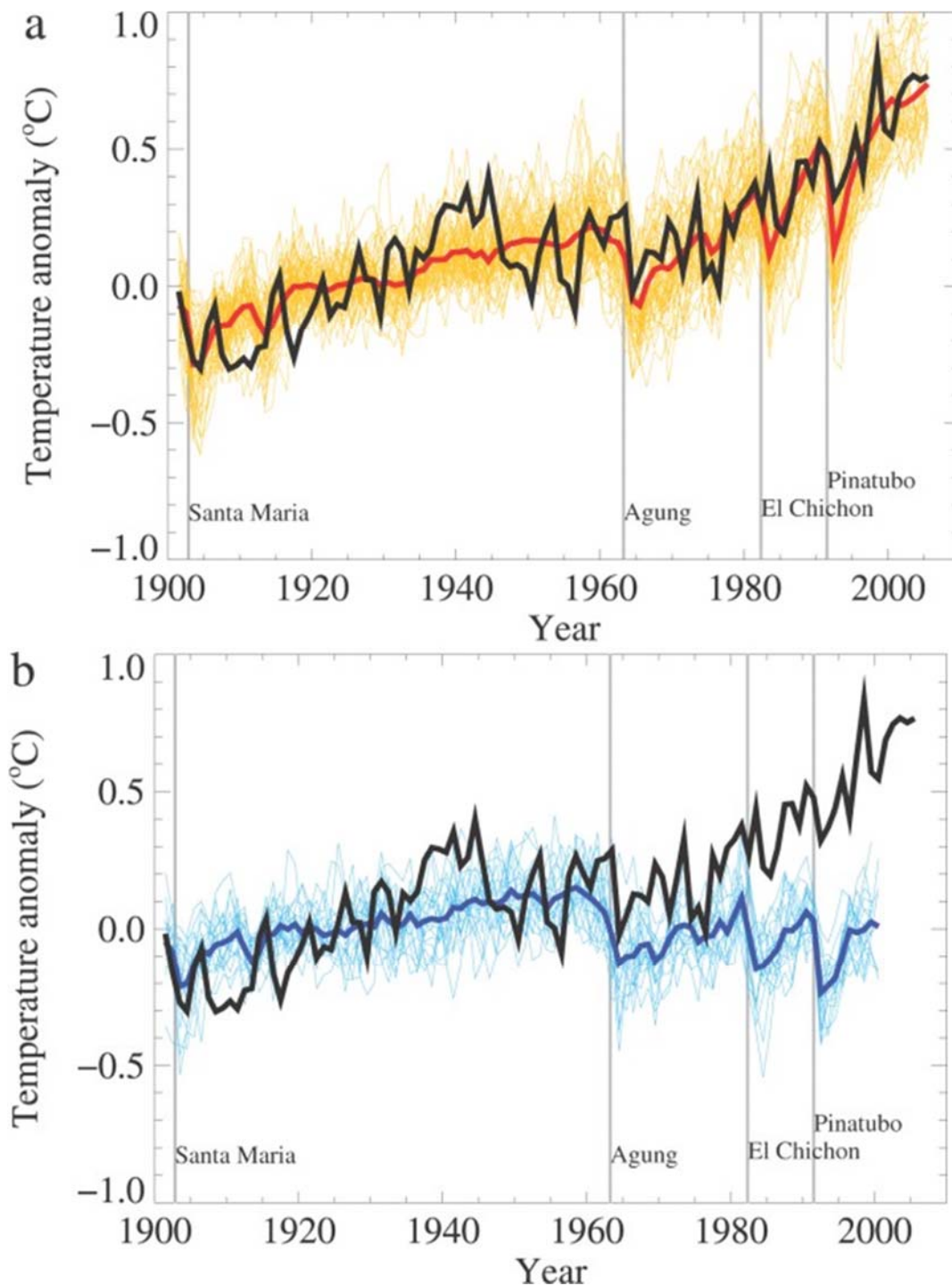


**Figure 1.1:** Global mean surface temperature anomalies relative to the period 1901-1950, as observed (black line) and as obtained from climate model simulations with (a) both human-induced and natural factors (red lines) and (b) natural factors only (blue lines) are considered. Vertical gray lines indicate the timings of major volcanic eruptions. The thick red and blue curves show the multi-ensemble means and the thin lighter curves show individual simulations. (Source: IPCC Fourth Assessment Report, WG I; Figure 9.5).

Volcanic eruptions have the capacity to alter drastically global climate both at shorter and longer timescales through their direct radiative and circulation effects on atmosphere and oceans. Large explosive eruptions are considered as an important driving factor of climate variability (Timmreck, 2012). The climate effects are more evident when the stratospheric aerosols are greatly enhanced after large volcanic eruptions. The two strongest eruptions of the late 20th century were El Chichón in April 1982 and Mount Pinatubo in June 1991. Pinatubo was the strongest and best documented event so far that produced the largest stratospheric volcanic aerosol cloud of the century by injecting about 20 megatons of sulphuric gases and more than hundred of megatons of ash particles into the lower stratosphere, affecting global climate for years (McCormick et al., 1995, Robock, 2002). After the Pinatubo eruption, a global maximum cooling of 0.4 K (Dutton and Christy, 1992; Thompson et al., 2009) and stratospheric warming of 2–3 K (Labitzke and McCormick, 1992) was observed which led to a decrease in tropopause height (Santer et al., 2003). Moreover, a decrease in stratospheric ozone (Eyring et al., 2006) and significant changes of the hydrological cycle were also observed, such as a reduction in tropical precipitation (Gu et al., 2007; Iles et al., 2013), river runoff (Trenberth and Dai, 2007), and sea level height (Church et al., 2005; Stenchikov et al., 2009) as well as a drying of the troposphere (Soden et al., 2002). A sound understanding of the role of volcanic eruptions in the climate system along with other natural and anthropogenic forcing factors is, therefore, a prerequisite for understanding future and past climate variability.

Although the net climatic effect of these eruptions at the global scale is cooling, their effect over regional scale could be cooling or warming depending upon the dynamic impact caused by these eruptions e.g., volcanically induced circulation changes over the Atlantic ocean cause warming over parts of Europe and Siberia and cooling over southern Europe and North Africa (Robock and Mao, 1992, 1995; Robock, 2002; Stenchikov et al., 1998, 2002, 2006). These changes result largely from an enhanced westerly airflow around the Northern Hemisphere, which brings warmer and wetter oceanic air over these European continents. This westerly flow, and therefore the surface temperature change, is associated with the leading variability pattern of Northern Hemisphere cold season sea level pressure (SLP), called the "Arctic Oscillation" (AO) that largely exhibits similar effects as NAO (Hurrell, 1995; Penner and Binyamin, 2013; Rind et al., 2005). Observations show an apparent upward trend in the amplitude of the positive phase of this pattern (Thompson and Wallace, 1998; Thompson et al., 2000). The variability associated with this pattern extends from the surface up into the stratosphere, and in fact the variability pattern can be equivalently defined as being composed of variability at all levels from the surface through the lower stratosphere (Baldwin and Dunkerton, 1999). Therefore, to better understand

the climate of any region, consideration of the effect of circulation changes along with direct radiative effect following volcanic eruption events is mandatory.

The Middle East and North Africa (MENA; 20° W to 70 °E and 5 °S to 45 °N) region is largely affected by the North Atlantic oscillation. As NAO is enhanced after these eruptions, the question arises how these changes in NAO oscillation will affect the MENA climate regime. Past studies have also emphasized that volcanic eruptions affect the seasonal movement of ITCZ both in winter and summer (Mass et al., 1989; Haywood et al., 2013). Recently it has been argued that the radiative perturbations caused by strong volcanism modulate the trade winds over the tropical Pacific such that they favor the positive phase of ENSO, which strongly affects the African and South Asian monsoonal rainfall. Hence studying the impact of post-eruption NAO, ENSO and monsoon dynamic circulation changes over MENA along with direct volcanic radiative effect including ITCZ shift could be of greater interest and need to be investigated in detail. Earlier studies have mainly discussed the direct radiative effect of volcanic eruptions over the Middle East and Africa; however, the sensitivity of MENA region to these eruptions through circulation changes has not been explored in detail.

I intend to focus on Middle East and African region because of its strong vulnerability and sensitivity but weak adaptive capacity to such climatic events (Robock, 2002; Genin et al., 1995; Haywood et al., 2013; Oman et al., 2006). Past studies show that volcanic eruptions may cause more droughts over this region because of post-eruption reduced precipitation amount as a result of diminishing of African monsoon (Trenberth and Dai, 2007; Oman et al., 2006), which will reduce agricultural resources because a sizeable portion of agriculture yields of this region is mainly fed by African summer monsoon.

#### **1.1.1. MENA Sensitivity to Explosive Eruptions**

Over the past few decades, there is a growing interest in the study of volcanic eruptions that resulted in a mature understanding of the climatic variability caused by these natural effects (Timmreck, 2012).

Similar to post-eruption winter warming over Eurasia, North America, and Siberia, it is well known that the Middle East winter weather is strongly affected by volcanic impacts. For example, after the 1991 Pinatubo eruption, there was an unusually cold winter and snowfall in Israel that led to a cold air temperature throughout the Middle East during the winter of 1992 (Genin et al., 1995; Robock, 2002).

Similarly, the eruption of Mount Etna in 44 B.C. diminished the solar radiation to such an extent that the resulting cooling caused crops to shrivel and produced famine in Rome and Egypt

(Forsyth, 1988). Yu and Zhou (2004) have shown that winter NAO has a strong negative correlation ( $\sim -0.4$ ) with surface air temperature over MENA particularly in February-March which clearly indicates the impact of positive NAO phase in winter season over entire MENA region. Several earlier studies have documented this cooling anomaly over Middle East after large eruptions (Robock and Mao, 1992, Shindel et al., 2004) with snowy conditions over Gulf of Aqaba (Genin et al., 1995; Robock, 2002) and pointed out that this cooling response could be due to volcanic direct radiative impact (Robock and Mao, 1992). However, there is rarely any study available that looked at the changes caused as a result of the dynamic response of post-eruption NAO circulation over MENA, and therefore in this dissertation, I will try to fill this gap.

Other than dynamic winter response over Europe from historical large tropical eruptions (Fischer et al., 2007), a large number of studies have also discussed radiative cooling response particularly in summer over the entire globe (Robock, 2003) focusing on Europe (Fischer et al., 2007) and Middle East after these tropical eruptions. In the last couple of years, some attention is also given to post-eruption drought-like conditions over Africa and Middle East region (Oman et al., 2006) and central India (Anchukaitis et al., 2010). It was also reported that volcanic eruption cast a shadow on African monsoon (Oman et al., 2005; Brönnimann et al., 2019) by affecting the position of ITCZ (Haywood et al., 2013). Additionally, large volcanic eruptions cause significant perturbations to the hydrological cycle (Trenberth and Dai, 2007), which is more pronounced under high latitude eruptions (Kravitz and Robock, 2011).

Earlier literature on explosive volcanism suggested that explosive eruptions affect MENA region strongly. For instance, after the Katmai eruption in 1912, both the Nile and Niger Rivers which are located in the MENA region had extremely low flow in the summer period of year 1913 (Figure 1.2) as measured at the Aswan (red) and Koulikoro (green) stations (Oman et al., 2006). The response of MENA region to the volcanic perturbations has also been discussed in Oman et al. (2006) using a very long climate record of the Nile River basin. Figure 1.3 shows 50-year intervals in the annual high Nile River level surrounding the three largest high-latitude Northern Hemisphere (NH) eruptions. In addition to the low flow following the Katmai eruption (Figure 1.3, top plot), very low flow was experienced in 1783 and 1784 following the Laki eruption (Figure 1.3, bottom plot). These two years had the lowest river levels of the surrounding 50 years. Similarly, a study conducted by Robock et al. (2002) on the impact of the Pinatubo eruption during post-eruption winter season highlighted that the cooling response over MENA region in the lower tropospheric temperature following 1991 Pinatubo eruption was much larger over the MENA region compared to other regions of the globe. This unusual cold winter in the Middle East region led to the death of coral reefs in the Red Sea region due to strong post-

eruption vertical mixing in the Red Sea. These studies suggest that the MENA region responds vigorously to volcanic perturbations, and therefore precise quantification of direct and indirect volcanic impacts over the MENA region is important.

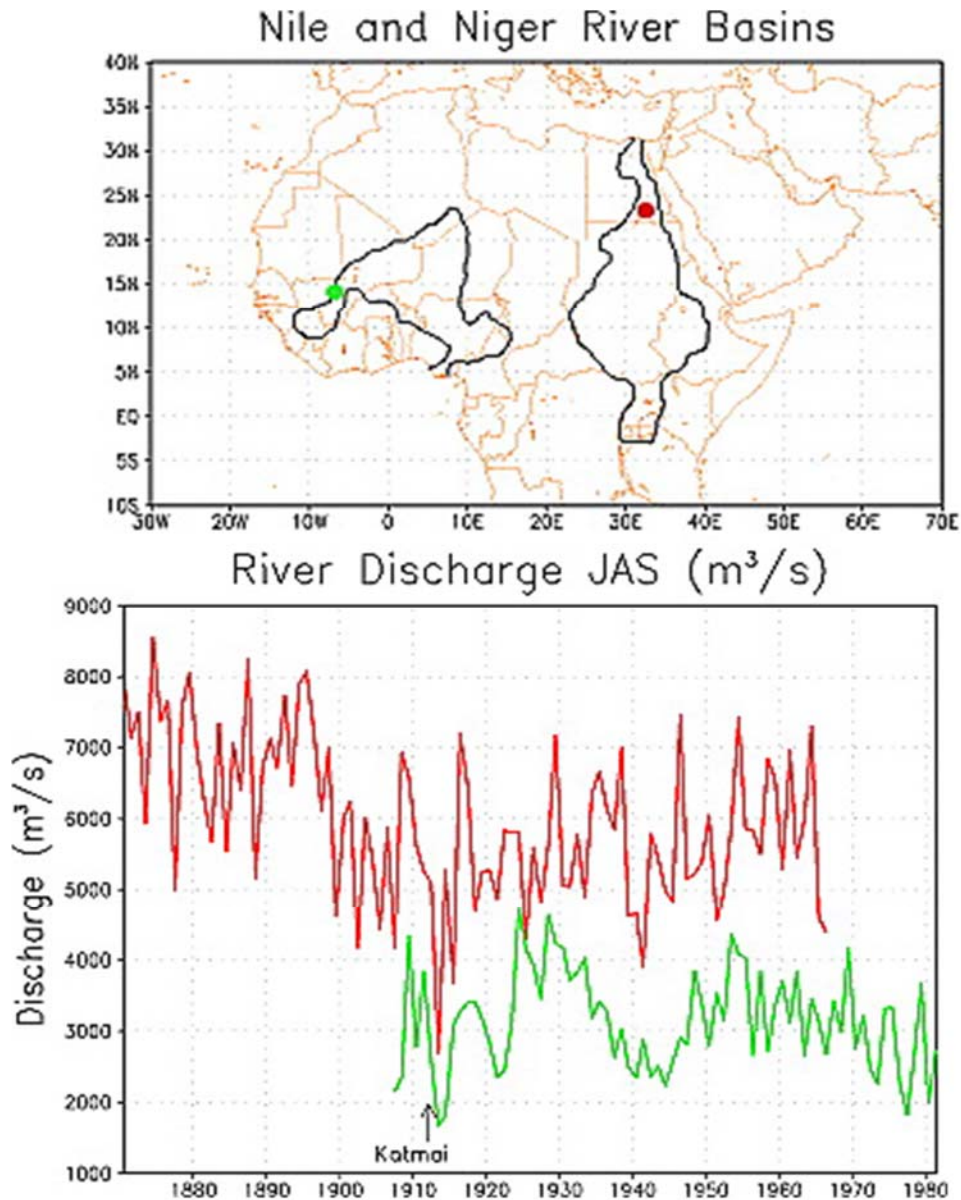


**Figure 1.2:** Nile and Niger River basins with the location of the Aswan (red circle) and Koulikoro (green circle) stations. July-August-September (JAS) averaged discharge on the Nile River at Aswan (red line) between 1870 and 1966 and on the Niger River at Koulikoro (green line) between 1907 and 1981. Also marked is the date of the Katmai eruption. (Source: Oman et al., 2006).

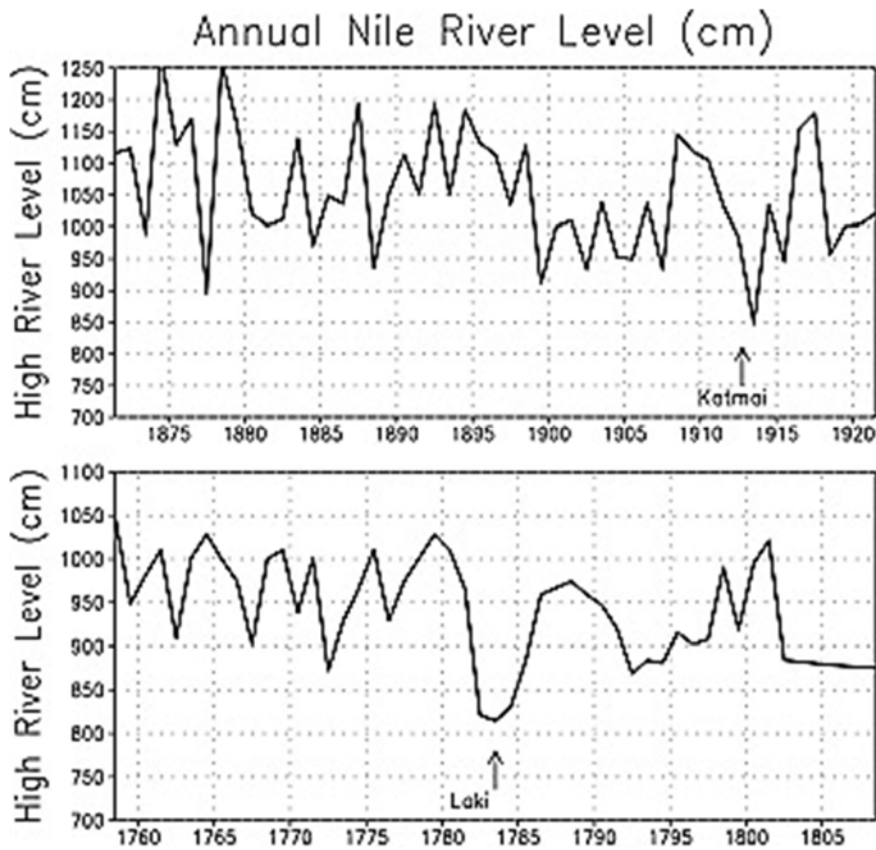


**Figure 1.3:** Selected 50-year intervals of annual Nile River level surrounding the three largest high-latitude volcanic eruptions of the past 2000 yr. All plots show the high river level for each year, and the bottom plot also shows the low river level. Low river level data are missing for Laki and exhibit a large anthropogenic trend before Katmai. (Source: Oman et al., 2006).

The climate in the Middle East region remains largely understudied. The Middle East is a climatic hot spot and is very sensitive to radiative forcings of different origins (e.g., anthropogenic forcing, dust and volcanic aerosol forcing), partly because surface energy balance in the arid regions is restored mostly by thermal radiation, i.e., by the surface temperature response (Papadopoulos et al., 2013; Serge et al., 2017). However, similar to the post-eruption high-latitude winter warming due to anomalously positive AO/NAO phase, post-eruption circulation changes play an important role for the MENA region (Serge et al., 2017).

Recent studies suggested that major volcanic eruptions significantly affect the climate in the Middle East and the Red Sea that should be carefully taken into account in assessments of long-term climate variability and warming trends in the Middle East and the Red Sea (Serge et al., 2017; Papadopoulos et al., 2013). It is observed that the Red Sea overturning circulation response to the strong volcanic eruptions was stronger and qualitatively different from that of the global ocean system (Osipov and Stenchikov, 2017).

Aerosol-induced cooling of the atmosphere rapidly modulates monsoon rainfall in this region (Oman et al., 2006; Haywood et al., 2013). Moreover, the global scale atmospheric circulations (e.g., ENSO and NAO) affect the MENA region strongly (Serge et al., 2017; Abualnaja et al., 2015). The atmospheric circulations such as NAO and ENSO are modulated by volcanism (Stenchikov et al., 2002; Stenchikov et al., 2009; Predybaylo et al., 2017). During the Pinatubo eruption, the observed SST in the Red Sea decreased more than 1 K, which was 3 times the globally averaged SST (Ding et al., 2014; Stenchikov et al., 2009) that caused increased overturning and vertical mixing, which severely affected the marine life (Genin et al., 1995). Therefore these climate drivers together with direct volcanic impacts produce strong impacts over the MENA region.

The upward branch of the Hadley Cell in the MENA region is strongly driven by the strength of its monsoon system. The rain-belt across MENA can largely be seen as the ascending branch of the local Hadley circulation. Moreover, there are many distinct regional circulation features embedded within this large-scale averaged circulation, such as the West African monsoon (WAM), African easterly jet (AEJ), tropical easterly jet (TEJ), and West African westerly jet (WAWJ), which drive the local Hadley circulation in the MENA region and affects its rising branch (e.g., Nicholson 2009; Cook 1999; Thorncroft and Blackburn 1999). Radiative forcing produced by the aerosols could strongly affect these large-scale global and regional circulations (Bangalath and Stenchikov, 2015; 2016) making this region sensitive to these climate forcings (i.e., ENSO, NAO, aerosol forcing). Therefore, a combination of both global and regional circulation changes and the complex multiscale interplay among these circulations play a crucial role in shaping the climate of the MENA region. The sensitivity of MENA tropical regions especially the tropical Sahel region to aerosol radiative forcing are explained in earlier studies (Vinoj et al., 2013; Yoshioka et al., 2007; Joseph and Zeng, 2011; Haywood et al., 2013). These studies shed light on the physical mechanisms such as aerosol-induced zonal and meridional thermal imbalance that weakens the cross equatorial Somali current and affects local monsoon-ITCZ coupled system. Moreover, aerosol-induced pressure and height gradients, wind changes, and local feedback mechanisms (e.g., planetary albedo, drought–vegetation, clouds, and orographic effect) amplify the climatic sensitivity of the MENA.

The monsoon-desert mechanism (Rodwell and Hoskins, 1996) suggests a remote dynamical link between Indian-monsoon forcing and African desertification. This mechanism shows that the remote diabatic heating in the Asian monsoon region can induce a westward propagating Rossby wave pattern that interacts with air on the southern flank of the mid-latitude westerlies causing it to descend. This adiabatic descent is localized over the eastern Sahara and

Mediterranean, and over the mountains of North Africa and southwest Asia. It is further noticed that the monsoon-desert mechanism does not represent a simple ‘Walker-type’ overturning cell. Instead, the descending air is seen to be mainly of mid-latitude origin. It is speculated that the monsoon-forced adiabatic descent may result in clear air and, therefore, a local diabatic enhancement, which effectively doubles the strength of descent. With this mechanism, desertification can be forced by remote changes in monsoon strength rather than by local effects.

Although there is not yet a complete understanding of the dynamical pathways by which tropical variability (produced by natural climate drivers e.g., volcanism, NAO and ENSO) can influence this region, there have been several studies of the influence of tropical convection occurring over a region extending from the eastern Indian Ocean to the western Pacific Ocean. Enhanced tropical Indo–west Pacific Ocean convection results in increased diabatic heating, which excites baroclinic (Barlow et al. 2002, 2005, 2007; Barlow 2011; Hoell et al. 2012, 2013) and barotropic (Hoell et al. 2013) stationary Rossby waves over central-southwest Asia and the Middle East. The mean wind appears to be important in increasing the northward extent of the classic Gill–Matsuno type response to tropical forcing, which assumes a resting basic state (Barlow 2011; Adames and Wallace 2014). The stationary Rossby waves thermodynamically interact with the mean climate, resulting in modifications to the mid- and upper-tropospheric temperature advection, which is balanced by precipitation-suppressing subsidence (Barlow et al. 2005; Hoell et al. 2012; Hoell et al. 2014b). Anticyclonic circulation associated with Rossby waves also reduces the flux of moisture into the region from tropical Africa and the Arabian Peninsula (Mariotti et al. 2002, 2005; Mariotti 2007; Barlow and Tippett 2008; Hoell et al. 2014b). The Indo–west Pacific convection also appears to excite eastward-traveling barotropic Rossby waves that can travel across the Northern Hemisphere and influence the Middle East, Africa and central southwest Asia from the west (Hoell et al. 2013). Additionally, a hemispherically symmetric influence from ENSO (produced independently or by volcanism) has been proposed in Seager et al. (2003, 2005), resulting from interaction between the tropically forced subtropical jet anomalies and transient activity. Thus, there are indications that tropical Indo-Pacific Ocean anomalies can influence the region with a modified Gill–Matsuno-like response to the west, a response to the east that propagates around the hemisphere, and a hemispherically symmetric response. Over the region, these wind circulations modify mid-level vertical velocity, moisture flux, and storm tracks (Barlow et al., 2016).

The Indian and African summer monsoon was diminished after the strong eruption events due to differentially reduced solar flux over the Indian Ocean and the large landmasses of Asia and Africa (Kravitz et al., 2010). This post-eruption African and Indian monsoon diminishing

seems strongly correlated (Joseph and Zeng, 2011) and therefore studying the impact of Indian summer monsoon over the MENA region is important to find the dynamic connection between post-eruptions MENA climatic response and Indian monsoon in summer (June-July-August, JJA). The above discussion indicates that MENA region is highly sensitive to volcanic eruptions and therefore the analysis of MENA region will give more insights for making reasonable findings that could help the people of this region in general and the climate community, in particular, to cope with the climatic changes caused by volcanism. Using model and observational analysis I will investigate post-eruption summer and winter thermal and dynamic responses over MENA in detail in the upcoming chapters, where I will first identify the main climate controls that affect this region (Chapter 3) and then in subsequent chapters I will quantify the regional climatic impact of those climate drivers.

## **1.2. OBJECTIVES**

Volcanism is considered as an important external radiative forcing that plays a significant role in our climate system through their direct radiative and indirect circulation impacts. An explosive volcanic eruption injects sulfate aerosols into the lower stratosphere, which scatter the incoming solar radiation, and plays an important role in reducing the amount of incoming solar radiation reaching the Earth surface (Robock, 2000). Subsequently, the reduction of the downward solar flux at surface caused by volcanic aerosols is able to change the mean state of the tropical Pacific toward the El Niño-like pattern evidenced from proxies (Handler, 1984; Adams et al., 2003; D'Arrigo et al., 2009; Wilson et al., 2010; Shaheen et al., 2013) and modeling studies (Mann et al., 2005; Emile-Geay et al., 2008; McGregor et al., 2010; Landrum et al., 2013; Ohba et al., 2013, Predybaylo et al., 2017). Moreover, it has been recognized that explosive volcanic eruptions could induce warm/cold sea surface temperature (SST) changes in the tropical Pacific through feedback processes (Meehl et al., 2003; van Loon et al., 2004, 2007; van Loon and Meehl, 2008; Meehl et al., 2008, 2009) that induce substantial global and regional climatic changes. Hence, studying the role of volcanism through their direct and indirect impacts in our climatic system is essential for a better understanding of the global and regional climatic variability.

In the previous literature, the direct radiative impacts of volcanism at the global scale are well documented, however, uncertainties exist in terms of volcanic-induced circulation changes and their regional impacts. A better understanding and quantification of the global and regional scale temperature and precipitation patterns induced by strong volcanism are therefore essential. In this dissertation work I will focus on strong volcanic forcing and will assess their regional scale climatic impacts in the Middle East and North Africa region, as this region appears to be

very sensitive to the impacts (direct radiative and post-volcanic circulation changes) caused by the volcanic forcing (Robock, 2002; Genin et al., 1995; Haywood et al., 2013; Oman et al., 2006). Hence, I intend to focus on the MENA region because of its strong vulnerability and sensitivity to such climatic events. Past studies show that volcanic eruptions may cause more droughts over this region because of post-eruption reduced precipitation amount as a result of diminishing of African monsoon (Trenberth and Dai, 2007; Brönnimann et al., 2019). This will reduce agricultural resources because a sizeable portion of agriculture yields of this region is mainly fed by African summer monsoon.

MENA region is also largely affected by the North Atlantic oscillation. As the positive phase of NAO is enhanced after these eruptions (Stenchikov et al. 2002; Rind et al., 2005; Kirchner et al., 1999; Zambri et al., 2017; Graf et al., 1994), the question arises how these changes in NAO will affect the MENA climate regime. Past studies have also emphasized that volcanic eruptions affect the seasonal movement of ITCZ both in winter and summer (Mass et al., 1989; Haywood et al., 2013). Hence studying the impact of post-eruption NAO and monsoon dynamic circulation changes over MENA including ITCZ shift could be of greater interest and need to be investigated in detail. However, there is barely any detailed study that has mainly focused on the climatic sensitivity of MENA to circulation changes following explosive volcanism (such as ENSO, NAO and Indian monsoon); hence this study is an antecedent to fill this research gap.

Global climate models have been successfully employed for simulating the major observed effects of large volcanic eruptions at global scale (Graf et al., 1993; Kirchner et al., 1999; Shindell et al., 2001; Stenchikov et al., 2002, 2004), nevertheless, they still lack in accurately reproducing the regional impacts. This study will provide us an opportunity to demonstrate the mechanistic strength of HiRAM atmospheric model in simulating regional climatic impacts of volcanism, respectively, over the MENA region. Hence, I will study in detail the direct radiative impact of volcanism and post-eruption circulation feedbacks, especially caused by the NAO, ENSO, and the Indian summer monsoon (ISM). I selected these variability modes as they are reported to have larger climatic impact over the MENA region compared to other existing modes of variabilities (Yu and Zhou, 2004; Papadopoulos et al., 2013; Abualnaja et al., 2015; Wanner et al., 2001; Krichak et al., 2002; Lim, 2015). I will focus on the following research questions:

1. What are the main climate drivers that affect MENA region in winter and summer season?
2. How sensitive is the MENA climate to volcano-induced radiative perturbations?

3. How are the MENA climate responses get modulated by the effects of ENSO, NAO, and ISM?
4. How well can HiRAM, a high-resolution atmospheric model, reproduce post-eruption direct radiative and circulation changes over the MENA region?

To answer above posed questions, regarding the study of volcanism and associated circulation changes in the MENA region, I make use of a high-resolution Atmospheric Global Climate Model typically at a resolution of a Regional Climate Model (RCM), to better investigate volcanic-induced regional climate responses. A global scale simulation at a typical RCM resolution, in the present case 25 km, incorporates multi-scale climate processes that are decisive in defining the regional climate. Such simulations are capable of resolving circulations ranging from planetary-scale to regional scale circulations and teleconnections. High-resolution global simulations are particularly relevant in the present case, where the volcanic-induced radiative effect perturbs circulations at various scales, which define the net climate response at regional-to-global scales. The global high-resolution simulations are conducted to elucidate the climate responses to volcanic direct radiative and indirect circulation effect. The current dissertation, therefore, analyses the responses and sensitivity of a range of multi-scale circulations by utilizing the high-resolution global simulations.

The dissertation is organized into six chapters. The introductory chapter provides an overview; background and literature review of volcanic forcing and associated climate responses, which contextualize the research questions addressed in the dissertation. It emphasizes on the background and importance of volcanic forcing and their global and regional climatic impacts, especially in the MENA and South Asian regions. Chapter 2 describes the climate model and data used along with the experimental setup employed for conducting dissertation research work. The importance of trend in data and leading climate modes affecting the MENA region are discussed in Chapter 3. Chapter 4, in general, portrays the climate response over MENA to volcanic effect. This chapter specifically investigates the response of the global and regional circulations that include ENSO, NAO and Indian monsoon circulations and their consequent impact across MENA region following El Chichón and Pinatubo tropical volcanism. To better understand the shift of ITCZ and associated cloud and precipitation changes in the MENA and South Asian regions, I looked at the response of Hadley circulation to volcanic forcing in Chapter 5. Finally, in Chapter 6, the main findings are summarized with conclusions. Possible suggestions on relevant future work are also described in this last chapter.

## **Chapter 2. Model and Data**

In this dissertation, I used a very high-resolution global climate model, HiRAM effectively at 25 km grid spacing, to study the volcanic direct and indirect impacts over the MENA region. High-resolution global simulations are particularly essential in the present case, as I am focusing on the regional climate impacts, which can only be better resolved by high resolution global climate model simulations. A regional model has limitations in simulating these large-scale volcanic impacts as they possibly trigger large-scale dynamic processes and associated two-way interactions that fall in the scope of global climate models. To compare model simulation results for both the eruptions, I used the University of Delaware (UDEL) and climate forecast system (CFS) reanalysis datasets. The details of HiRAM model, its experimental setup, observational and reanalysis datasets are given below.

### **2.1. GFDL-HiRAM Model**

For the study of volcanic impact over MENA, I employ the Geophysical Fluid Dynamics Laboratory (GFDL)'s global high-resolution atmospheric model, HiRAM. It is based on version 2 of the GFDL Atmospheric Model (AM2; Anderson et al., 2004), with modifications such as increased horizontal and vertical resolutions (with 32 vertical layers instead of 24, to better simulate the processes in the lower stratosphere and its coupling with the troposphere). The model top at 1 hPa (~50 km height) effectively incorporates post-eruption climatic processes happening in the lower stratosphere, which are especially important for volcanic-induced climatic interactions. It uses simplified parameterizations for moist convection and large-scale stratiform cloudiness. The relaxed Arakawa-Schubert convective closure scheme (Moorthi and Suarez, 1992) used in AM2 has been replaced by a shallow convective parameterization scheme (Bretherton et al., 2004). HiRAM uses a comparatively new cubed-sphere finite-volume dynamic core (Putman and Lin, 2007), a prognostic cloud scheme with a sub-grid scale distribution of total water and multi-species tropospheric aerosol climatology precalculated using the Model for OZone and Related chemical Tracers (MOZART) (Horowitz et al., 2003). HiRAM retains the surface flux, land surface, boundary layer, gravity wave drag, radiative transfer modules and large-scale cloud microphysics of AM2 (Anderson et al., 2004; Zhao et al., 2009). The land model used by HiRAM, known as LM3, includes soil sensible and latent heat storage, groundwater storage, and stomata resistance (Malyshev et al., 2015).

The shortwave (SW) radiation algorithm used in HiRAM follows Freidenreich and Ramaswamy (1999). The SW spectrum ranges from 0.17 to 4.00  $\mu\text{m}$  and is divided into 25 bands: 10 bands in the near IR region, 4 bands in the visible region and 11 bands in the UV region, and includes absorption by  $\text{H}_2\text{O}$ ,  $\text{CO}_2$ ,  $\text{O}_3$ ,  $\text{O}_2$ , and Rayleigh scattering. The longwave radiation code follows a modified form of the simplified exchange approximation (Schwarzkopf and Ramaswamy, 1999). It accounts for the absorption and emission by the principal gases present in the atmosphere, including  $\text{H}_2\text{O}$ ,  $\text{CO}_2$ ,  $\text{O}_3$ ,  $\text{N}_2\text{O}$  and  $\text{CH}_4$ , and the halocarbons, CFC-11, CFC-12, CFC-113, and HCFC-22. Aerosols and clouds are treated as absorbers in the longwave radiation code, with non-grey absorption coefficients specified in the eight spectral bands of the transfer scheme, following the methodology adopted in Ramachandran et al. (2000). A detailed description of the model and a list of recent publications can be found at GFDL’s website. Table 1 highlights the basics of the HiRAM model and experimental details used for this study.

**Table 1:** Summary of GFDL-HiRAM, and input forcing data used for volcanic simulations.

<b>Resolution</b>	<b>Model Top</b>	<b>Convective Scheme</b>	<b>Vertical layers</b>	<b>Dynamic core</b>
25 km	1 hPa (~50 km)	Shallow convective parameterization scheme	32 vertical layers	Cubed-sphere finite-volume dynamic core.
<b>Simulation Period</b>		<b>Volcanic Forcing Data</b>	<b>Other Forcing</b>	<b>SST Data</b>
1979-2008. First 3 years are not used in the analysis to avoid spin-up effects.		Single Scattering Albedo, Extinction Coefficient & Asymmetry Parameter for El Chichón and Pinatubo eruptions are prescribed (Stenchikov et al., 1998).	All other forcing follows AMIP simulation setup.	Prescribed HadISST1 data set (Rayner et al., 2003).

## 2.2. Volcanic Radiative Forcing Data

In order to simulate the volcanic impacts caused by the El Chichón and Pinatubo eruptions, aerosols’ optical properties are prescribed in the model according to Stenchikov et al. (1998) using aerosol effective radius and aerosol optical depth retrieved by Sato et al. (1993). This volcanic data set provides zonally averaged monthly mean spectral dependent aerosol extinction, single scattering albedo, and an asymmetry parameter which are required to conduct radiative transfer simulations within HIRAM. These parameters are used as input volcanic radiative

forcing for El Chichón and Pinatubo eruptions. They are provided to model's radiative transfer module both for its shortwave (SW) and longwave (LW) spectral bands in the stratosphere. Mie solution on the aerosol optical depth from Sato et al. (1993) is used to compute these aerosol optical properties. The observed aerosol cloud took on a zonal structure within a few weeks after these eruptions and changed smoothly in time (McCormick et al., 1995). The detailed description of aerosol optical characteristics and computation steps used for the preparation of this zonally averaged monthly mean spectral dependent volcanic data is available in Stenchikov et al. (1998). The direct LW radiative effect of volcanic aerosols on the troposphere and surface energy balance is negligibly small (Stenchikov et al., 1998) and is therefore not considered. Figure 2.1 shows the vertically summed zonally averaged aerosol optical thickness at 550 nm that is used to compute above stated aerosol optical properties (i.e., aerosol extinction, single scattering albedo, and an asymmetry parameter). This plot highlights the spatial and temporal distribution of AOD at 550 nm for the major volcanic eruptions happened during the period 1900-2000. Figure 2.2 shows the vertically summed zonal mean extinction coefficient (per meter) at 550 nm (i.e., at model spectral band 07). These optical volcanic aerosol characteristics are taken as input volcanic forcing data in the HiRAM model for the period of 1976-2008 (volcanic data up to period 2000 is shown) that covers El Chichón (April 1982) and Pinatubo (June 1991) eruptions.

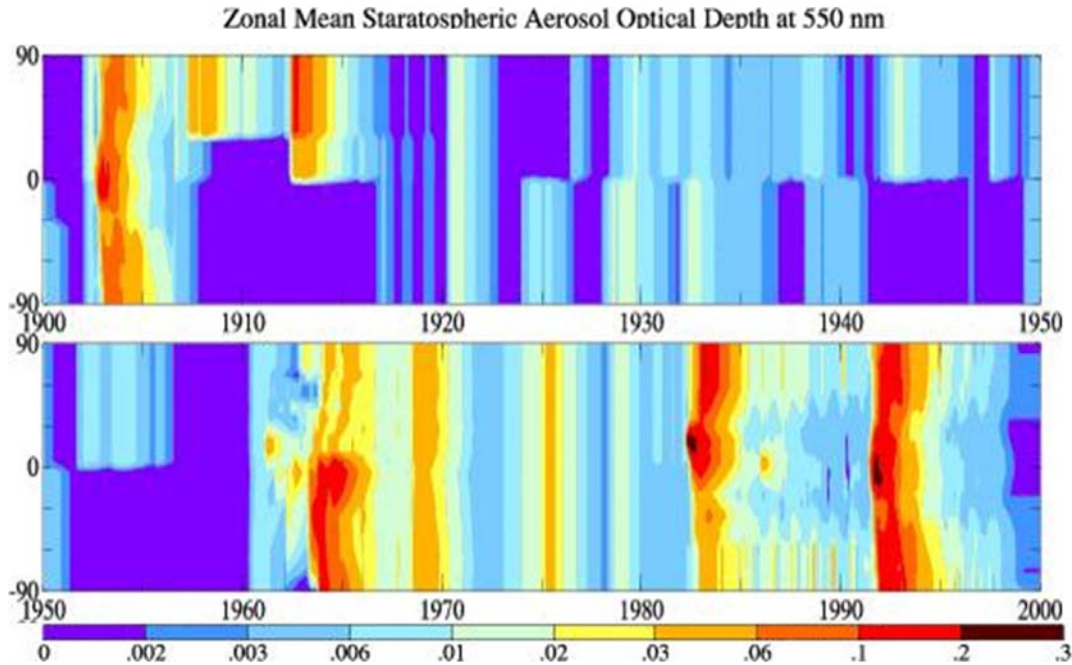


**Figure 2.1:** Vertically summed zonal mean Aerosol Optical Depth (AOD) at 550 nm.

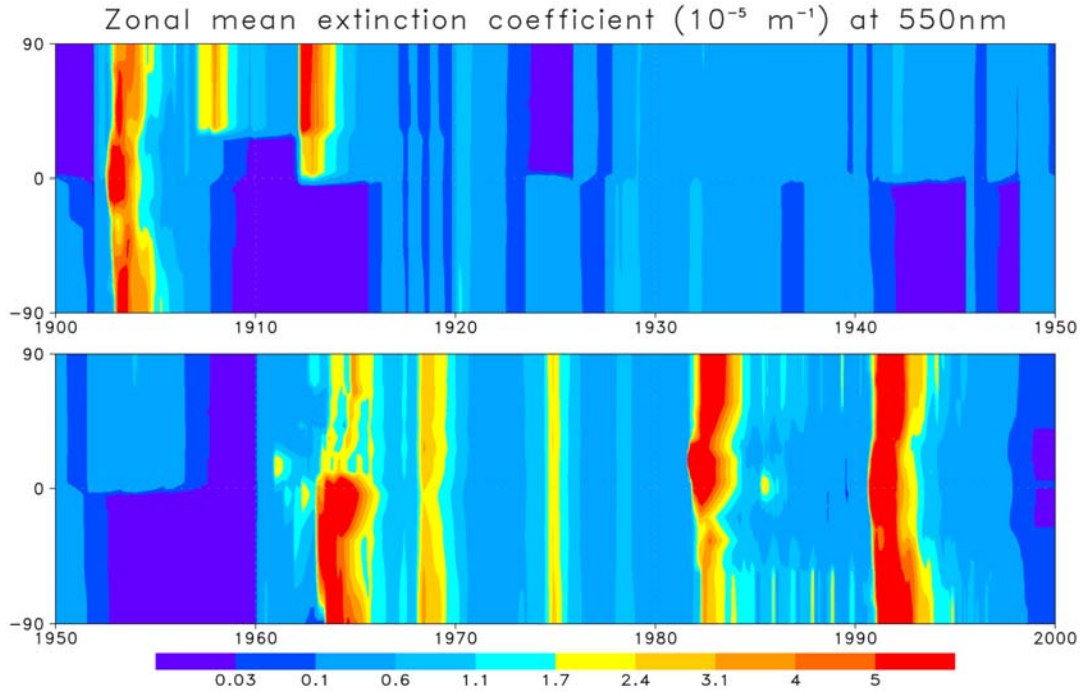


**Figure 2.2:** Vertically summed zonal mean extinction coefficient ( $10^{-5} \text{ m}^{-1}$ ) at 550 nm.

### 2.3. Observations and Reanalysis Data

For comparison and validation of the HiRAM response over MENA, I used University of Delaware (UDEL, V2.01) monthly and global gridded ( $0.5^\circ$  latitude x  $0.5^\circ$  longitude) data of surface air temperature and precipitation fields. The UDEL dataset is preferred here due to its high resolution, rigorous quality assurance, and dense observational network coverage (Peterson et al., 1998). These data sets are built from a large number of station observations, both from the GHCN2 (Global Historical Climate Network version 2) and, more extensively, from the archive of Legates & Willmott (1990). They are available from 1900 to 2010. The UDEL dataset covers land only. A complete description of UDEL temperature and precipitation data sets and corresponding references can be found at the University of Delaware website (<http://climate.geog.udel.edu/~climate/>).

For the validation of the atmospheric overturning circulation and radiation fluxes, the National Center for Environmental Prediction (NCEP) Climate Forecast System (CFS) Reanalysis (CFSR) product is used (Saha et al., 2010). CFSR is a high-resolution coupled ocean-atmosphere reanalysis, produced using an NCEP T382L64 ( $\sim 38\text{km}$  spatial resolution) atmospheric model, coupled with the GFDL MOM4 ocean model at  $0.25^\circ$  horizontal resolution in the tropics with 40 vertical levels. CFSR assimilates satellite observations in the form of radiance

rather than retrieved values, with bias correction and spin-up runs at full resolution. CFSR also assimilates surface observations, accounts for time-varying CO<sub>2</sub> and other radiatively absorbing gases, volcanic aerosols and solar flux variations (Saha et al., 2010). Explicit accounting for volcanic aerosols and a high spatial resolution make CFSR especially suitable for my purposes.

For the analysis of Hadley Cell response to explosive volcanism, discussed in Chapter 5, I used 20th Century Reanalysis (20CR) of National Oceanic and Atmospheric Administration (NOAA) as well as ERA-Interim reanalysis data. 20CR is a comprehensive global atmospheric dataset spanning the twentieth century at 6-hourly temporal and 2° spatial resolutions. It is produced using observed interpolated monthly sea-surface temperature and sea-ice distributions from the Hadley Centre SST and Sea Ice dataset (Rayner et al., 2003) as prescribed boundary conditions. It uses an Ensemble Kalman Filtering data assimilation method and a new version of the National Centers for Environmental Prediction (NCEP) Global Forecast System atmosphere-land global numerical weather prediction model to generate background ‘first guess’ fields (Compo et al., 2011). The annual averages of the time-varying CO<sub>2</sub> concentration, volcanic aerosols, and downward solar radiation flux used in 20CR are specified as described in (Saha et al., 2010). The ERA-Interim dataset used in this study is a reanalysis that is based on an assimilation system that includes a 4-dimensional variational analysis (4D-Var) with a 12-hour analysis window. The spatial resolution of the ERA-Interim dataset is approximately 80km on 60 vertical levels from the surface up to 0.1 hPa (Dee et al., 2011).

### **Chapter 3. Study of Climate Trends and Leading Modes of Climate Variability for the MENA Region**

Before looking at the climate responses of the MENA region to volcanic forcing (chapter 4), it will be useful to examine the long-term climate variability of the MENA region to get an idea of the key climate controls that affect this region. For this purpose, I used regression analysis and investigated the role of trends, and other leading circulation modes such as NAO, ENSO and Indian summer monsoon in inducing temperature and precipitation variability in the MENA region over the period 1979-2008.

#### **3.1. Introduction and Motivation**

Climate change is a contentious subject and one of the primary methods to prove or disprove its existence is the trend analysis of climate variables. The analysis of climate trends is important to understand whether the climate is changing or not, and to determine the causes of such change. The Middle East and North Africa, primarily the Arabian Peninsula is a region where the rate of mean surface temperature rise per decade is among the highest globally known during the recent past (Hansen et al., 2010; Almazroui et al., 2012; Croitoru and Piticar, 2013; del Río et al., 2013). Therefore, it is of significant practical importance to analyze the trends in the temperature and precipitation fields; to have a better understanding of climatic changes caused by internal and external climate forcings (such as volcanism, ENSO, NAO and Indian monsoon), keeping in mind the uncertainty introduced as a result of the scarcity of the observational measurements in this region (Morak et al., 2013). The trend in climate data is a long-term change that could be caused as a result of non-climatic factors. Moreover, the trend in data may add significant bias and uncertainty in climatic responses (as it could mask or enhance the climatic signal) and therefore its detection and removal both from observational and model data is indispensable. Trend free data could help in the accurate quantification of the radiative effect of volcanic forcing, both direct volcanic radiative impact and post-volcanic circulation effects. For this purpose, I included the climate trend index as an input predictor along with other leading explanatory predictor variables (i.e., NAO, ENSO and Indian summer monsoon) in the multiple regression analysis and filtered out the trend contribution from volcanic and circulation based climate responses (see chapter 4 for details). The trends of temperature and precipitation fields are computed using multiple regression analysis and their statistical significance is tested at a 95% confidence level. A two-tailed student t-test is applied to find the statistical significance of the trends and the regression coefficients of NAO, ENSO and the Indian summer monsoon, both in the model and the observations (see, e.g., Santer et al., 2000 for details). This chapter highlights

the importance of the trend in data. Moreover, I also assess the importance of different leading modes of variability in this chapter and compute their regression maps to better understand their mean seasonal association with MENA temperature and precipitation fields. Using multiple regression technique, I assess the importance of different teleconnections (e.g., NAO, ENSO and Indian summer monsoon) over the MENA region. This chapter sheds light on the internal mechanisms of MENA climate variability and its sensitivity to leading teleconnection modes. The main questions that are discussed in this chapter are as follows: (1) what is the role of temperature and precipitation trends over the MENA region? (2) How the leading modes of variabilities (ENSO, NAO, and ISM) affect the MENA climatic regime? Initially, in Section 3.2, I validated my high-resolution model simulation by comparing model climatology with the CFS reanalysis data following which I discussed the multiple linear regression analysis. In the subsequent sections, I analyzed the trend and regression coefficients for the MENA region.

### **3.2. Model Climatology**

Before proceeding into the detailed analysis of the MENA region, it is necessary to look at the performance of HIRAM AGCM in reproducing global climatological features of temperature and precipitation patterns. Figure 3.1 shows simulated global mean pattern of 2m surface air temperature and precipitation overlaid with mean pattern of zonal and meridional wind vector distribution at 925 hPa in winter (DJF) season produced using CFS Reanalysis and HiRAM model. These winter climatology patterns for CFSR and HiRAM simulation are computed using the period 1979–2008. Both the spatial structure as well as the magnitude of variation in the climatological pattern of surface air temperature and precipitation fields clearly demonstrate that HiRAM AGCM replicates effectively to the main features such that it exhibits higher temperature pattern over the tropical regions and cooling patterns over high latitudes and polar regions. Global and regional precipitation distribution, especially in the tropical regions, and associated wind vector patterns are also reasonably well reproduced by the model. Converging and diverging wind patterns at the tropical belt as well as low-pressure systems and associated cyclonic features in the Northern Atlantic and the Northern Pacific regions are consistent among HiRAM simulation and CFS Reanalysis product. This analysis increased my confidence in the usage of HiRAM model to study the direct and indirect regional impacts of volcanism.

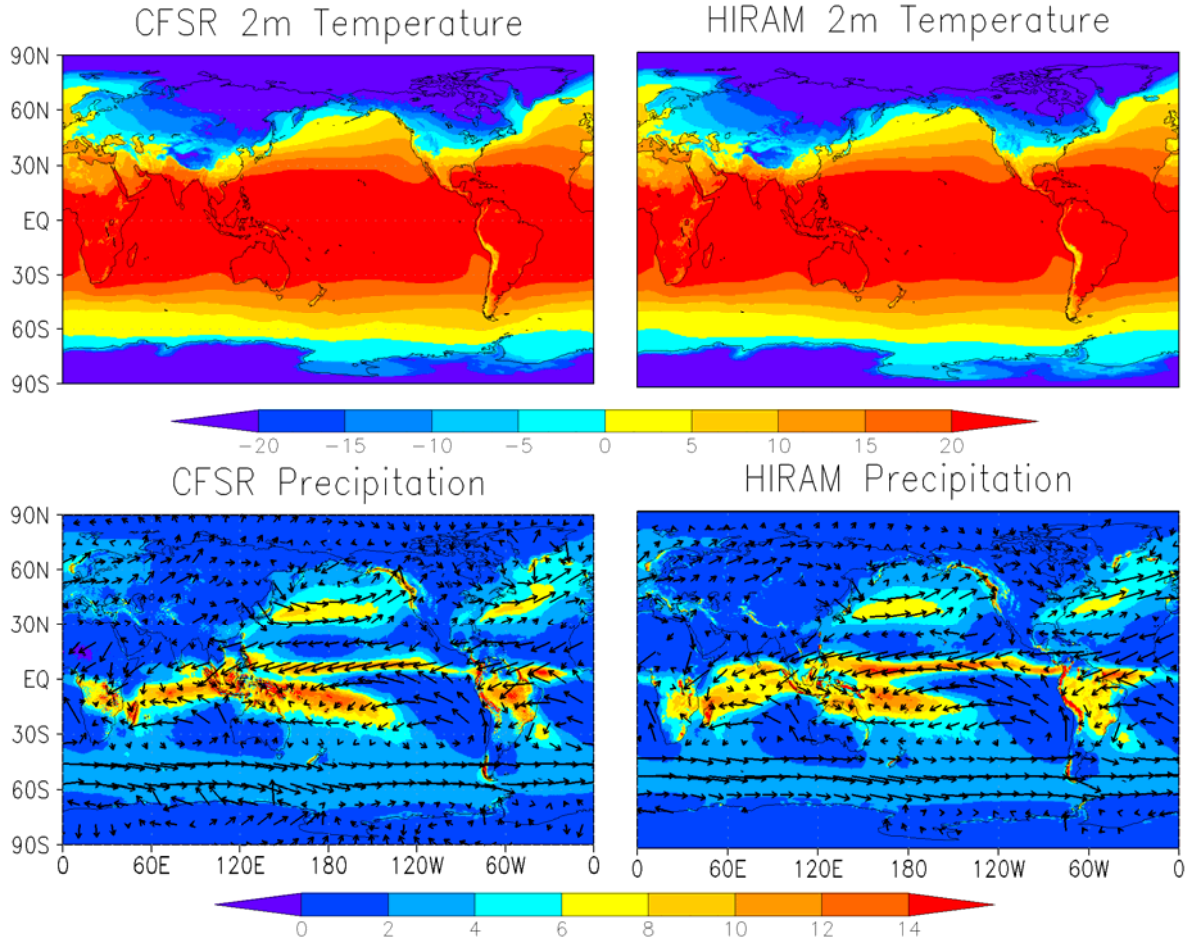


**Figure 3.1:** Mean pattern of 2m surface air temperature ( $^{\circ}\text{C}$  in top) and precipitation (mm/day in bottom) in winter (DJF) season produced using CFSR (left panel) and HIRAM simulation (right panel) overlaid with mean wind vectors at 925 hPa.

### 3.3. Multiple Regression Analysis

The multiple linear regression (MLR) technique is an extension of the simple linear regression that is used when more than one independent factor (also referred as a predictor, regressor or controlled variable) affects a dependent variable (also referred as a criterion variable, response variable, measured variable, outcome, regressand or predictand). Multiple linear regression analysis helps to detect change in dependent variable following the change in independent variables. As outcome or dependent variables I choose  $T_W^i(\lambda, \phi)$  - winter temperature anomaly,  $P_W^i(\lambda, \phi)$  - winter precipitation anomaly,  $T_S^i(\lambda, \phi)$  - summer temperature anomaly and  $P_S^i(\lambda, \phi)$  - summer precipitation anomaly, which are functions of longitude  $\lambda$ , latitude  $\phi$  and the time index  $i$ , which reflects the year of a season and spans all years in the dataset. I choose the following

indices (Figure 3.2) as input predictors in the multiple regression analysis (see Section 3.6 for details regarding selection of relevant predictor variables for MENA region):

Trend index  $\alpha_{TR}^i$  - the standardized year of the season,

ENSO index  $\alpha_{ENSO}^i$  - the standardized DJF NINO3.4 based ENSO index,

NAO index  $\alpha_{NAO}^i$  - the standardized DJF NAO index of Hurrell (1995), and

ISM index  $\alpha_{ISM}^i$  - the standardized JJA Indian summer monsoon (ISM) rainfall index,

which depend only on the time index  $i$ . Since all the predictors are standardized, the regression relations take the following forms for winter (DJF) season:

$$T_W^i(\lambda, \phi) = \alpha_{TR}^i \times T_{TR}^W(\lambda, \phi) + \alpha_{ENSO}^i \times T_{ENSO}^W(\lambda, \phi) + \alpha_{NAO}^i \times T_{NAO}^W(\lambda, \phi) \quad (1)$$

$$P_W^i(\lambda, \phi) = \alpha_{TR}^i \times P_{TR}^W(\lambda, \phi) + \alpha_{ENSO}^i \times P_{ENSO}^W(\lambda, \phi) + \alpha_{NAO}^i \times P_{NAO}^W(\lambda, \phi) \quad (2)$$

and for summer (JJA) season:

$$T_S^i(\lambda, \phi) = \alpha_{TR}^i \times T_{TR}^S(\lambda, \phi) + \alpha_{ENSO}^i \times T_{ENSO}^S(\lambda, \phi) + \alpha_{ISM}^i \times T_{ISM}^S(\lambda, \phi) \quad (3)$$

$$P_S^i(\lambda, \phi) = \alpha_{TR}^i \times P_{TR}^S(\lambda, \phi) + \alpha_{ENSO}^i \times P_{ENSO}^S(\lambda, \phi) + \alpha_{ISM}^i \times P_{ISM}^S(\lambda, \phi) \quad (4)$$

where  $T_{TR}^{W,S}$ ,  $P_{TR}^{W,S}$ ,  $T_{ENSO}^{W,S}$ ,  $P_{ENSO}^{W,S}$ ,  $T_{NAO}^W$ ,  $P_{NAO}^W$ ,  $T_{ISM}^S$ ,  $P_{ISM}^S$  are the regression coefficients that for each  $(\lambda, \phi)$  can be obtained from the following systems of linear equations for the winter (DJF) season:

$$\text{Cov}(\alpha_{TR}^i, T_W^i) = T_{TR}^W + \text{cov}(\alpha_{TR}^i, \alpha_{ENSO}^i) \times T_{ENSO}^W + \text{cov}(\alpha_{TR}^i, \alpha_{NAO}^i) \times T_{NAO}^W$$

$$\text{Cov}(\alpha_{ENSO}^i, T_W^i) = \text{cov}(\alpha_{TR}^i, \alpha_{ENSO}^i) \times T_{TR}^W + T_{ENSO}^W + \text{cov}(\alpha_{ENSO}^i, \alpha_{NAO}^i) \times T_{NAO}^W$$

$$\text{Cov}(\alpha_{NAO}^i, T_W^i) = \text{cov}(\alpha_{TR}^i, \alpha_{NAO}^i) \times T_{TR}^W + \text{cov}(\alpha_{NAO}^i, \alpha_{ENSO}^i) \times T_{ENSO}^W + T_{NAO}^W$$

$$\text{Cov}(\alpha_{TR}^i, P_W^i) = P_{TR}^W + \text{cov}(\alpha_{TR}^i, \alpha_{ENSO}^i) \times P_{ENSO}^W + \text{cov}(\alpha_{TR}^i, \alpha_{NAO}^i) \times P_{NAO}^W$$

$$\text{Cov}(\alpha_{ENSO}^i, P_W^i) = \text{cov}(\alpha_{TR}^i, \alpha_{ENSO}^i) \times P_{TR}^W + P_{ENSO}^W + \text{cov}(\alpha_{ENSO}^i, \alpha_{NAO}^i) \times P_{NAO}^W$$

$$\text{Cov}(\alpha_{NAO}^i, P_W^i) = \text{cov}(\alpha_{TR}^i, \alpha_{NAO}^i) \times P_{TR}^W + \text{cov}(\alpha_{NAO}^i, \alpha_{ENSO}^i) \times P_{ENSO}^W + P_{NAO}^W$$

and for the summer (JJA) season:

$$\text{Cov}(\alpha_{TR}^i, T_S^i) = T_{TR}^S + \text{cov}(\alpha_{TR}^i, \alpha_{ENSO}^i) \times T_{ENSO}^S + \text{cov}(\alpha_{TR}^i, \alpha_{ISM}^i) \times T_{ISM}^S$$

$$\text{Cov}(\alpha_{ENSO}^i, T_S^i) = \text{cov}(\alpha_{TR}^i, \alpha_{ENSO}^i) \times T_{TR}^S + T_{ENSO}^S + \text{cov}(\alpha_{ENSO}^i, \alpha_{ISM}^i) \times T_{ISM}^S$$

$$\text{Cov}(\alpha_{NAO}^i, T_S^i) = \text{cov}(\alpha_{TR}^i, \alpha_{NAO}^i) \times T_{TR}^S + \text{cov}(\alpha_{NAO}^i, \alpha_{ENSO}^i) \times T_{ENSO}^S + T_{ISM}^S$$

$$\text{Cov}(\alpha_{TR}^i, P_S^i) = P_{TR}^S + \text{cov}(\alpha_{TR}^i, \alpha_{ENSO}^i) \times P_{ENSO}^S + \text{cov}(\alpha_{TR}^i, \alpha_{ISM}^i) \times P_{ISM}^S$$

$$\text{Cov}(\alpha_{ENSO}^i, P_S^i) = \text{cov}(\alpha_{TR}^i, \alpha_{ENSO}^i) \times P_{TR}^S + P_{ENSO}^S + \text{cov}(\alpha_{ENSO}^i, \alpha_{ISM}^i) \times P_{ISM}^S$$

$$\text{Cov}(\alpha_{NAO}^i, P_S^i) = \text{cov}(\alpha_{TR}^i, \alpha_{NAO}^i) \times P_{TR}^S + \text{cov}(\alpha_{NAO}^i, \alpha_{ENSO}^i) \times P_{ENSO}^S + P_{ISM}^S$$

Where Cov is the covariance operator. For further details see (Gujarati, 2009). It is important to mention here that the multiple regression approach discussed above will be used to delineate the volcanic aerosol's direct and indirect impacts over MENA (see chapter 4 and appendices for details regarding volcanic effect of El Chichón and Pinatubo eruptions over the MENA region). The residuals in (1-4) are treated as a direct volcanic effect similar to earlier studies (Randel, 2010; Fujiwara et al., 2015; Gu and Adler, 2010; Gu and Adler, 2011). The residual approach is considered to avoid losing accuracy in calculations due to close correlations between the ENSO and volcanic impacts, as both the El Chichón and Pinatubo eruptions occurred in El Niño years.

For polynomial (cubic polynomial) regression, that is used to consider polynomial trend (see Section 3.5 and 4.4.6), the regression relations take the following forms for winter (DJF) season:

$$\begin{aligned}
T_W^i(\lambda, \phi) &= [\alpha_{TR}^i \times T_{TR,1}^W(\lambda, \phi) + (\alpha_{TR}^i)^2 \times T_{TR,2}^W(\lambda, \phi) + (\alpha_{TR}^i)^3 \times T_{TR,3}^W(\lambda, \phi)] \\
&\quad + \alpha_{ENSO}^i \times T_{ENSO}^W(\lambda, \phi) + \alpha_{NAO}^i \times T_{NAO}^W(\lambda, \phi) \quad (5) \\
P_W^i(\lambda, \phi) &= [\alpha_{TR}^i \times P_{TR,1}^W(\lambda, \phi) + (\alpha_{TR}^i)^2 \times P_{TR,2}^W(\lambda, \phi) + (\alpha_{TR}^i)^3 \times P_{TR,3}^W(\lambda, \phi)] \\
&\quad + \alpha_{ENSO}^i \times P_{ENSO}^W(\lambda, \phi) + \alpha_{NAO}^i \times P_{NAO}^W(\lambda, \phi) \quad (6)
\end{aligned}$$

and for summer (JJA) season:

$$\begin{aligned}
T_W^i(\lambda, \phi) &= [\alpha_{TR}^i \times T_{TR,1}^S(\lambda, \phi) + (\alpha_{TR}^i)^2 \times T_{TR,2}^S(\lambda, \phi) + (\alpha_{TR}^i)^3 \times T_{TR,3}^S(\lambda, \phi)] \\
&\quad + \alpha_{ENSO}^i \times T_{ENSO}^S(\lambda, \phi) + \alpha_{NAO}^i \times T_{ISM}^S(\lambda, \phi) \quad (7) \\
P_W^i(\lambda, \phi) &= [\alpha_{TR}^i \times P_{TR,1}^S(\lambda, \phi) + (\alpha_{TR}^i)^2 \times P_{TR,2}^S(\lambda, \phi) + (\alpha_{TR}^i)^3 \times P_{TR,3}^S(\lambda, \phi)] \\
&\quad + \alpha_{ENSO}^i \times P_{ENSO}^S(\lambda, \phi) + \alpha_{ISM}^i \times P_{ISM}^S(\lambda, \phi) \quad (8)
\end{aligned}$$

Where  $T_{TR,1}^{W,S}$ ,  $P_{TR,1}^{W,S}$ ,  $T_{TR,2}^{W,S}$ ,  $P_{TR,2}^{W,S}$ ,  $T_{TR,3}^{W,S}$ ,  $P_{TR,3}^{W,S}$  represent to polynomial trend based regression coefficients of temperature and precipitation with linear, quadratic and cubic components in winter (W) and summer (S) seasons.

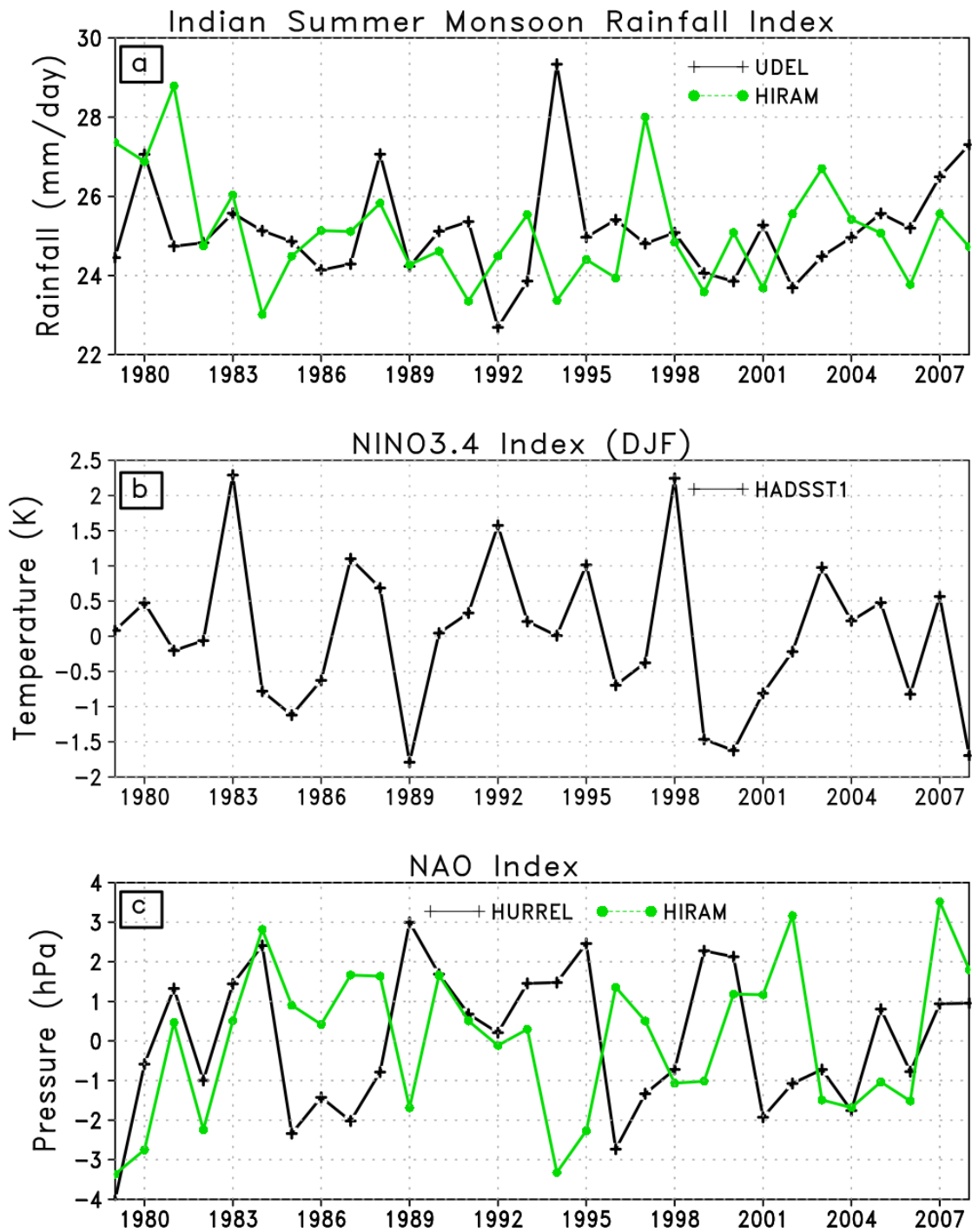


**Figure 3.2:** Time series of predictors (not standardized) from the observations and HiRAM used in the regression analysis in both seasons a) Indian Monsoon Rainfall Index, which shows the total summer rainfall computed over the entire Indian region b) NINO3.4/DJF, c) NAO Index of Hurrell (1995).

Hereafter, I will analyze the patterns of temperature and precipitation trends and regression coefficients of the leading climate modes for the MENA region based on the multiple regression analysis.

#### **3.4. Temperature and Precipitation Linear Trends**

Figure 3.3 and Figure 3.4 show winter and summer decadal trend respectively of MENA temperature/precipitation (top/bottom) fields, which are calculated using MLR analysis over the period 1979-2008. The trend in HiRAM simulations and observed data set shows a strong spatial and seasonal variability with an overall increase of both the temperature and precipitation, although important disagreements between the UDEL observations and model output are found. The spatial distribution of the winter decadal temperature trend over the entire MENA region (Figure 3.3) shows that the temperature has an overall growing trend that reaches to 0.5 K/decade both in the UDEL observation and HiRAM output. There exists some spatial inconsistency between observation and model results such that the UDEL observations show maximum warming over Central Africa, especially over Sudan, Niger and Mauritania, whereas, the model shows a maximum warming trend over the northeastern part of the selected domain, especially, over Iran, Afghanistan and Turkmenistan. Moreover, observations show a decreasing trend that reaches up to -0.5 K per decade over Turkey, Syria and Iraq whereas, the model does not capture this pattern; instead it displays an increasing trend distribution over these areas. The decadal trend in winter precipitation shows a mixed pattern with an overall increasing trend over the tropical regions and a decreasing pattern over parts of Southern Europe, Arabian Peninsula and Iran both in the model and observations. The trend distribution of precipitation in winter is largely in agreement (both quantitatively and qualitatively) between the model and UDEL observations, except over Sudan and the Iberian Peninsula where they show a different spatial structure. The possible difference of the spatial structure and magnitude of the trend between the model and observation could be accounted for by the internal natural climate variability signal, as it needs not to be the same between the model and observation.

Alike its winter counterpart, the long-term trend of temperature in summer is also rising over the entire MENA region except in the tropical areas, where, I observe a decreasing tendency both in the model and the observations (Figure 3.4). That could be accounted for by the increased water vapor and cloud distributions caused by the increased land-sea thermal gradient in summer season. Moreover, the decadal trend of temperature in summer over the northern half of the selected domain is larger which peaks at 1 K per decade compared to the southern part of the domain that peaks at 0.5 K per decade, predominantly in the observations. The summer

precipitation shows an overall increasing trend, especially over the tropical belt. Moreover, the precipitation shows a dipole structure, with a rising trend over the northern areas of the tropics and a decreasing trend southward of 10°N especially in the UDEL observations. The trend pattern of temperature and precipitation in summer season is relatively more consistent between the model and observation compared to the winter counterpart, suggesting that model performs reasonably well in summer. The presented trend maps both for winter and summer seasons, show that the climate trends could add uncertainty in the forcings-induced climate signals, and therefore need to be filtered out while examining temperature and precipitation changes caused by internal and external climate forcing factors such as volcanism, NAO and ENSO (see chapter 4 for details). The presented long-term decadal trend results are consistent with earlier studies (e.g., Athar, 2014; Krishna, 2014), which also show an overall increasing trend. I further find that the values of the decadal trend of temperature, especially in the northern part of the selected domain are relatively larger in summer than in winter. Moreover, the decadal trend of temperatures in both the seasons has statistically significant and relatively larger trend values, which are spatially more widespread compared to the precipitation decadal trend values.

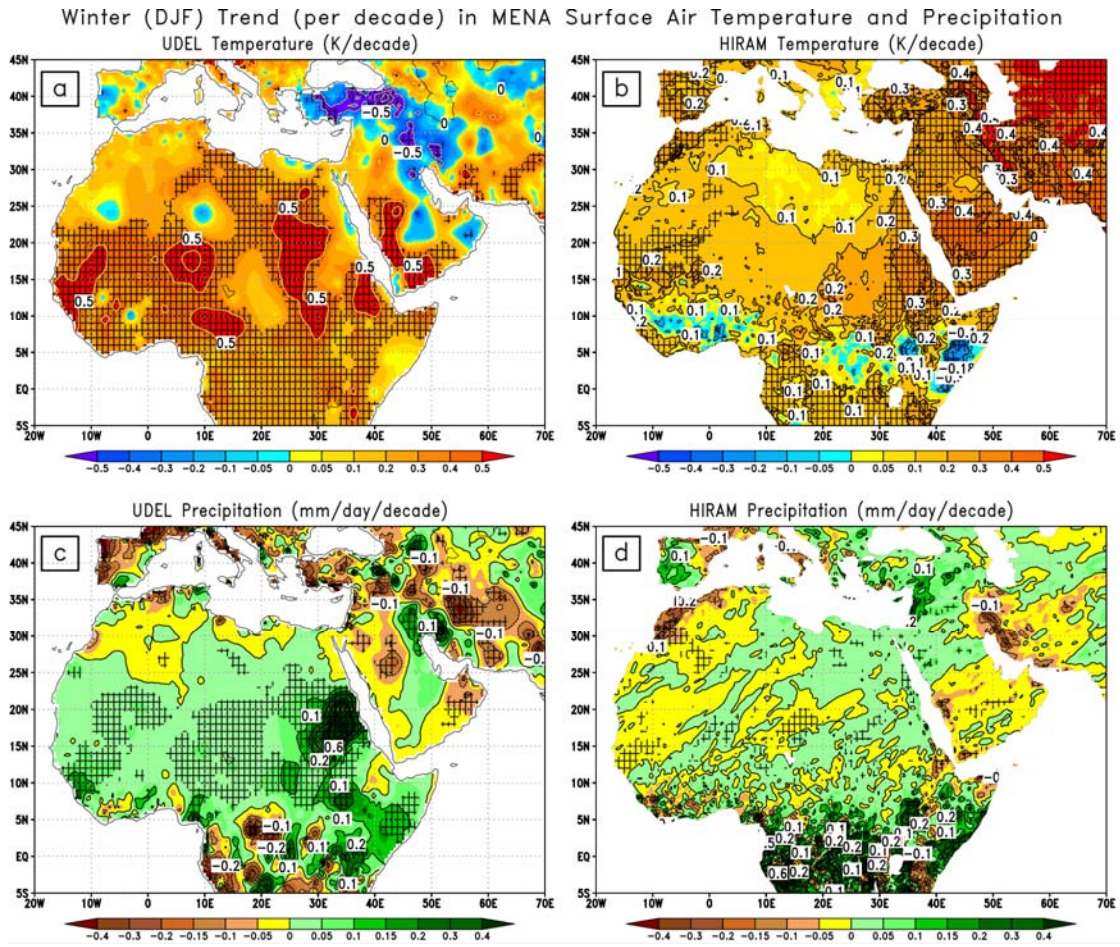


**Figure 3.3:** The spatial distributions of the trends (per decade) of winter (DJF) temperature over the period of 1979-2008 using (a) UDEL, (b) HiRAM output and trend in Precipitation using (c) UDEL and (d) HiRAM output. Hatching indicates statistically significant decadal trends at 95% confidence level that is computed using two-tailed student t-test.

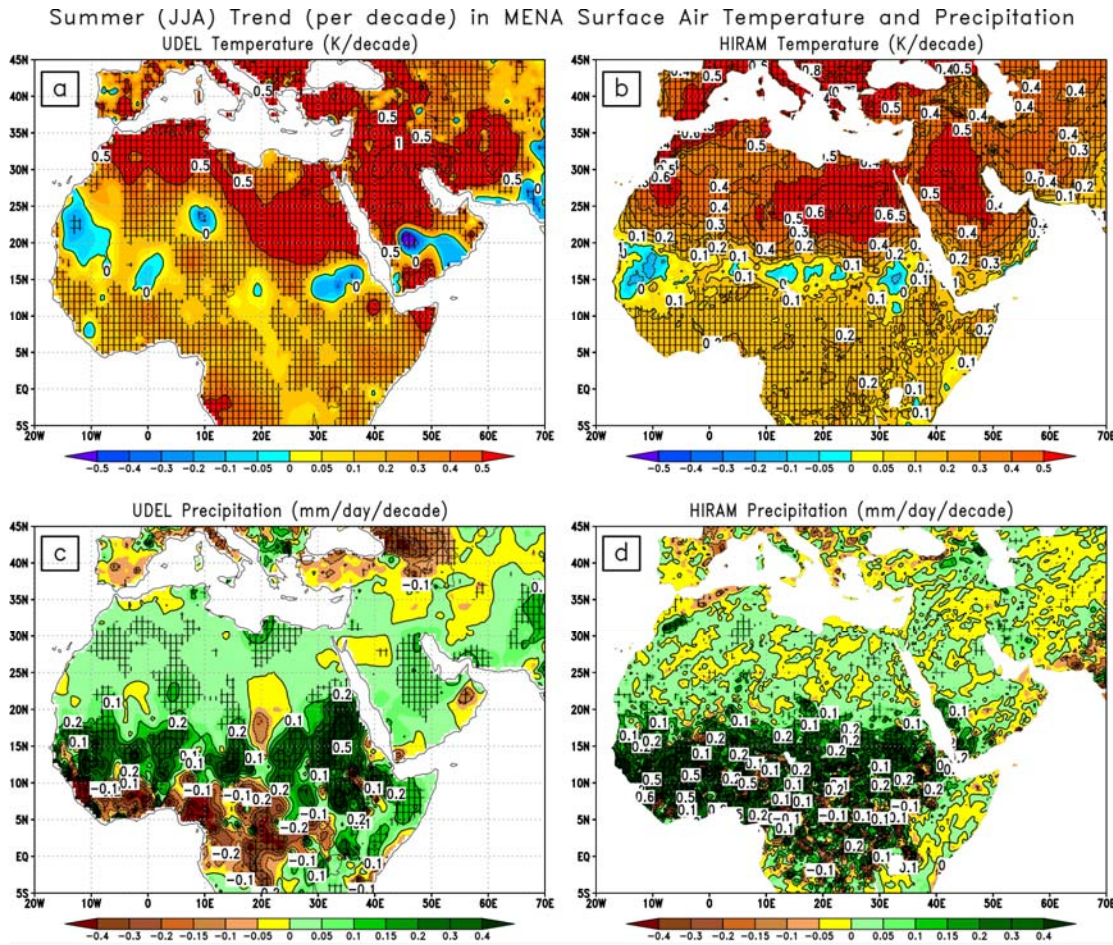


**Figure 3.4:** Same as Figure 3.3 but for the trends in summer (JJA).

### 3.5. Temperature and Precipitation Polynomial Trends

To see the robustness of temperature and precipitation trends and to further understand the long term climatic changes over MENA region, I extended the trend analysis over a longer period 1900-2008 and computed trends in the temperature and precipitation fields using UDEL observed data set. For this purpose I computed polynomial trends (Section 3.3, equation 5-8), as the trends over longer period are not linear. Figure 3.5 shows polynomial trend curve computed by averaging over the entire MENA region (20°W-70°E, 5°S-45°N) for both the seasons. The polynomial trend over the longer period reveals that the MENA temperature has an overall increasing trend whereas precipitation has a decreasing trend. However, the long-term temporal evolution of temperature trend both in the winter and summer season shows an increasing trend curve for initial few decades and then it decreases for the period 1920-1970. The decrease in temperature trend is more obvious in summer season than in winter. After year 1970 the

temperature trend increases again. The polynomial trend of precipitation over MENA region has a downtrend for the entire period of analysis in both the seasons such that the decrease is slow in the initial decades and then it becomes relatively more pronounced especially after year 1920. This analysis of trend using polynomial approach suggests that one has to consider removing polynomial trend from the data while considering analysis over longer period of time, which is 1900-2008 in my case. The temperature and precipitation anomaly for both the seasons before (red curve) and after (green curve) removing polynomial trend is also shown in Figure 3.5, indicating that the trends adds significant part in the anomaly signal and therefore need to be filtered out while considering climatic impact assessment for the MENA region.

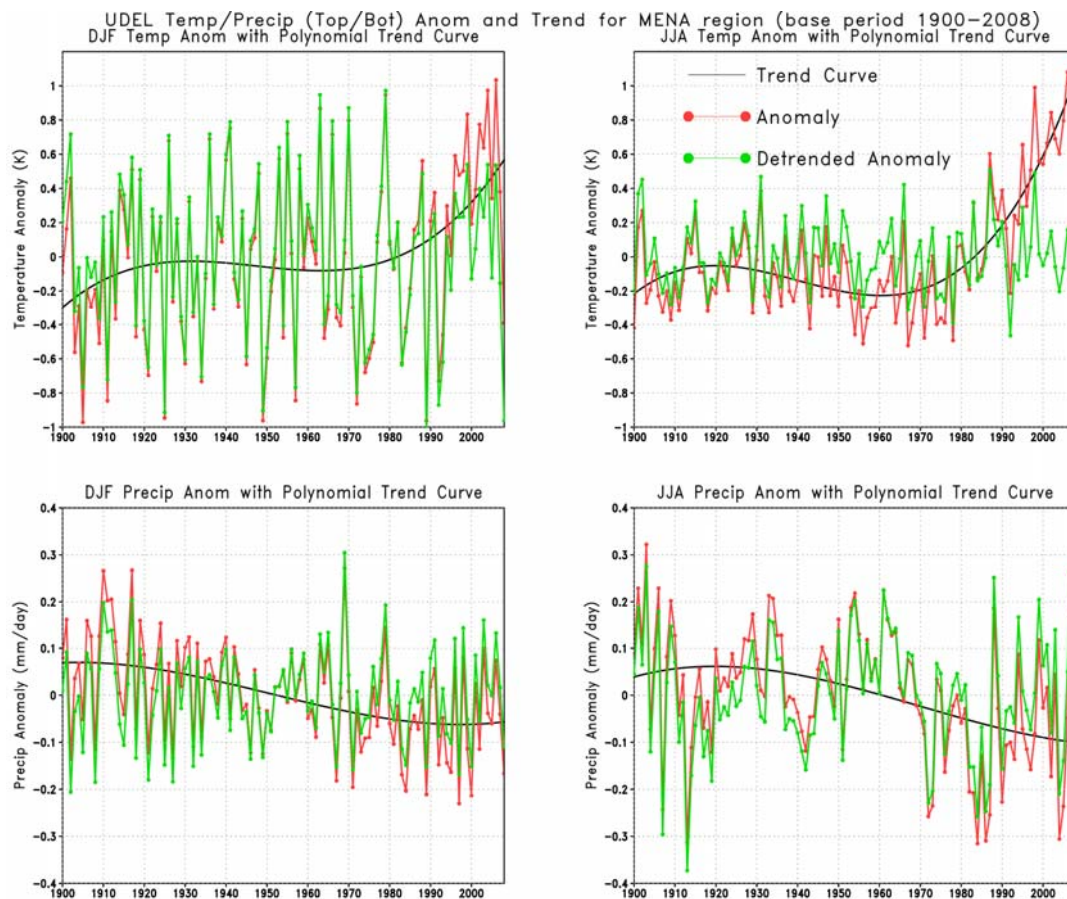


**Figure 3.5:** The polynomial trend curve for temperature/precipitation (top/bottom) fields in winter/summer (left/right) computed over MENA region over a longer period of 1900-2008. The anomalies of temperature and precipitation before (red curve) and after removing polynomial trend (green curve) are also shown.

### 3.6. Selection of Leading Predictors for MENA Region

It has been discussed in several studies that the North Atlantic Oscillation (NAO) is one of the primary modes of atmospheric variability in the North Atlantic sector that largely impacts the

climate of Europe and MENA (Hurrell, 1995; Yu and Zhou, 2004; Abualnaja et al., 2015; Athar, 2015; Barlow et al., 2016). ENSO and Indian Monsoon have also been reported as important modes of variability that impact MENA climate (Wanner et al., 2001; Abualnaja et al., 2015; Athar, 2015; Athar and Ammar, 2016; Chakraborty et al., 2006). Wanner et al. (2001) and Athar (2015) have shown that both the NAO and ENSO are the prominent modes of variabilities that are essential to be considered while discussing Northern Hemisphere winter climate, especially, the climate of Arabian Peninsula region. There are other modes of variabilities with origin in the Atlantic sector such as East Atlantic (EA) and East Atlantic West Russia (EA/WR) patterns that presumably impact climate of Europe and the Middle East, however, Krichak et al. (2002) have discussed that the impact of EA/WR over Middle East is much less compared to NAO and ENSO impact. They further showed that the precipitation anomalies induced by EA/WR pattern over these regions are not significant. In recent studies, it has been discussed that the EA/WR's pattern impacts Eastern North America and Eurasia including the Ural Mountains, Northeastern Africa and the Middle East region. However, these studies suggest that this variability pattern is modulated by NAO oscillation, as both are closely associated (Lim, 2015). Wanner et al. (2001) further suggest that the variability in the North Atlantic sector and associated global and regional impacts are largely explained by NAO pattern in the North Atlantic Ocean. I also tested the impact of the Indian Ocean Dipole (IOD) on the MENA region by including IOD normalized index in the regression analysis and found it negligibly small.

Based on the above discussion, I anticipate that considering NAO and ENSO as leading patterns would be enough to account for most of the variability over MENA region in the winter season. Similarly ENSO and Indian summer monsoon (ISM) appear to have significant contribution in summer season over MENA (Almazroui et al., 2012; Athar, 2015; Abualnaja et al., 2015; Athar and Ammar, 2016). In the subsequent section I will analyze the NAO, ENSO and ISM regression coefficients and their climatic relevance for MENA domain.

### **3.7. NAO, ENSO and ISM Impacts**

Using multiple linear regression analysis (see Section 3.3 for details), I computed regression coefficients of ENSO, NAO and Indian Summer Monsoon, which explain their long-term seasonal summer and winter climatic impact on MENA temperature and precipitation fields. The regression coefficient maps are helpful to summarize our understanding of consistent NAO, ENSO and Indian monsoon relations with MENA surface temperature and precipitation fields. As discussed above, the selections of the predictors used in multiple regression analysis are based on their strong correlation with MENA climate as well as their significant climatic impact

discussed in the previous literature (see Section 3.6 for details regarding the selection of independent input variables for MENA region in the winter and summer seasons). These regression coefficients represent the mean change in the dependent variable (temperature or precipitation) for one unit change in the corresponding predictor variable while holding the other predictors to be constant. In the following sections (i.e., 3.7.1, 3.7.2 and 3.7.3) I will discuss each factor in detail.

### **3.7.1. NAO**

The NAO plays a significant role to characterize the atmosphere of Europe and Middle East region (Hurrell, 1995; Wallace and Gutzler 1981; van Loon and Rogers, 1978; Cullen et al., 2002; Iqbal et al., 2013). Figure 3.6 displays NAO correlation coefficient with surface air temperature of Eurasia and MENA in winter and summer seasons computed using UDEL observation and HiRAM model over a period of 1979-2008. Both the model and observation depicts highly significant positive correlation in winter over northern part of Eurasia suggesting that the positive NAO phase significantly warms the northern part of Europe and Asia. Similarly I observed that NAO is negatively correlated with winter temperature of Southern Europe and MENA and its cooling impact further extends to South and East Asia. Spatial structure of NAO correlation with winter temperature over Europe and MENA region shows a dipole nature with positive correlation over Northern Europe and Siberia and negative correlation over mid latitude MENA domain. This suggests that the positive phase of NAO brings cooler and drier air into the Southern Europe and Middle East region, whereas negative phase brings warm and wet conditions over this region. The spatial patterns of temperature and precipitation fields clearly reveal that positive NAO will induce a cooling and drying pattern in winter. Temperature response to NAO circulation in winter is anticipated to be larger and more pronounced than in summer season because NAO correlation in winter with MENA temperature is much higher (Figure 3.5) than corresponding correlation in summer (Bladé et al., 2012, Hurrell et al., 2003; Iles and Hegerl, 2017). The absolute magnitude of NAO correlation coefficient in winter peaks at 0.6 and 0.8 respectively in the model and observations (Figure 3.6). These values are statistically significant at 95% confidence level, suggesting that the NAO circulation plays a significant role to characterize climatic changes over MENA region in winter. HiRAM simulation slightly underestimates the magnitude of NAO correlation coefficient in winter season although overall spatial distribution is well captured by the model.

To further understand how the change in NAO influences the MENA region I looked at the NAO regression coefficient with MENA surface air temperature and precipitation. Figure 3.7

shows the map of regression coefficient of NAO respectively in winter season computed using multiple regression analysis, which explains the fractions of the variance of temperature and precipitation caused by NAO over MENA region. A detailed methodology dealing with the selection of these input explanatory variables, along with their importance for MENA region has been discussed in Section 3.6.

The positive phase of NAO causes strong cooling (that peaks at 0.6 in UDEL and 0.4 in the model response) in winter especially over the Arabian Peninsula region (Figure 3.7), which is consistent with earlier studies that used simple linear regression (see, e.g., Yu and Zhou, 2004; Iles and Hegerl, 2017). Moreover, the positive NAO phase results in weakening of rainfall over the entire MENA region, mainly over Southern Europe extending to Iraq and Iran. The NAO induced patterns are largely consistent between the model and observation. The patterns of NAO regression coefficients, both for UDEL observation and HiRAM output represent statistically significant response over the entire MENA region. Moreover, it is observed that the NAO based temperature and precipitation changes in summer season over the MENA are weaker. It happens because the NAO correlation with MENA temperature in summer season is weaker (Figure 3.6, lower panel). These results are consistent with earlier studies (Bladé et al., 2012, Hurrell et al., 2003; Iles and Hegerl, 2017).

### **3.7.2. ENSO**

The ENSO atmospheric teleconnections is considered as the leading mode of variability that causes profound effect on global and regional climate and weather events. It has been shown that the climate of Middle East in particular the Arabian Peninsula region is strongly impacted by ENSO (Barlow et al., 2016; Athar and Ammar, 2016). In this section I emphasized that both the El Niño and La Nina are important modes of variability that should be taken into account while discussing leading climate forcing factors and their climatic impacts in the Middle East and North Africa region. By modulating the near-equatorial zonal atmospheric overturning circulation i.e. the Walker circulation, ENSO atmospheric teleconnections induce changes in cloud cover and evaporation in remote ocean basins such as the Arabian Sea, Indian Ocean, and the tropical North Atlantic Ocean that in turn affects the land regions of Middle East and Asia (Klein et al., 1999; Wang, 2002; Barlow et al., 2016). For example, during a developing period of El Niño, the Walker circulation moves to the east, resulting in anomalous atmospheric subsidence over the Indian Ocean region and consequent suppression of convection there. This ENSO-induced changes leads to warming in the Indian Ocean through intensified solar radiation as well as a weakening land-sea contrast in summer, resulting in less Indian summer monsoon rainfall

(Barlow et al., 2016). Moreover, ENSO (El Niño/La Nina) are reported to produce increased/decreased precipitation activity over tropical MENA region by inducing thermal changes in the Indian and Atlantic Ocean in winter season and the reverse is observed for summer season (Barlow et al., 2016). To see long-term ENSO influences over the MENA region I have analyzed their regression coefficients using multiple regression analysis.

Figure 3.8 show the map of regression coefficients of ENSO respectively in winter season computed using multiple regression analysis, which explains the fractions of the variance of temperature and precipitation caused by ENSO over MENA region. A detailed methodology dealing with the selection of these input explanatory variables, along with their importance for MENA region has been discussed in Section 3.6.

The warming phase of ENSO (i.e., El Niño) results in cooling over Arabian Peninsula and warming over Northwestern as well as tropical parts of Africa (Figure 3.8). Moreover, the El Niño phase shows increased precipitation over the horn of Africa as well as over North Eastern part, in particular over Iraq and Iran domain. The model shows slightly weaker regression coefficient values than the observations and the spatial patterns are also somewhat shifted in the model compared to observation. The ENSO (El Niño/La Nina) regression coefficients show that the temperature change (cooling/warming) caused by ENSO reaches a maximum value of 0.6/0.2 in the observation and 0.1/0.2 in the model. However, these cooling/warming impacts are statistically significant especially in the observations, suggesting that ENSO produces substantial climatic signal over MENA region in the winter season.

The MENA region is also strongly influenced by ENSO in summer season as explained by the ENSO regression coefficients for temperature and precipitation (Figure 3.9). The ENSO (El Niño/La Nina) results in warming/cooling and decreased/increased precipitation over the tropical rain belt regions of MENA in summer.

### **3.7.3. Indian summer monsoon**

Several studies have emphasized that the global monsoon systems, especially the Indian and African monsoons are strongly affected by the internal and external climate forcing factors (Oman et al., 2006; Trenberth and Dai, 2007; Anchukaitis et al., 2010; Joseph and Zeng, 2011; Liu et al., 2016; Robock and Liu, 1994; Robock et al., 2008). It has also been observed that the temperature and rainfall distribution of the MENA tropical region in summer is largely characterized by the strength of its monsoon system (Rodwell and Hoskins, 1996; Sultan and Janicot, 2000). External forcings such as explosive eruptions induce weakening to the monsoon system (Oman et al., 2006; Liu et al., 2016) and affect the position of ITCZ (Haywood et al.,

2013). Earlier studies have shown that Indian and African monsoon systems are tightly linked to the rising branch of local Hadley Cell, also known as ITCZ (Joseph and Zeng, 2011; Wegman et al., 2014). Hence, the Indian and African monsoons are affected by the climate forcings-induced seasonal changes in the ITCZ (Wegman et al., 2014). In the summer season, ITCZ moves northward as a result of climate forcings-induced thermal gradient between land and ocean. This inter-hemispheric gradient drives Hadley circulation. A decreased land-sea thermal gradient following external or internal forcings suppresses the northward migration of ITCZ that result in a decreased amount of clouds and associated decrease in rainfall over the tropical ITCZ region. Moreover, the tropical climate of the Arabian Peninsula and East Africa region is largely affected by the intensity of the Somali jets that are driven by the strength of the Indian monsoon system. A stronger Indian monsoon system drags immense moisture (through Somali jet) towards the inland region of East Africa (Uganda, South Sudan, Kenya, Somalia, Ethiopia, Djibouti and Eritrea) and southern parts of Arabian Peninsula including Yemen and Oman. This moist wind system (Somali jet) then, following geostrophic wind relation, enters to northern and central India because of the strong low-pressure system over Indian landmass during the summer period. Whereas, a weakened Indian monsoon will have weakened Somali current that will result in less transport of moisture-laden air to Eastern Africa (Aiki et al., 2006) and to the north and Central India that consequently affects rising branch of the Hadley circulation.

A strong teleconnection effect of Indian monsoon on African monsoon system, especially the influence of Indian monsoon on East and West African monsoon onset, was shown in previous studies (Camberlin et al., 2010; Flaounas et al., 2012). Based on regression analysis, I also observed that Indian and African monsoon systems are well correlated and therefore a weakened Indian and African monsoon will produce warming and drying anomaly over tropical MENA region.

As discussed above, the MENA region is strongly influenced by the Indian monsoon in the summer season as explained by the ISM regression coefficient for temperature and precipitation (Figure 3.10). An increased ISM results in decreased/increased (temperature/precipitation) over the tropical parts of the MENA region in summer. The absolute value of ISM regression coefficients for temperature/precipitation fields peaks at 0.4/0.6 and these values are statistically significant, especially over the tropical areas, suggesting that ISM produces significant climatic impact over MENA tropical regions in summer. The spatial pattern of the ISM regression coefficient, especially for temperature case is relatively less smooth in the observations, compared to the model, probably because the observational data face scarcity in observational measurements for this region. However, the model shows much smoother response

(both for temperature and precipitation) presumably because the model results are averaged over three ensemble members that possibly minimize the effect of internal noise. The conducted multiple regression analysis emphasizes that the Indian monsoon modulates the strength of African monsoon and therefore a decreased Indian monsoon will produce a decreased precipitation over the tropical MENA region. Indian monsoon-induced precipitation distribution shows a dipole structure at the Northern Hemisphere tropical region (decreased precipitation northward of  $10^{\circ}\text{N}$  and subsequent increase southward of  $10^{\circ}\text{N}$ ), which could be attributed to the southward shift of ITCZ (Haywood et al., 2013; Liu et al., 2016). This pattern suggests that a significant portion of the total precipitation over the MENA tropical region is controlled by the strength of Indian monsoon as it could cause weakening to the rising branch of NH local Hadley circulation i.e. the ITCZ. A detailed discussion on possible mechanisms and teleconnection between the Asian monsoon system and precipitation changes over MENA (through the monsoon-desert mechanism) can be seen in Rodwell and Hoskins (1996). My results are largely consistent with earlier studies that deal with ENSO and Indian Monsoon changes over the African region using the modeling and observational approaches (Preethi et al., 2015).

From the spatial pattern of temperature and precipitation, it is observed that the temperature and pressure based indices i.e. ENSO and NAO respectively have a higher value of statistically significant regression coefficients and are spatially more widespread compared to the precipitation-based indices, i.e., ISM.

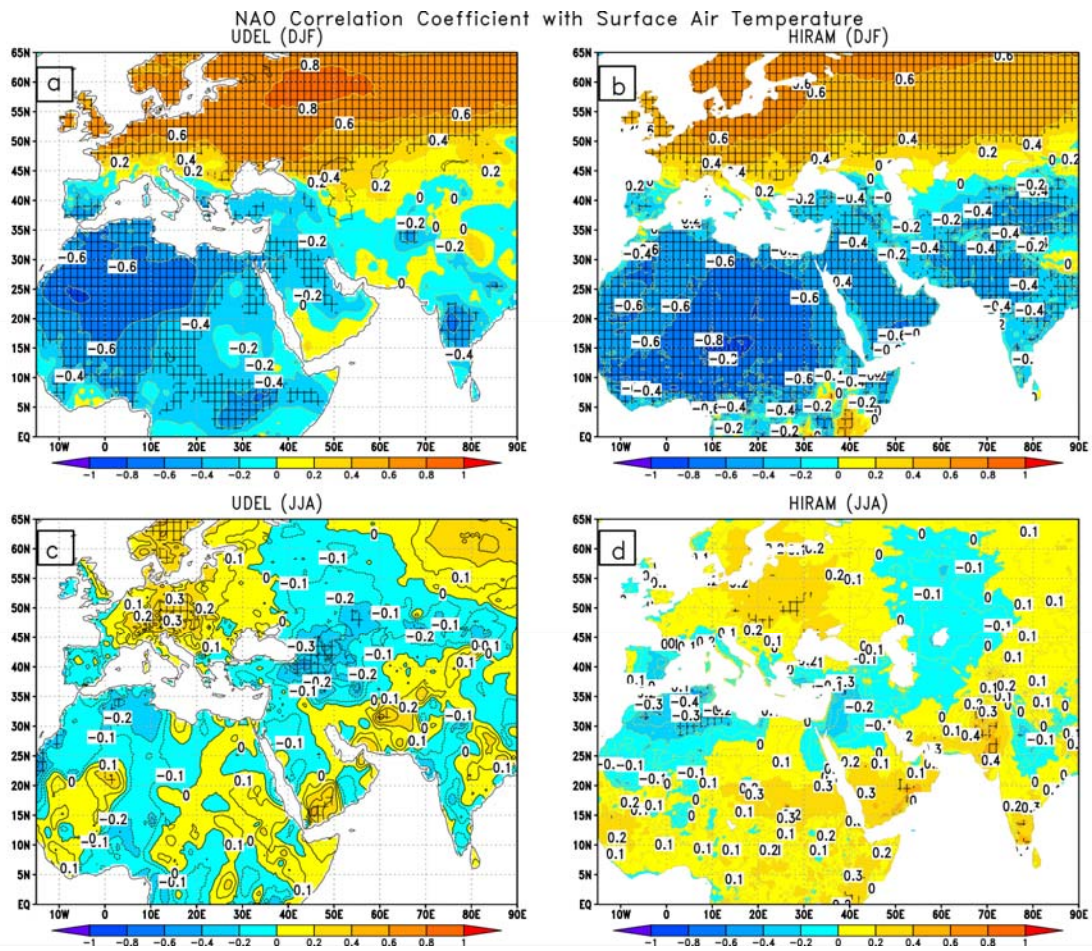


**Figure 3.6:** Winter (DJF) NAO correlation coefficient with surface air-temperature calculated using a) UDEL 30-year winter period, b) Model 30-year winter period, c) UDEL 30-year summer period, d) model 30-year summer period. Hatching shows the statistically significant areas with at least 95% confidence level Hatching indicates statistically significant decadal trends at 95% confidence level that is computed using two-tailed student t-test.

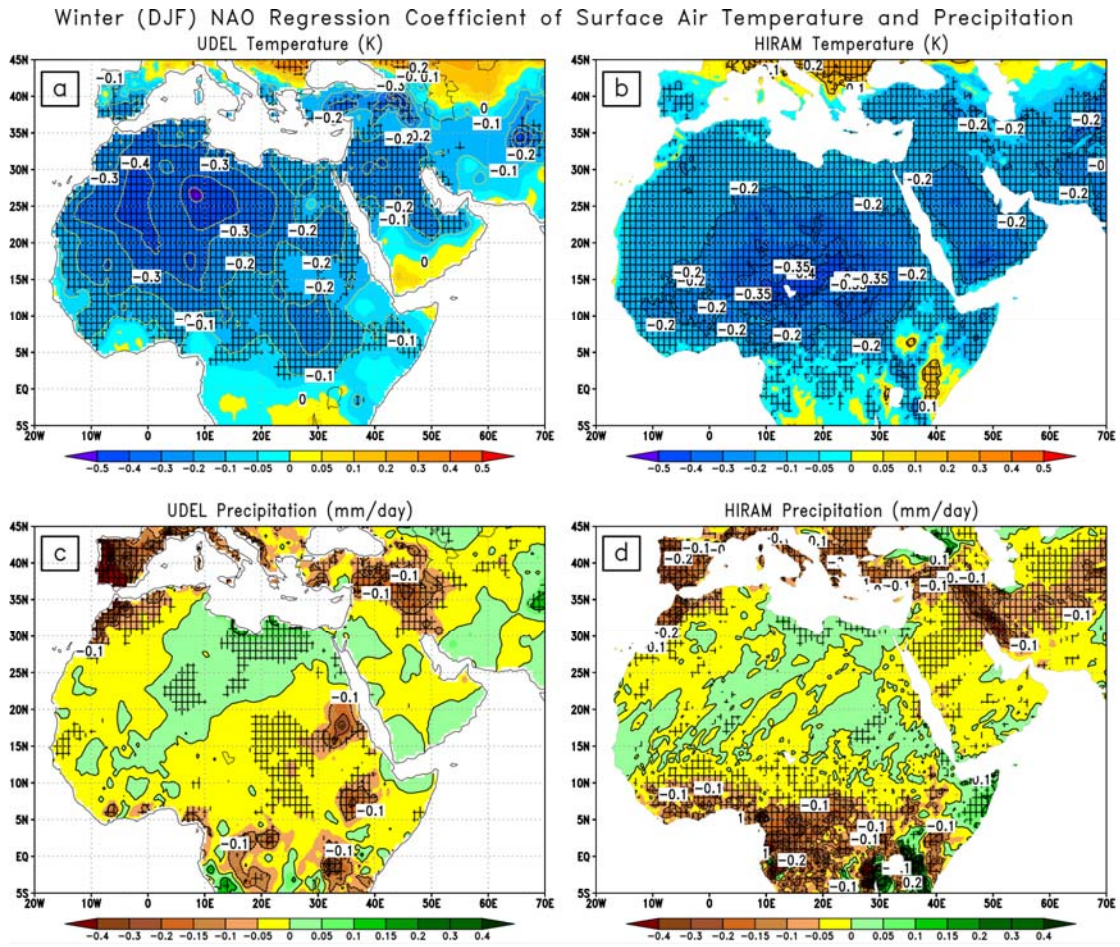


**Figure 3.7:** Winter (DJF) NAO regression coefficient with surface air-temperature (K) calculated using a) UDEL 30-year period, b) Model 30-year period, and with precipitation (mm/day) calculated using c) UDEL 30-year period, d) model 30-year period. Hatching shows the statistically significant areas with at least 95% confidence level.

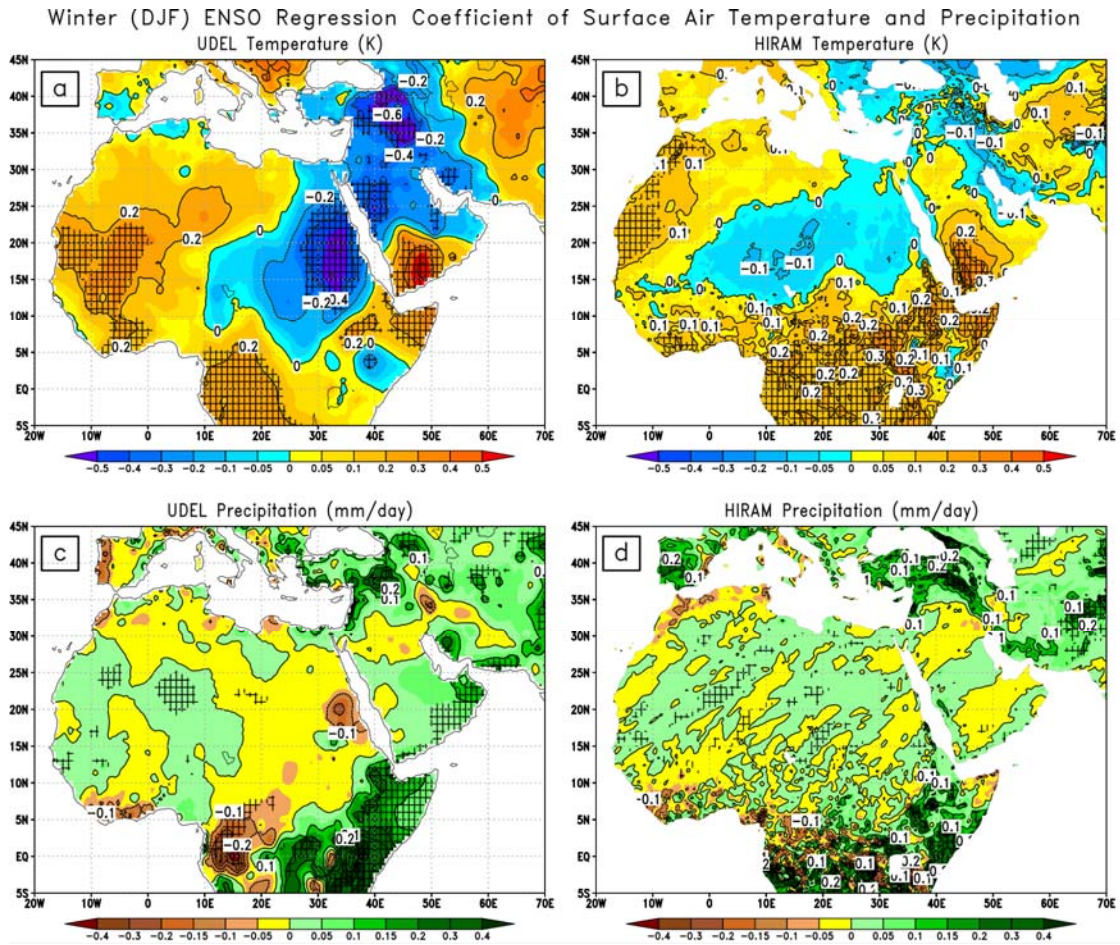


**Figure 3.8:** Winter (DJF) ENSO regression coefficient with surface air-temperature (K) calculated using a) UDEL 30-year period, b) Model 30-year period, and with precipitation (mm/day) calculated using c) UDEL 30-year period, d) model 30-year period. Hatching shows the statistically significant areas with at least 95% confidence level.

Summer (JJA) ENSO Regression Coefficient of Surface Air Temperature and Precipitation

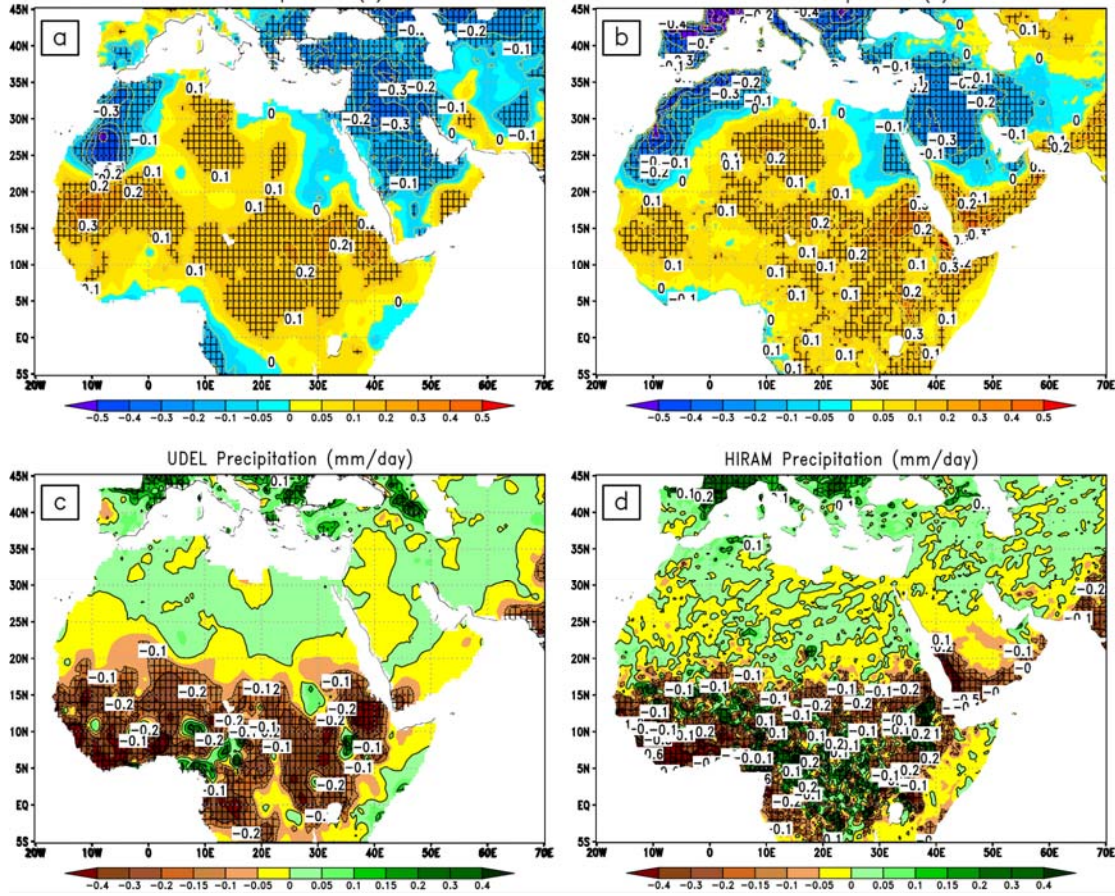


**Figure 3.9:** Summer (JJA) ENSO regression coefficient with surface air-temperature (K) calculated using a) UDEL 30-year period, b) Model 30-year period, and with precipitation (mm/day) calculated using c) UDEL 30-year period, d) model 30-year period. Hatching shows the statistically significant areas with at least 95% confidence level.

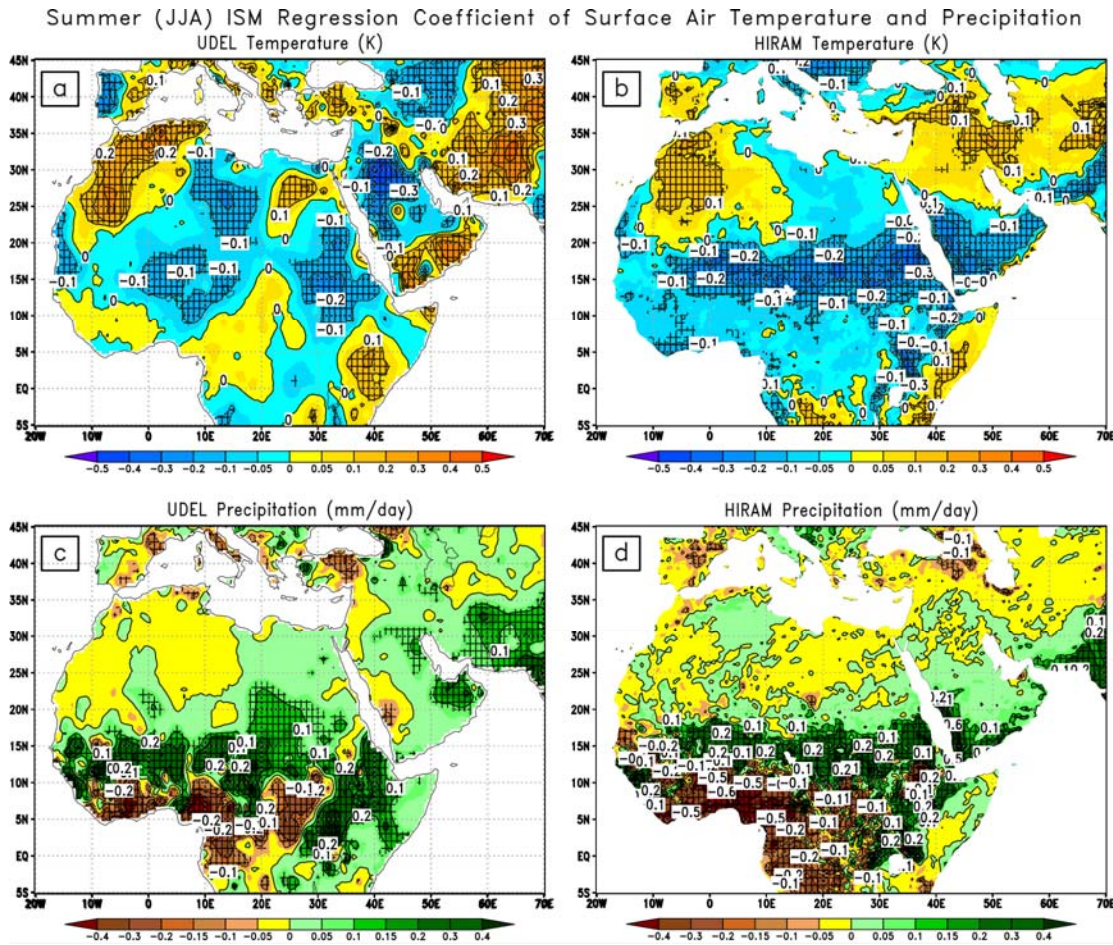


**Figure 3.10:** Summer (JJA) ISM regression coefficient of surface air-temperature (K) calculated using a) UDEL 30-year period, b) Model 30-year period, and with precipitation (mm/day) calculated using c) UDEL 30-year period, d) model 30-year period. Hatching shows the statistically significant areas with at least 95% confidence level.

### 3.8. Summary and Conclusions

Both the climate trends and the regression coefficients of leading climate variability modes are important parameters that are widely used to study the global and regional climatic changes induced by internal and external climate forcings. This chapter focuses on the importance of trend in data and leading climate variability modes that play significant role in shaping MENA climate in winter and summer seasons. As MENA region is very sensitive to the changes induced by the internal (e.g., ENSO, NAO, Indian monsoon) and external (e.g., volcanism) climate forcings, thereby, understanding the processes that govern MENA climatic variability is, therefore, of high priority, especially in the context of global and regional climate change. In order to better understand the climatic impact of leading modes of variabilities (i.e., their spatial structure, temporal evolution, mechanism, and climate variability) over MENA region I used multiple

regression analysis and looked at the impact of leading variability modes over the MENA temperature and precipitation fields. Regression analysis is widely used to identify the spatial patterns of climate change that are associated with internal and forced climate variability. The selection of leading predictors used in multiple regression analysis is based on their importance highlighted in the literature as well as my own assessment based on their strong correlation with MENA temperature and precipitation fields. For the analysis of the trend in data, I computed linear and polynomial trends over the period 1979-2008 and 1900-2008 respectively. I used the polynomial trend for the longer 109-year period (1900-2008), as the trends over longer periods are not linear. For a better comparison of associated climatic impact, the trend and other leading predictors are standardized. The conducted MLR analysis emphasize that the trend in data could add significant contribution (it may add uncertainty or noise) in climate variability pattern of a region and therefore trend-induced contribution need to be filtered out while analyzing the impact of different leading factors. My results further emphasize that NAO, ENSO and Indian monsoon are the leading variability modes that significantly impact the climate of MENA. The positive phase of NAO cause cold and dry climatic changes over the MENA in winter. The impact of NAO in summer is much weaker than its winter counterpart. It is possible because the NAO correlation with MENA temperature in summer is weaker and less significant than its winter counterpart. ENSO (El Niño/La Niña) also induce cold/warm anomalies over the Arabian Peninsula in the winter season. Moreover, ENSO (El Niño/La Niña) brings warm/dry climatic changes especially over the MENA tropical region in the summer season through ENSO-induced thermal changes in the Indian and Atlantic Ocean that in turn affect MENA tropical land areas. Indian monsoon also plays a significant role to characterize the climate of MENA and South Asia in the summer season. A weaker Indian monsoon will cause weakening to Hadley circulation as well as weakening to the Somali current that in turn affect the cloud distribution and moisture entrainment towards inland regions of South Asia and MENA. The analysis of trends and regression coefficients is necessary to better understand the climate variability of MENA. Both the observational and simulated results highlight the need to better understand the long-term trend in data and to better account for the circulation responses, such as that of the NAO, ENSO and Indian summer monsoon to better understand the MENA regional climate variability.

## **Chapter 4. Sensitivity of the Regional Climate in the Middle East and North Africa to Volcanic Perturbations**

In this chapter, I investigate the sensitivity of the Middle East and North African region to strong tropical explosive volcanic eruptions. For this purpose, I selected the El Chichón (1982, Mexico) and Pinatubo (1991, Philippine) tropical eruptions, as both these eruptions erupted in the satellite era and therefore better observational records are available which provides us the opportunity to better assess the performance of the high-resolution atmospheric model, HiRAM. Hereafter, the abstract of this chapter is presented.

The Middle East and North Africa (MENA) regional climate appears to be sensitive to volcanic eruptions. Winter cooling after the 1991 Pinatubo eruption far exceeded the mean hemispheric temperature anomaly, even causing snowfall in Israel. To better understand MENA climate variability, the climate responses to the El Chichón and Pinatubo volcanic eruptions are analyzed using observations, NOAA/NCEP Climate Forecast System Reanalysis, and output from the Geophysical Fluid Dynamics Laboratory's High-Resolution Atmospheric Model (HiRAM). A multiple regression analysis both for the observations and the model output is performed on seasonal summer and winter composites to separate the contributions from climate trends, El Niño Southern Oscillation (ENSO), North Atlantic Oscillation (NAO), Indian summer monsoon and volcanic aerosols. Strong regional temperature and precipitation responses over the MENA region are found in both winter and summer. The model and the observations both show that a positive NAO amplifies the MENA volcanic winter cooling. In boreal summer, the patterns of changing temperature and precipitation suggest a weakening and southward shift of the Intertropical Convergence Zone, caused by volcanic surface cooling and weakening of the Indian and West African monsoons. The model captures the main features of the climate response; however, it underestimates the total cooling, especially in winter, and exhibits a different spatial pattern of the NAO climate response in MENA compared to the observations. The conducted analysis sheds light on the internal mechanisms of MENA climate variability and helps to selectively diagnose the model deficiencies.

### **4.1. Problem Formulation and Motivations**

Large explosive volcanic eruptions can inject millions of tons of sulfur-containing gases into the lower stratosphere. These gases oxidize into sulfuric acid, forming a sulfate aerosol plume that reflects the incoming solar radiation and cools the planet for a subsequent two to three years period (Franklin, 1784; Mitchel, 1961; Lamb, 1970; Robock, 2000; Stenchikov et al., 2009; Timmreck, 2012), affecting weather and climate. Radiative impacts of volcanic origin are

important driving factors of natural climate variability (Schneider et al., 2009; Timmreck, 2012; Fyfe et al., 2013; Santer et al., 2014). A comprehensive discussion of the role of volcanic eruptions in modulating climate can be found in earlier studies (Turco et al., 1982; Briffa et al., 1998; Hansen et al., 1992; Kelly et al., 1996; Robock, 2000; Sigurdsson, 1982; Shindell et al., 2001; Stenchikov 2009; Stenchikov et al., 2009; Timmreck, 2012; Laakso et al., 2016; Kremser et al., 2016). Volcanic eruptions drastically affect both global and regional climate (Timmreck, 2012; Schneider et al., 2009; Liu et al., 2016). However, regional climate responses are poorly simulated in comparison with global ones, as volcanic forcing is naturally of global scale (so global climate models with a relatively coarse grid spacing must be used), and resolving regional patterns requires a finer spatial resolution than conventional global models can afford.

Correct replication of climate responses to volcanic forcing is a fundamental challenge and an ultimate test for climate models attempting to simulate climate variations (Stenchikov et al., 2006; Driscoll et al., 2012). Strong volcanic eruption events provide an opportunity to test climate response because they produce measurable impacts that are used for model validation (Robock, 2000). However, volcanic climate impacts are short-lived, causing signals with relatively low signal-to-noise ratio, so composites or superposed epoch analysis is often used (Kirchner et al., 1999; Stenchikov et al., 2006; Driscoll et al., 2012).

It is well known that strong equatorial explosive volcanic eruptions are followed by a pronounced positive phase of the Arctic Oscillation (AO) for one to two Northern Hemisphere winters (e.g., Robock and Mao, 1992, 1995; Robock, 2001; Robock et al., 2002; Graf et al., 1994; Shindell et al., 2001; Stenchikov et al., 2002, 2006). The AO is defined as the first hemispheric, empirical orthogonal function of the sea level pressure variability (Thompson and Wallace, 1998, 2000) and is closely related to North Atlantic Oscillation (NAO) (Hurrell, 1995; Hurrell et al., 2003; Thompson and Wallace, 1998; Rind et al., 2005; Penner and Binyamin, 2013). In the context of this study, the terms NAO and AO are interchangeable, but since I use the NAO indices of Hurrell (1995) for my analysis, here I choose to refer to this phenomenon as NAO only. The positive phase of NAO forcing is partly induced by an enhanced equator-to-pole temperature gradient in the lower stratosphere caused by radiative heating in the aerosol cloud over the tropics (Graf et al., 1993; Kodera, 1994; Kirchner et al., 1999; Stenchikov et al. 2002; 2006; Rind et al., 2005). Stenchikov et al. (2002) have proposed that ozone depletion and the tropospheric cooling effect of volcanic aerosols also contribute towards the positive phase of NAO. Tropospheric cooling caused by aerosols in the subtropics decreases the meridional temperature gradient in the winter troposphere between 30°N and 60°N. The corresponding reduction of the mean zonal kinetic energy and the amplitudes of planetary waves in the troposphere decrease

wave activity flux in the lower stratosphere. The resulting strengthening of the polar vortex forces a positive phase of the NAO (Stenchikov et al., 2002; Rind et al., 2005). This post-eruption positive NAO phase brings anomalously warm temperature conditions to parts of America, Europe and Siberia (Groisman, 1992; Robock and Mao, 1992; Kirchner et al., 1999; Shindell et al., 2004). This post-eruption Eurasian winter warming effect has received a lot of attention and was the focus of multiple studies (Robock, 2002; Stenchikov et al., 1998, 2002, 2006; Shindel et al., 2001; Fischer et al., 2007).

The Middle East climate is also strongly affected by explosive volcanic impacts. After the Pinatubo eruption of 1991, there was an unusually cold winter that led to freezing temperatures throughout the Middle East, including snowfall in Israel, during the winter of 1991-92. The post-Pinatubo winter cooling in the northern Red Sea resulted in increased deep water mixing, which provided more nutrients to algal bloom growth and caused extensive coral reef death (Genin et al., 1995; Robock, 2002). Yu and Zhou (2004) have shown that the winter NAO forcing has a strong negative correlation with the MENA surface air temperature in winter. A few modeling studies have mentioned the cooling anomaly over the Middle East region after large volcanic eruptions (Robock and Mao, 1992; Robock, 2002; Shindell et al., 2004), indicating that it is part of a circulation response with the same origin as the winter warming in Siberia. However, there are only a few studies that analyzed the possible physical causes of the seasonal climate variability induced by strong volcanic eruptions in the Middle East and North Africa region (e.g., Joseph and Zeng, 2011; Haywood et al., 2013), so the dynamic feedbacks and forced circulation changes remain poorly understood.

Along with dynamic responses, large volcanic eruption events cause significant perturbations to the hydrologic cycle (Trenberth and Dai, 2007; Bala et al., 2008; Wild et al., 2008). Robock and Liu (1994) used the Goddard Institute for Space Studies (GISS) global climate model to analyze the precipitation response to major volcanic eruptions and noted decreases in precipitation over the Sahel belt for about two years following tropical volcanic eruptions. Oman et al. (2006) noticed a precipitation decrease and reduction in water discharge from the Nile River following the Laki eruption. Trenberth and Dai (2007) have used the Palmer Drought Severity Index (PDSI) to show a decrease in precipitation after the Pinatubo eruption. They linked this drying to the weakening of the land-sea temperature contrast caused by the volcanic radiative cooling that suppresses summer monsoon circulation, including the African, Indian and Asian monsoon systems, which is consistent with the results shown in other studies (Graf, 1992; Oman et al., 2005; Oman et al., 2006; Peng et al., 2010; Joseph and Zeng, 2011).

The tropical rain belt region and the Inter-Tropical Convergence Zone (ITCZ) also strongly respond to volcanic forcing (McCracken and Luther, 1984; Mass and Portman, 1989; Robock and Liu, 1994; Joseph and Zeng, 2011; Haywood et al., 2013; Wegmann et al., 2014; Liu et al., 2016). Eruptions in the Northern Hemisphere are found to have different effects on ITCZ than the eruptions in the Southern Hemisphere (Haywood et al., 2013; Liu et al., 2016; Pausata et al., 2015a, 2015b; 2016). Using a single eruption event, i.e. El Chichón, Haywood et al. (2013) have shown that large northern and southern hemisphere eruptions modulate the position of the ITCZ such that they cause drying or greening of the Sahel region. The ITCZ responses are closely related to the volcanic impact on the regional Hadley circulation (Tandon et al., 2013), which governs processes in the entire tropical belt.

Volcanic climate responses are not easily reproducible in climate models. Analysis of the IPCC AR4 (Stenchikov et al., 2006) and AR5 (Driscoll et al., 2012) simulations indicates that the best up-to-date global climate models cannot calculate the whole scale of regional winter warming or circulation responses to volcanic forcing in high northern latitudes. The winter regional responses in the MENA region, caused to a great extent by similar circulation processes, have not been thoroughly analyzed yet, and only a few studies are available that have been devoted to the summer regional responses. Therefore, here I try to fill this gap. I focus on regional scale atmospheric responses that are modulated by the large-scale teleconnections with ENSO, NAO or the Indian summer monsoon (ISM). To resolve regional scale and to better account for the teleconnections, I use a global atmospheric model, HiRAM, with a horizontal spatial resolution of 25 km, comparable to the resolution of regional climate models. The initial conditions in form of monthly sea surface temperature (SST) are prescribed from observations. I use state-of-the-art near-surface observations (UDEL, V2.01) and reanalysis (Saha et al., 2010) to assess the model capabilities and to study regional physical mechanisms that affect the MENA climate. For this analysis I choose the two strongest low-latitude tropical eruptions of the late 20th century, El Chichón of 1982 and Pinatubo of 1991, which have better observational records, having occurred in the satellite era (Baran and Foot, 1994; Barnes and Hoffman, 1997; Minnis et al., 1993; Read et al., 1993; Ginoux et al., 2006). In this chapter, I address the following questions:

1. How sensitive is the regional climate of MENA to volcano-induced radiative perturbations?
2. How do the effects of ENSO, NAO, and ISM modulate the MENA climate responses to eruptions?

3. How well HiRAM, a high-resolution atmospheric model, can reproduce post-eruption direct radiative and circulation changes over the MENA region?

The rest of the chapter is organized as follows. The climate model, in conjunction with the data and methodology used in this study, has been discussed in Chapter 2 (see Sections 2.2 and 2.4 for the details of the HiRAM model and observational or reanalysis data used here). Following Sections 4.2 and 4.3 highlight the experimental setup and methods used in this study. In Section 4.4, I present results and discussion, including a detailed overview of post-eruption radiative impacts, post-eruption surface temperature and precipitation responses, obtained from both weather observations and HiRAM simulations. The sensitivity of the MENA region to circulation changes, such as ENSO, NAO, and ISM, is also discussed in this section. In the last section, I summarize my results.

#### **4.2. HiRAM Experimental Setup for Volcanic Impact Study**

I conducted HiRAM simulations at C360 resolution (about 25 km), typically a range that most regional climate models use in climate downscaling studies. This allows us to study regional climate changes using a global climate model that fully accounts for regional and global scale interactions, which are especially important in the tropics. A brief description of the methodology and the experimental setup is as follows.

The model is forced with the observed monthly SST from the Hadley Centre Sea Ice and Sea Surface Temperature (HadISST1) data set (Rayner et al., 2003). The sea-ice model assumes that each grid point is either ice-free or fully ice-covered, and also assumes a uniform ice thickness of 2 meters. The anthropogenic greenhouse gases (GHGs), ozone, natural forcings, tropospheric aerosol concentration in the atmosphere and land use changes employed in the model follow the AMIP simulation setup, which is described in detail at CMIP website (<http://cmip-pcmdi.llnl.gov/cmip5/forcing.html>). The volcanic stratospheric aerosol spatial-time distribution and optical characteristics for both eruptions used in HiRAM simulations are calculated following Stenchikov et al. (2006) using aerosol optical depth from Sato et al. (1993). This volcanic aerosol dataset provides zonally averaged, monthly mean spectral-dependent single-scattering albedo, aerosol extinction, and asymmetry parameters, which are required to conduct radiative transfer simulations in the model. The indirect effect of aerosols through microphysical interaction with clouds (aerosol-cloud interaction) and associated changes in cloud properties is not considered. Three different realizations were produced, each for a 33-year (1976-2008) simulation period, and each beginning with different atmospheric initial conditions, taken from the GFDL long Atmospheric Model Intercomparison Project (AMIP) run at January 1 of

years 1976, 1977, and 1978. In all three realizations, the first three years of the integration (1976-1978) are not used in the analysis, to avoid spin-up effects. To reduce the effect of internal variability in the model results, ensemble average over three HiRAM realizations is used in the analysis.

Using an atmospheric model with a prescribed SST forcing is, of course, an idealized approach, but a fairly reasonable one, as demonstrated in earlier studies (Stenchikov et al., 2002; 2004). The ocean-related effect in my simulations is not interactive. The observed SSTs, used in my calculations, account for the ocean post-eruption cooling. Thus, in the model simulations, the atmospheric response is fully interactive and constrained by observed ocean boundary conditions. This approach allows me to evaluate the contributions of different processes more reliably and compare my results with observations.

### **4.3. Methods**

I have analyzed climate responses following the El Chichón eruption of April 1982 and the Pinatubo eruption of June 1991 for two seasons, winter (DJF) and summer (JJA). In order to reduce the possible effect of noise from internal climate variability and to make the volcanic signal clearer, a composite analysis (also known as a Superposed Epoch Analysis) is applied, which is widely used to study the effect of volcanoes on climate (Stenchikov et al., 2006; Fischer et al., 2007; Schneider et al., 2009; Peng et al., 2010). Thus, each composite is comprised of four winters (1991-92, 1992-93, 1982-83 and 1983-84) or four summers (1991, 1992, 1982 and 1983) accounting two consecutive years after each eruption. The anomalies are calculated with respect to the seasonal summer or winter climatology, calculated for the 30-year period 1979-2008, but excluding the two winter or two summer seasons immediately following each of the volcanic eruptions.

To assess the statistical significance of the volcanic signals I employed bootstrapping with replacement method (e.g., Efron and Tibshirani, 1994; Xu, 2006). The test statistic is the difference of the mean of the anomalies of a field (total or partial) corresponding to the four volcanic years and that of anomalies of the randomly sampled 4 non-volcanic years. The null hypothesis ( $H_0$ ) states that the difference between a four-year volcanic composited anomaly with the mean of 4 anomalies of randomly chosen non-volcanic years is either negligible or has an opposite sign than the volcanic anomaly. The proportion of the bootstrapped samples of the test statistic that comply with  $H_0$  is the p-value. The grid points with the p-value equal to 0.05 or less are hatched to show statistical significance at 5% (i.e., 95% confidence level, one-sided test). The identical procedure is applied to the observed and simulated fields.

Please note that in chapter 3, I employed student t-test to evaluate statistical significance of regression coefficients while for the statistical significance of the anomaly fields that are discussed in chapter 4, I employed bootstrapping with replacement method. I noticed that both methods produce more or less similar results, however, bootstrapping with replacement gives more significant hatching area at 95 % confidence level compared to student t-test presumably because bootstrapping with replacement could work better especially for small data samples.

To separate the contributions of multiple factors, I apply multiple linear regression technique to the anomaly fields (see Section 3.3, Section 4.4.4 and Section 4.4.6 for details). The multiple linear regression analysis has been widely used to separate out volcanic signals (see, e.g., Randel, 2010; Fujiwara et al., 2015; Gu & Adler, 2010; Gu & Adler, 2011). The ideal/best approach to identify the direct volcanic and posteruption circulation (e.g., ENSO, NAO and Indian monsoon) response is by conducting climate model sensitivity experiments with and without volcanic aerosol forcing (e.g., Predybaylo et al., 2017). This study is to a great extent based on the comparison of my model simulations with observations that do not have nonvolcano realizations. That is why I conducted the model analysis similar to my analysis of observations and did not include the nonvolcanic or non-ENSO control simulations. In this study, I conduct multiple regressions using simulated and observed anomalies for 30 years period (1979-2008) to compare the model and observed responses. To prove that the 30-year period is sufficient, I also conduct multiple regressions using a 109-year observation period (see Section 4.4.6 for details). In all cases, I include climate trend in the multiple regression (linear for the 30-year interval and polynomial for the 109-year interval) and ENSO. To account for possible nonlinear trend over longer period (1900 -2008), I used polynomial regression, which is a special case of multiple linear regression. For polynomial regression, I included the cubic polynomial trend term in the multiple regression analysis (see Section 3.3, equations 5-8). The effect of volcanic aerosols (i.e., direct volcanic effect) is considered as a residual, similar to previous studies (Randel, 2010; Fujiwara et al., 2015), to avoid losing accuracy in calculations due to close correlations between the ENSO and volcanic impacts, as both the El Chichón and Pinatubo eruptions occurred in El Niño years. However, the residual term might contain some contributions from the internal variability and the factors that are not included in the multiple regressions, e.g., IOD, EA/WR and quasi-biennial oscillation (QBO)-induced temperature variability (see Appendix A).

#### **4.4. Results and Discussion**

##### **4.4.1. Radiative Impact**

Aerosol plumes developing in the lower stratosphere after explosive volcanic explosions

modulate the climate of the earth by scattering (ultraviolet, visible and near-infrared) and absorbing (near-infrared) the incoming solar short-wave (SW) radiation. The presence of these scattering aerosols in the stratosphere reduces the amount of net solar radiation reaching the Earth's surface. The aerosol layer also both absorbs and emits long-wave (LW) radiation, which causes warming in the equatorial lower stratosphere and presumably forces the NAO to its positive phase (Stenchikov et al., 1998; 2002; 2006). Figure 4.1 shows zonal averaged aerosol optical depth (AOD) at 550 nm, calculated over the MENA (4°S-45°N) region using AOD data of Sato et al. (1993). Both eruptions show a significant increase in the aerosol loading over the MENA region, which peaks in the fall and winter seasons of 1982 and 1991, following the El Chichón and Pinatubo eruptions, respectively. The aerosol loading in the stratosphere decays to the background level within two to three years following each eruption. To identify the radiative impact of these stratospheric volcanic aerosol plumes, the ensemble mean anomalies of the all-sky shortwave net (SWNET) radiation (positive direction is down) at the surface over the MENA region are analyzed, and the model results are compared with the CFSR product (Figure 4.2). As discussed in the previous section, these fields are composited for two post-eruption seasons and for both eruptions. The CFSR and HiRAM show that the volcanic aerosols generally reduce the SWNET flux in both seasons. These changes are statistically significant at a 95% confidence level and fall within the previously reported range of the SWNET flux anomaly produced by the El Chichón and Pinatubo volcanic plumes over the tropics and sub-tropics (Mennis et al., 1993; Stenchikov et al., 1998; Trenberth and Dai, 2007; Man et al., 2014). The post-eruption summer and winter spatial distributions of the SWNET flux are consistent between CFSR and HiRAM. The magnitude of the negative SWNET flux anomaly in winter peaks at  $-10 \text{ W/m}^2$  in CFSR and  $-6 \text{ W/m}^2$  in HiRAM. Both the CFSR and HiRAM SWNET fluxes exhibit some spatial differences that could be accounted for by possible variations in the spatial distribution of cloud contents, water vapor, land surface characteristics or associated feedback processes (Hansen et al., 1981; Stenchikov et al., 1998; Soden et al., 2002; Schmidt et al., 2012).

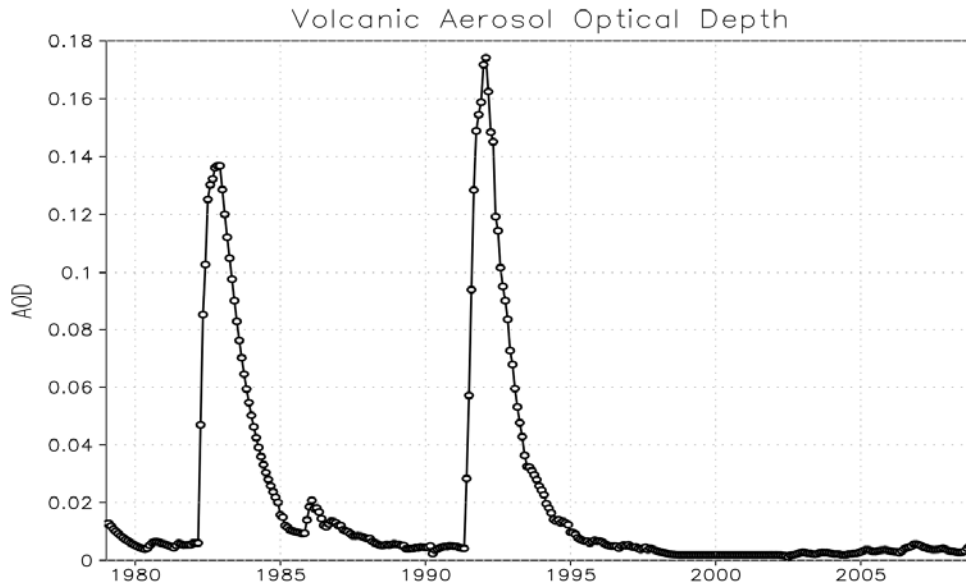


**Figure 4.1:** Total stratospheric aerosol optical depth at 550 nm as a function of time, zonally averaged over the MENA latitudes (5°S-45°N, data source: Sato et al., 1993).

Positive anomalies of the SWNET flux in the tropical regions of the summer hemisphere are observed in both seasons (Figure 4.2) due to cloud reduction caused by post-eruption radiative cooling. Both HiRAM and CFSR clearly exhibit this feature. The magnitude of the SW heating in the summer season peaks at  $10 \text{ W/m}^2$ , both in HiRAM and CFSR, over the northern border of the ITCZ region that in the scope of this study I associate with the area of the upward motions in the regional Hadley Cell. This suggests that the volcanic impact suppresses deep tropical convection predominantly in the summer hemisphere and weakens the rising branch of the Hadley Cell over the Sahel, causing a southward shift of the ITCZ (Haywood et al., 2013; Joseph and Zeng, 2011). I further discuss the complex nature of the ITCZ response in Sections 4.4.4 and 4.4.6.

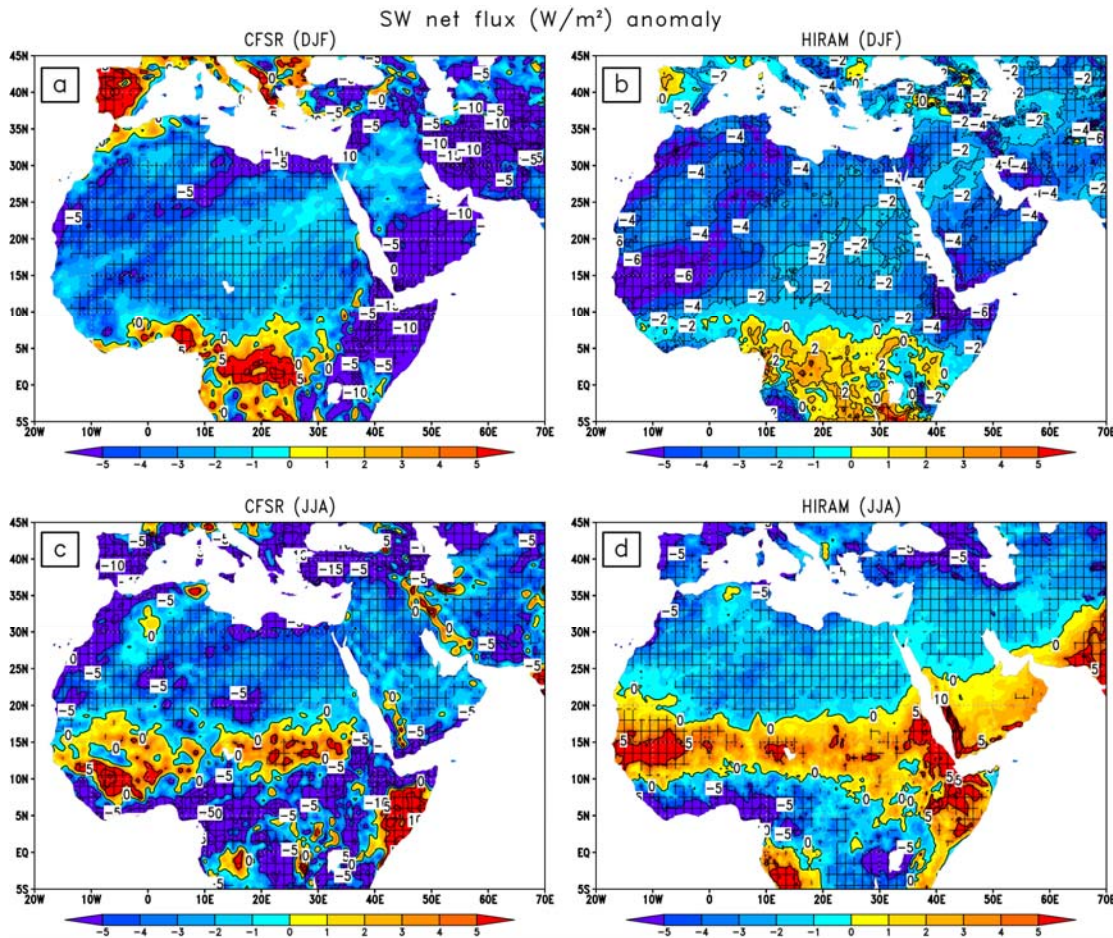


**Figure 4.2:** Seasonal (DJF and JJA) two-year anomalies of solar net flux ( $\text{W/m}^2$ ) composites following the El Chichón and Pinatubo explosive eruptions, calculated for winter using a) CFSR and b) HiRAM outputs, and for summer using c) CFSR and d) HiRAM outputs. Hatching shows the statistically significant areas with at least 95% confidence level examined by bootstrapping with replacement test.

Analysis of the clear-sky shortwave net flux, both at the top of the atmosphere and at the surface, shows a significant decrease during both seasons over the entire MENA domain (not shown). The clear-sky SW net flux anomaly exhibits more uniform spatial distribution than the all-sky. The warming pattern seen under all-sky conditions is not present in the clear-sky case, which confirms that a reduction in clouds is responsible for the positive SWNET anomaly in the ITCZ region.

#### 4.4.2. Total Temperature and Precipitation Response

To quantify the regional responses of MENA to volcanic impacts and natural variability, I first examine the total composited anomalies of surface air temperature and precipitation fields for

both the model output and the UDEL observations (Figure 4.3 and 4.4), and in subsequent Sections 4.4.4, 4.4.5 and 4.4.6 I further study the partial responses associated with different climate factors.

This analysis presumably reveals that the volcanic impact and natural variability could produce substantial cooling (predominantly in north Africa and the northern part of Arabian Peninsula) and drying over the MENA region (predominantly in central and southern areas) in post-eruption years as shown in Figure 4.3 and 4.4, respectively. This agrees well with previous studies (e.g., Genin et al., 1995; Robock and Mao, 1995; Robock, 2000; Shindell et al., 2004; Man et al., 2014).

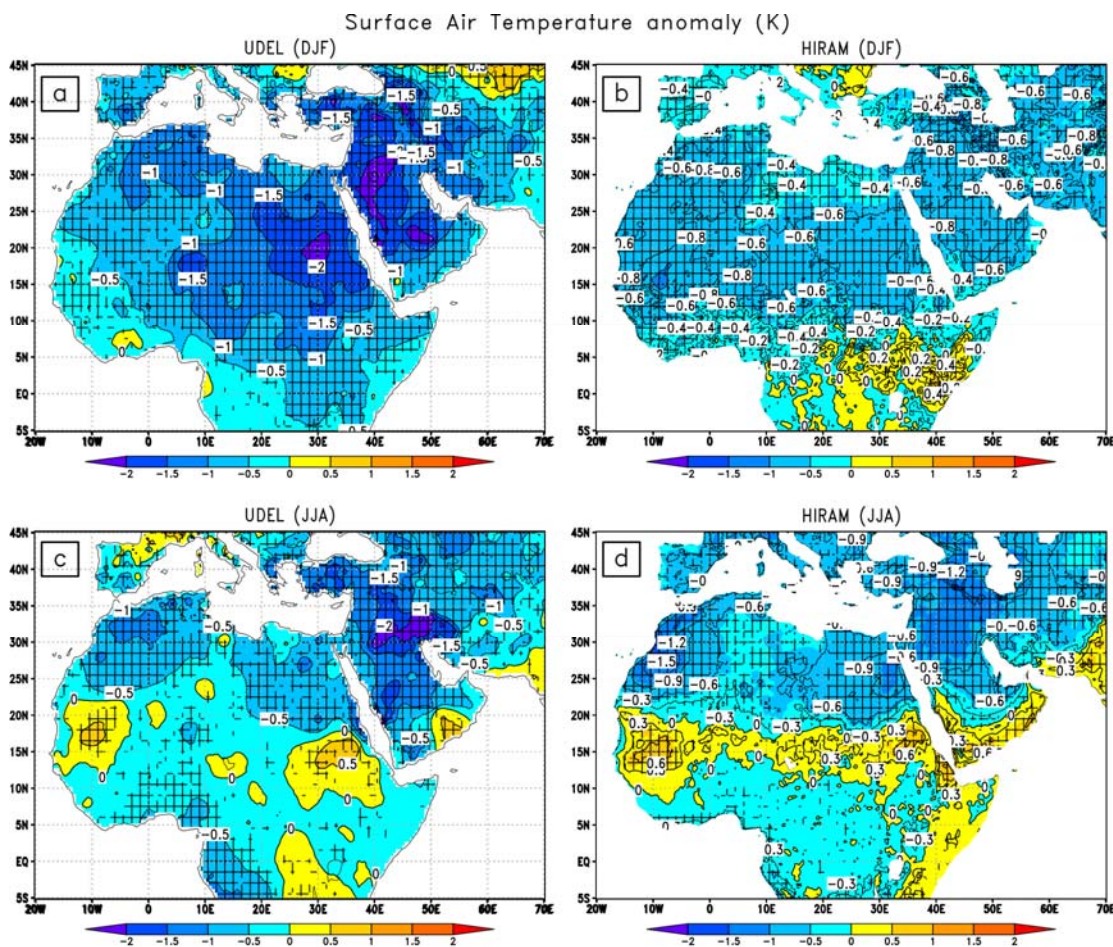


**Figure 4.3:** Seasonal (DJF and JJA) two-year anomalies of surface air temperature (K) composites following the El Chichón and Pinatubo explosive eruptions, calculated for winter using a) UDEL observations, b) HiRAM output, and for summer using c) UDEL observations, d) HiRAM output. Hatching shows the statistically significant areas with at least 95% confidence level examined by bootstrapping with replacement test.

The winter cooling in the UDEL observations over the MENA region (Figure 4.3a) is

especially strong, ranging between -0.5 K and -2.0 K, and is almost 3 times the globally averaged Pinatubo temperature anomaly (Stenchikov et al., 2009; Santer et al., 2001, indicating the large sensitivity of the MENA winter climate to external radiative forcing. The model temperature responses are smoother and the cooling signal is more uniformly distributed (Figure 4.3b) compared to the observations, as they are averaged over three realizations. The overall structure and geographic patterns are largely consistent between the model and observations. The cooling response in Figures 4.3a and 4.3b is stronger over central and East Africa and the Arabian Peninsula, including the central and northern parts of the Red Sea, and is more pronounced in the observations than in the model simulations.

The simulated temperature anomaly in the summer season is in better agreement with the observations than the winter counterpart. Figures 4.3c and 4.3d show a strong, but weaker than in winter, cooling signal that peaks at -1.5 K (in observations) over the northern part of the Arabian region, and at -0.5 K over the rest of the MENA domain; except for the summer tropical belt, where the positive surface air temperature anomaly peaks at 0.6 K. This warming is consistent with the increasing all-sky SWNET flux over the tropical region (the Sahara and Sahel belt) in summer (see Figures 4.2c and 4.2d).

A precipitation decrease ranging from -0.5 to -1.0 mm/day, both in the observations and in the HiRAM simulations, is seen in the winter season (Figures 4.4a and 4.4b), mainly over the tropical region. The precipitation anomaly pattern produced by the HiRAM simulation is in agreement with the observations and previously reported results (Trenberth and Dai, 2007; Fischer et al., 2007; Joseph and Zeng, 2011). Trenberth and Dai (2007) also reported drying over the MENA region, particularly in the tropical region; however, they considered the annual mean responses following Pinatubo eruption, whereas I focus on the seasonal responses composited over two years following the El Chichón and Pinatubo eruptions. The surface cooling and associated decreased evaporation from the ocean in post-eruption years, causing dryness and reducing moisture transport over the MENA land areas, partially explain this effect. The pressure anomalies in the Atlantic Ocean during boreal winter, associated with the positive NAO phase, may add to this dryness by drawing cold and dry northwesterly winds from polar areas towards the MENA domain.

In the summer season (Figures 4.4c and 4.4d), I observe a negative precipitation anomaly over almost the entire domain except in Southern Europe extending to Turkey, Syria, and Iraq. A weak meridional dipole structure in the tropical region, with drying over the Sahel (up to -1.5 mm/day) and a positive precipitation anomaly to the south (ranging from 0.5 to 1.0 mm/day), from 10°N to the equator, is seen both in the observations and the model (Figures 4.4c and 4.4d).

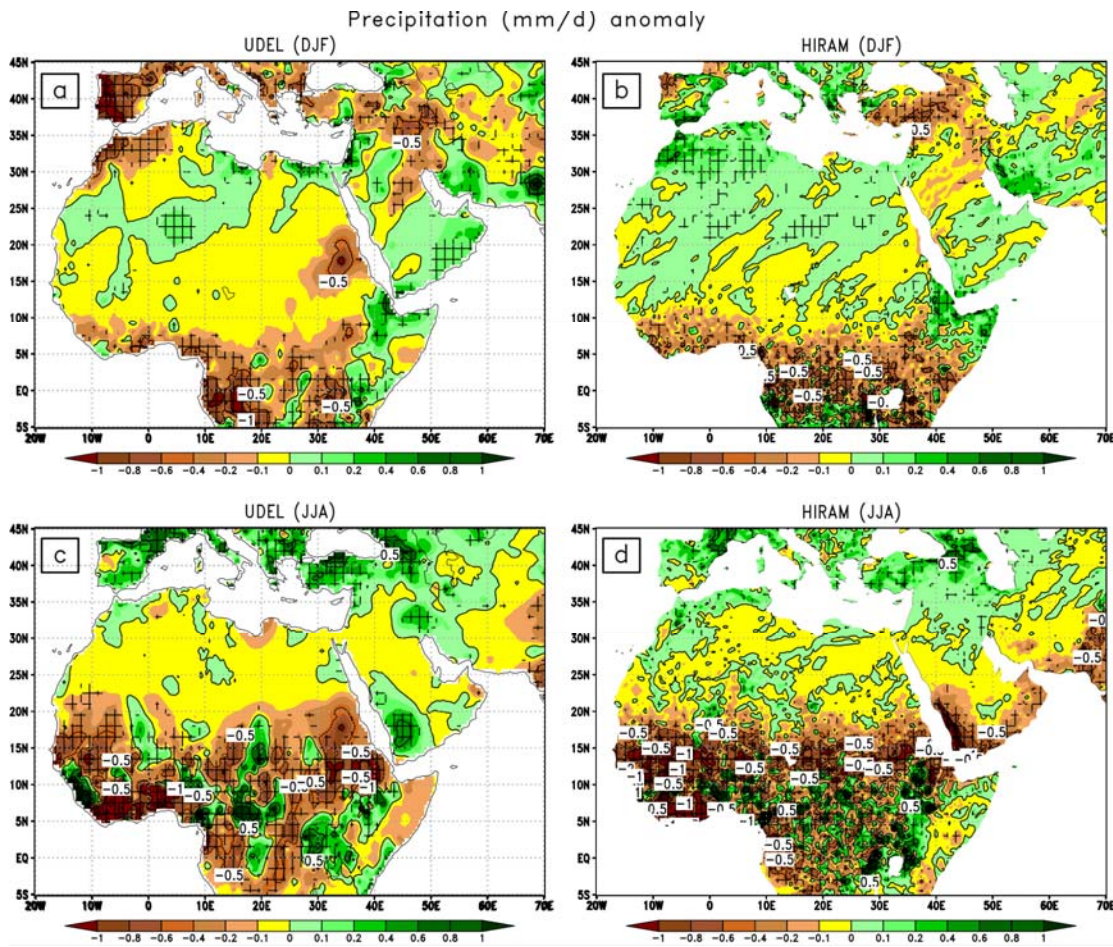


**Figure 4.4:** Same as Figure 4.3, but for precipitation anomaly (mm/day).

These results are consistent with a previous study conducted by Joseph and Zeng (2011), where the post-eruption summer anomalies were composited for the Agung, El Chichón and Pinatubo eruptions. The positive summer precipitation anomalies (simulated and observed) in southern and southeastern Europe are consistent with the results of the study conducted by Fischer et al. (2007), which showed a similar pattern during the first summer following large explosive volcanic eruptions. The precipitation anomalies in this analysis are statistically significant at a 95% confidence level in most parts of the MENA domain.

It is well known that explosive volcanic eruptions can affect both the Hadley circulation and precipitation in the ITCZ (Haywood et al., 2013; Pausata et al., 2015a, 2015b; 2016; Oman et al., 2006). The African ITCZ is especially vulnerable as it experiences large seasonal migrations. The radiation, temperature, and precipitation anomalies in the post-eruption years (Figures 4.2c, 4.2d, 5.3c, 5.3d, 5.4c and 5.4d) are generally consistent with a weakening and southward shift of the ITCZ. To test this concept, I analyze the vertical mass flux  $M_{\phi}$  in a regional Hadley

circulation, separated from the Walker mass flux following (Schwendike et al., 2014; Bangalath and Stenchikov, 2015). Figures 4.5a and 4.5b show the total regional JJA mass flux  $M_\phi$  at 500 hPa, averaged over the 1979-2008 period as a function of latitude  $\Phi$  and longitude  $\lambda$ , both for the CFSR reanalysis (CFSR) and the HiRAM simulations. The CFSR  $M_\phi$  is spatially a little more compact with a more pronounced core than in the model, but the resemblance to HiRAM is quite good. The model captures correctly even small areas of upward motion over the eastern Mediterranean Sea and the northwestern coast of Africa in summer season that presumably are forced by the orography (Simpson et al., 2015). Figures 4.5c and 4.5d show the composite anomaly of  $M_\phi$  in the eruption years.

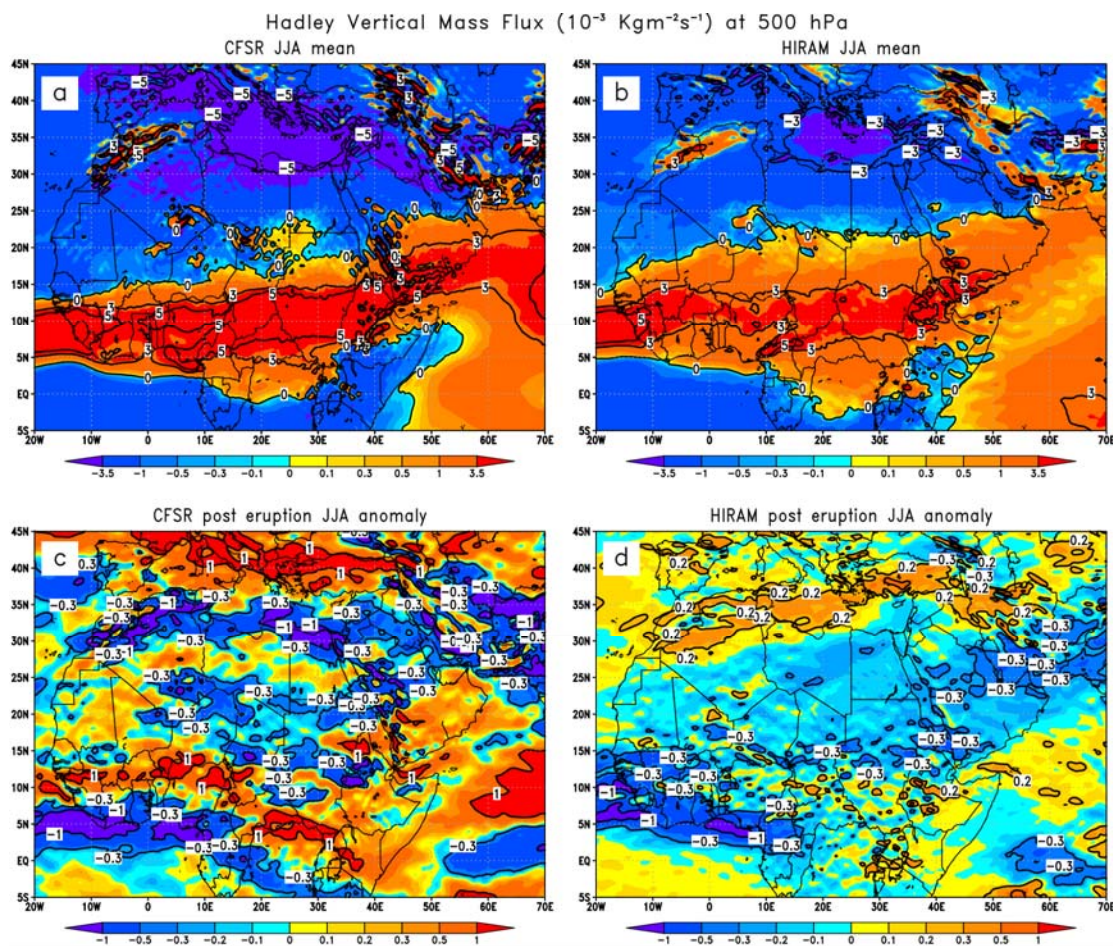


**Figure 4.5:** Summer (JJA) total vertical regional Hadley Cell mass flux  $M_\phi$  (positive upward,  $10^{-3} \text{ kg m}^{-2} \text{ s}^{-1}$ ) averaged over the period 1979-2008 (excluding post-eruption years) using a) CFSR, b) HiRAM outputs, and two-year composited anomalies of  $M_\phi$  ( $10^{-3} \text{ kg m}^{-2} \text{ s}^{-1}$ ) following the El Chichón and Pinatubo eruptions calculated using c) CFSR, d) HiRAM outputs.

The  $M_\Phi$  anomalies, although weaker in the model, are fairly consistent with the reanalysis, showing the weakening of the large-scale subsidence over the Mediterranean, and the strengthening of the upward motion at  $0 < \Phi < 10^\circ\text{N}$ , especially in central and East Africa. In West Africa, the weakening of  $M_\Phi$  in the West African monsoon dominates. Thus, despite the weakening and southward shift of cloudiness and ITCZ seen across the entire continent, the driving mechanisms of this effect on West and East Africa could be quite different. The Indian and African monsoon systems are tightly linked to the rising branch of local Hadley Cell (Joseph and Zeng, 2011; Wegman et al., 2014), and the post-eruption anomalies of  $M_\Phi$  over the MENA tropics could be modulated by changes in the Indian and African monsoon systems (Wegman et al., 2014).

Presumably, the meridional dipole pattern in the summer precipitation response seen in Figures 4.4c and 4.4d in the tropics, which forms because the West African monsoon (WAM) circulation is suppressed and the ITCZ shifts southward, is induced by both direct volcanic radiative cooling and circulation changes. The suppression of the regional WAM system is caused by a change in the thermal contrast between the Gulf of Guinea and African landmasses as well as between the Arabian Sea and the nearby continental Arabian Peninsula (Haywood et al., 2013). Oman et al. (2005, 2006) have also reported a decrease in cloud amount after the Katmai eruption of 1912, as a result of a post-eruption weakening of the Indian and African summer monsoon systems and an associated reduction in precipitation and Nile water discharge.

Summarizing the total regional climate response in MENA, I conclude that the model and observations show that cooling is more pronounced in boreal winter (in observations the winter temperature change is up to 1 K colder than in summer) than in the boreal summer (Figure 4.3), although the radiative forcing is not very different (Figure 4.2). This suggests the contribution of an additional “dynamically forced” cooling, caused by circulation changes associated with the positive phase of the NAO. Summer anomalies over the MENA region are strongly affected by the weakening of the monsoon circulation, the shift in the ITCZ and the drying in the Sahel. Thus, the preliminary analysis shows that the MENA regional climate anomalies in the post-eruption years following the El Chichón and Pinatubo eruptions are modulated by multiple factors, e.g., NAO in winter and ISM in summer. Moreover, both seasons are affected by the ENSO phase, and climate trends that is important and therefore must be accurately evaluated and filtered out. To better understand the driving mechanisms and to clearly reveal the model deficiencies, in the next section I conduct a multiple linear regression analysis that, in the first approximation, allows us to delineate the contributions from different physical processes.

#### **4.4.3. Post-eruption Circulation Impacts**

The post-eruption circulation impacts on MENA climate caused by NAO, ENSO and Indian monsoon need precautions/attention while interpretation of the results that are discussed in the following sections (Section 4.4.4. and subsequent subsections) as explained below.

It has been shown in several studies that the strong volcanic eruptions provide suitable conditions that favor or strengthen the formation of the positive ENSO (Maher et al., 2015; Pausata et al., 2015; Ohba et al., 2013; Predybaylo et al., 2017; Khodri et al., 2017) and positive NAO phases (Stenchikov et al., 2002, Driscoll et al., 2012; Zambri et al., 2017; Timmreck, 2012; Fischer et al., 2007). This suggests that both the El Nino and NAO circulations that happened during the time of El Chichón and Pinatubo eruption might be produced or modulated by these volcanic eruptions. However, it doesn't necessarily mean that these circulations presumably belong to the volcanoes only. The pre-eruption conditions of these circulations could be neutral or they might be in the positive/negative state. Moreover, they could be produced without the eruption, as is the case during non-eruption periods. Although the more likely scenario is that during the eruption time these circulation modes are probably forced towards their positive phases as is explained in earlier studies (Maher et al., 2015; Pausata et al., 2015; Ohba et al., 2013; Emile-Geay et al., 2008; Predybaylo et al., 2017; Khodri et al., 2017; Stenchikov et al., 2002, Driscoll et al., 2012; Zambri et al., 2017; Timmreck, 2012; Fischer et al., 2007), the term "indirect impact" used in the thesis needs to be treated simply as the impacts caused by the circulation anomalies during four post-eruption winter/summer seasons following both the El Chichón and Pinatubo periods. Largely speaking, this post-eruption indirect impact contains the contribution of both the eruptions and already existing (background state) part of these circulations along with any other possible internal natural variability.

#### **4.4.4. Delineating the Effects of NAO, ENSO, ISM and Volcanic Aerosols**

NAO, ENSO and ISM are the major external circulation modes that affect the climate of MENA (Wanner et al., 2001; Aiki et al., 2006; Camberlin et al., 2010; Josey et al., 2011; Flaounas et al., 2012; Papadopoulos et al., 2013; Abualnaja et al., 2015). West African Monsoon (WAM) is considered to be internal to MENA as it is produced within MENA region. There are a few other teleconnection modes with origins in the Atlantic sector that have been shown to induce climate changes over the Mediterranean Middle East, such as the East Atlantic (EA) and East Atlantic/West Russia (EA/WR) patterns. However, their contribution to MENA regional climate variability is much smaller than NAO, ENSO or ISM (Wanner et al., 2001; Krichak et al., 2002; Lim, 2015). I also tested the impact of the Indian Ocean Dipole (IOD) on the MENA region by

including IOD normalized index in the regression analysis and found it negligibly small. The Atlantic Multi-Decadal Oscillation (AMO) introduced in Schesinger and Ramankuttu (1994) is an important control on much longer time scales than those considered in this study; hence, they are not included.

Thus, in the winter season I perform the multiple regression analysis by employing a climate trend index (which references the calendar year of the studied season), the ENSO index (DJF sea surface temperature anomaly in the Niño 3.4 region) and the NAO index (Hurrell, 1995; Hurrell and Deser, 2010); whereas in the summer season I consider the climate trend index, the ENSO index and the Indian summer monsoon rainfall index (IMI) introduced in Parthasarathy et al. (1994) and Parthasarathy (1995), as a total summer rainfall computed over the entire Indian region. The selection of these indices for the winter or summer season is based on their relevance to this region as discussed in Josey et al. (2011), Papadopoulos et al. (2013) and Abualnaja et al. (2015), as well as on my own experience (i.e., the selected predictors have significant correlation with MENA temperature and precipitation fields in a corresponding season). All the predictors (Figure 3.2) used in the multiple regression analysis (NAO, ENSO and IMI) are standardized. The residual component of the multiple regression analysis (i.e., difference between observed and predicted values) have been interpreted as a volcanic impact (Randel, 2010; Fujiwara et al., 2015); however, they might contain contributions from the internal variability and the factors that are not included in the multiple regressions, e.g., IOD, EA/WR or QBO related variability (see appendix A and Appendix B). The multiple regression analysis used in this study is discussed in detail in Section 3.3 and Section 4.4.6. Appendix B provides a further discussion regarding the robustness of multiple regression analysis. Additionally, I perform multiple regression analysis over a longer 109-year period (1900-2008) using UDEL observations, to test the robustness and significance of the results obtained using a 30-year (1979-2008) simulation period (Section 4.4.6).

#### **4.4.5. Winter Climate Response**

##### **4.4.5.1. ENSO**

ENSO is a leading source of climate variability seen both in the ocean and the atmosphere (Trenberth et al., 1998; Trenberth and Caron, 2000; Timmermann et al., 1999). Global atmospheric teleconnections from ENSO cause extreme weather events, droughts, flooding and changes to tropical cyclone activity (Chan, 1985; Nicholls, 1985; Power et al., 1999). The ENSO impact on global and regional temperatures and precipitation patterns have been widely discussed (Trenberth et al., 1998; Timmermann et al., 1999; Ashok et al., 2004; 2007; Zhang et al., 2013; 2015).

It has been shown that an El Niño event has the potential to modulate a volcanic signal (Mass and Portman, 1989; Portman and Gutzler, 1996; Timmreck, 2012; Robock et al., 1995). The last three major volcanic eruptions, Agung (1963), El Chichón (1982) and Pinatubo (1991), coincided with El Niño events (Trenberth and Dai, 2007; Timmreck, 2012); therefore, the extraction of ENSO signals using simple linear regression was suggested by Robock and Liu (1994) while discussing volcanic impacts. Here I make use of multiple linear regression to simultaneously account for the contributions of multiple interfering factors. ENSO has a reasonably high correlation with MENA winter and summer surface temperatures, suggesting that it could play a role in modulating climate response in this region.

Figures 4.6a and 4.6b show the anomaly of ENSO-regressed temperature over the MENA region (both in the observation and the model) composited for two winter seasons after both the El Chichón and Pinatubo eruptions. The model underestimates the magnitude of ENSO-related winter cooling compared to the observations, although their overall spatial patterns are coherent. The observations show a stronger cooling anomaly over Sudan and parts of the Arabian Peninsula than in the HiRAM simulations although the 109-year observational analysis appears to be more consistent with the model (see Section 4.4.6). Both the observations and the model show similar warming signals over parts of Afghanistan, Turkmenistan, Yemen, Ethiopia, South Sudan, Liberia, Guinea, Mauritania and Western Sahara. Figures 4.6c and 4.6d show ENSO-induced precipitation anomalies over the MENA region. Drying anomalies of 0.1 to 0.2 mm/day are scattered over the entire region, and are less pronounced and less organized in specific spatial patterns than the temperature responses.

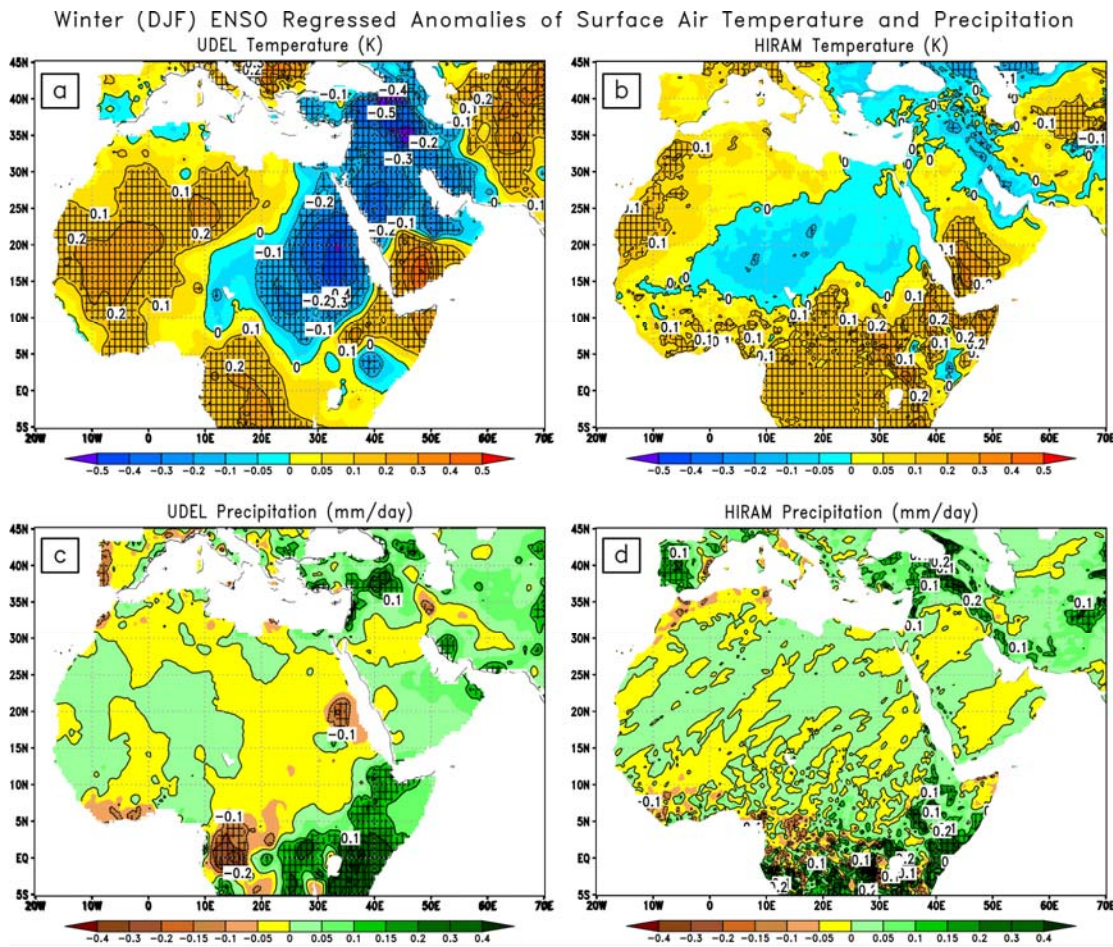


**Figure 4.6:** Anomalies of ENSO-regressed surface air temperature (K) and precipitation (mm/day) composited over two winter (DJF) seasons after both the El Chichón and Pinatubo eruptions. The temperature composites are calculated using a) UDEL observations, b) HiRAM output, and precipitation composites using c) UDEL observations, d) HiRAM output. Hatching shows the statistically significant areas with at least 95% confidence level examined by bootstrapping with replacement test.

#### 4.4.5.2. NAO

The NAO effect on southern Europe and the Mediterranean Middle East was discussed in (Wallace and Gutzler, 1981; van Loon and Rogers, 1978; Cullen et al., 2002; Iqbal et al., 2013). It was also observed that large equatorial explosive volcanic eruptions of a size comparable to El Chichón and Pinatubo strengthen and force the NAO towards its positive phase (Stenchikov et al., 2002, 2006), causing a poleward shift of the subtropical jet and the storm tracks in the Northern Hemisphere boreal winter. The associated winter warming in northern high latitude regions covering Eurasia and North America (Baldwin and Dunkerton, 1999; Kirchner et al., 1999;

Kodera et al., 1995, Graf et al., 1993; Robock, 2002; Stenchikov et al., 2002, 2006) was a subject of intensive research during the past decade. Here I focus on the NAO's effect on the MENA region in post-eruption years.

Figure 4.7 displays composited (i.e., averaged over two winters after both the El Chichón and Pinatubo eruptions) anomalies of NAO-regressed surface air temperature and precipitation that show the substantial cooling and drying over the MENA region. The magnitude of NAO-induced simulated winter cooling reaches  $-0.35$  K compared with  $-0.6$  K in the observations (Figures 4.7a and 4.7b). The HiRAM NAO winter cooling signal is twice as weak as the observations. The spatial pattern of the NAO-regressed surface temperature anomaly is also not very well reproduced by the model, which shows maximum cooling in central Africa, while in observations the maximum cooling is seen in the northwest of Africa.

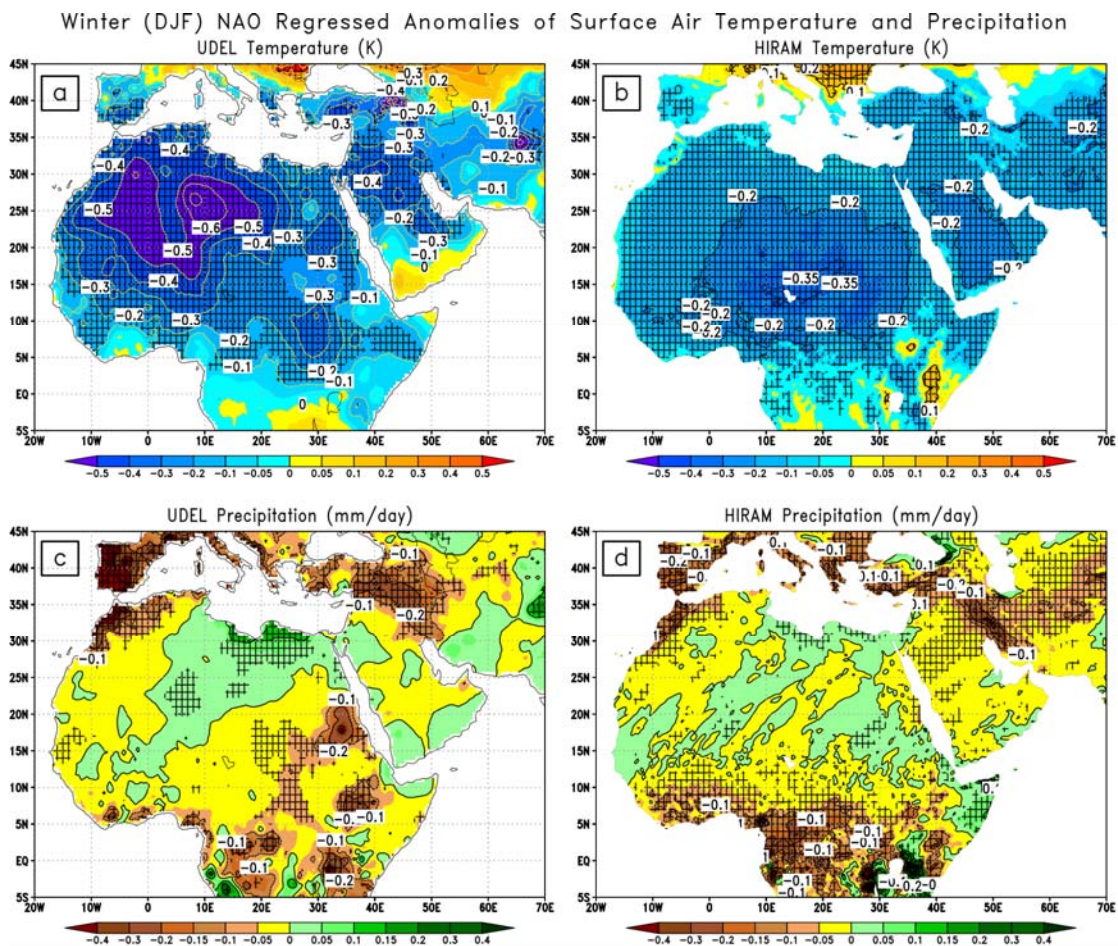
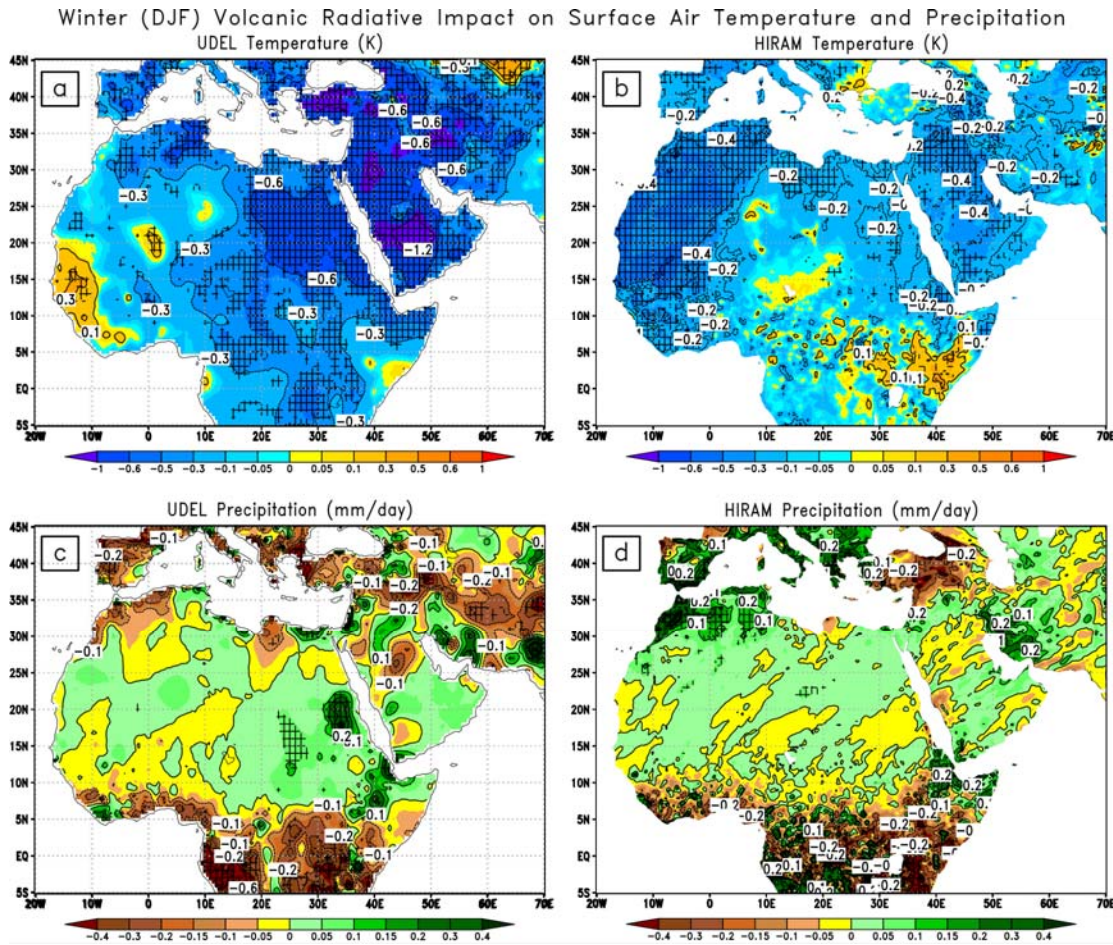


Figure 4.7: Same as in Figure 4.6 but for the case of NAO-regressed anomalies.

This discrepancy between the simulated and observed anomalies could be partly attributed to the internal variability, but because anomalies are statistically significant both in the model and in observations, I relate the discrepancy more to the model deficiency. The pattern of the NAO-induced precipitation anomaly is largely consistent between the model and observations (Figures 4.7c and 4.7d). The NAO precipitation anomaly peaks at -0.2 mm/day, both in the model and the observations. Drying is more pronounced over southeastern Europe, the northern part of the Arabian Peninsula (Syria, Jordan and Iraq) and over the tropical region, than in central Africa, where either no precipitation changes or a very weak signal is observed.

#### **4.4.5.3. Volcanic direct impacts**

Figure 4.8 shows the residual anomalies of surface air temperature and precipitation averaged over two post-eruption winter seasons following both the El Chichón and Pinatubo eruptions. This anomaly is calculated using the residual term by subtracting linear trend, ENSO and NAO-regressed fields from the total anomaly (Figures 4.3a, 4.3b, and Figures 4.4a, 4.4b), and shows volcanic direct impacts (see Section 4.3 for details). Both the model and the observations display a significant cooling signal over the entire MENA domain that is, presumably, caused by the reflection of the incoming shortwave radiation by stratospheric volcanic aerosols following the volcanic eruptions. The observed volcanic winter cooling signal is strong over the Arabian Peninsula (-1.2 K) and northeastern Africa (-0.6 K), but in the simulations, it peaks at -0.4 K in western Africa and the center of the Arabian Peninsula. The model slightly underestimates the volcanic cooling and exhibits marginally different spatial cooling patterns; however, the overall anomaly structure is consistent with the observations. The precipitation decreases in the tropics south of 10°N, both in the model and the observations, due to radiative cooling. The model does not capture drying signals on the Mediterranean coasts, or in Spain, Iran or Afghanistan. However, it does show the correct signal over Turkey.



**Figure 4.8:** Winter (DJF) anomalies of surface air temperature (K) and precipitation (mm/day) regressed on the residual term (volcanic effect) composited for two winter seasons following both the El Chichón and Pinatubo eruptions. The temperature composites are calculated using a) UDEL observations, b) HiRAM output, and precipitation composites using c) UDEL observations, d) HiRAM output. Hatching shows the statistically significant areas with at least 95% confidence level examined by bootstrapping with replacement test.

#### 4.4.6. Summer Climate Response

##### 4.4.6.1. ENSO

Typically, ENSO peaks in winter, but as its development starts a year before the peak and its decay extends to a year after, it could modulate a volcanic signal during the summer season (Zhang et al., 2013). Volcanic eruptions could also trigger El Niño-like SST anomalies. Northern Hemisphere high-latitude eruptions during the summer force an El Niño within the following 8-9 months, through a southward shift of the ITCZ (Pausata et al., 2015a; 2015b; 2016). Tropical low-latitude eruptions tend to enhance El Niño-like anomalies for the following 12 months after

an eruption (Predybaylo et al., 2017; Adams et al., 2003; Mann et al., 2005; Emile-Geay et al., 2008; Ohba et al., 2013; Maher et al., 2015).

Figures 4.9a and 4.9b show the composited MENA climate response (both in the observations and the model) associated with the winter positive ENSO phase occurring in the years of the El Chichón and Pinatubo volcanic eruptions.

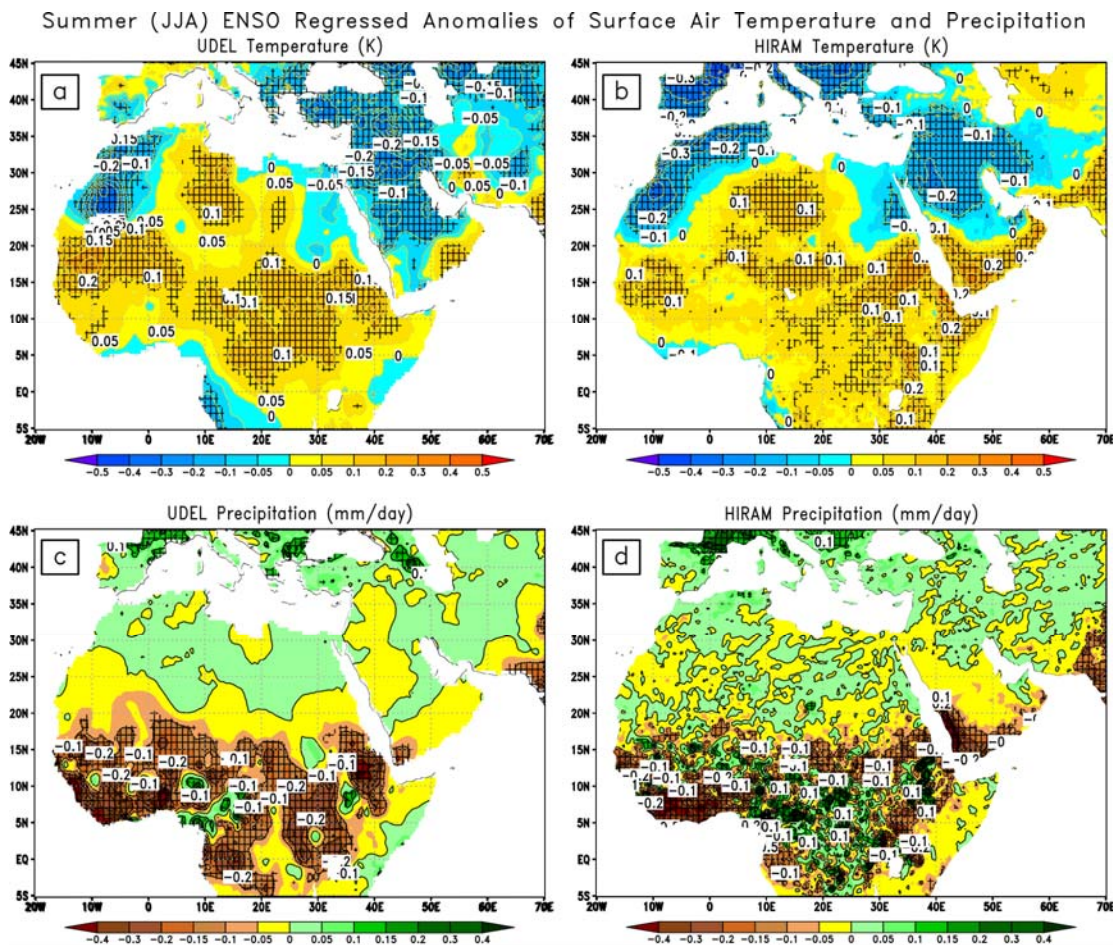


**Figure 4.9:** Anomalies of ENSO-regressed surface air temperature (K) and precipitation (mm/day) composited over two summer (JJA) seasons after both the El Chichón and Pinatubo eruptions. The temperature composites are calculated using a) UDEL observations, b) HiRAM output, and precipitation composites using c) UDEL observations, d) HiRAM output. Hatching shows the statistically significant areas with at least 95% confidence level examined by bootstrapping with replacement test.

Both the model and observations depict a spatially fairly uniform warming signal of 0.1-0.2 K, except over the northern Arabian Peninsula, southern Europe, and northwestern Africa, where a cooling signal is observed instead. The temperature response is consistent spatially and

quantitatively in the model and the observations. The drying effect (Figures 4.9c and 4.9d) is seen over the tropical regions, except some areas of North Africa and southern Europe, where increased precipitation is detected. Both the magnitude and the spatial structure of ENSO-induced precipitation anomalies in post-eruption summers are in good agreement between the observations and the HiRAM simulation. The significant drying of the northern tropics (including WAM and East Africa) suggests an overall suppression of convective activity because of the ENSO-induced change to the Hadley and Walker circulations, thereby resulting in less cross-equatorial moisture transport from the ocean towards inland areas (see, e.g., Shukla, 1975; Ashok et al., 2004; 2007; Dogar and Kucharski et al., 2017; Dogar et al., 2019).

#### **4.4.6.2. Indian Summer Monsoon**

Strong volcanic eruptions have been known to suppress the ISM (Oman et al., 2006; Trenberth and Dai, 2007; Anchukaitis et al., 2010; Joseph and Zeng, 2011; Liu et al., 2016; Robock and Liu, 1994; Robock et al., 2008), through solar dimming and weakening of the temperature contrast between the continents and the ocean. In turn, the ISM profoundly affects summer circulation over the tropical MENA region (Rodwell and Hoskins, 1996; Sultan and Janicot, 2000).

In post-eruption summers the weakening of the ISM causes warming and drying anomaly over the 15°N tropical belt (Figure 4.10). Warming reaches 0.15 K, both in the model and the observations. HiRAM shows a better organized tropical warming pattern compared to the UDEL observations because the model anomalies are built using three realizations and do not suffer from insufficient data coverage, as the observations do. The warming pattern is consolidated over the summer ITCZ region, and can be attributed to the weakening and southward shifting of the regional Hadley Cell.

Drying southward of 20°N (the Sahel region) is found both in the model and observation in Figures 4.10c and 4.10d, peaking at -0.2 mm/day. At the same time, precipitation from the WAM and in central equatorial Africa increases. The model results are fairly consistent with the UDEL observed pattern, which indicates the model's potential to simulate the Indian summer monsoon effect in the MENA region. The ISM-contributed precipitation anomaly shows a meridional dipole pattern (decreasing precipitation north of 10°N but increasing south of 10°N, in central and West Africa) that is consistent with the southward shift of the ITCZ (Haywood et al., 2013; Joseph and Zeng, 2011) and the strengthening of the coastal monsoon circulation in West Africa.

Tropical East Africa and the Arabian Peninsula experience drying of 0.1-0.2 mm/day due to the weakening of the Somali Jet, which drags moisture towards the inland regions of East

Africa (Somalia, Ethiopia, Djibouti and Eritrea) and the southern parts of the Arabian Peninsula, including Yemen and Oman. This is consistent with the suggestions in early studies pointing out that the suppression of the ISM by volcanic cooling weakens the Somali Jet, resulting in less transport of moisture to eastern Africa (Aiki et al., 2006), and consequently weakens the Hadley updraft motion, contributing to the southward shift of the ITCZ and even affecting the West African monsoon (Camberlin et al., 2010; Flaounas et al., 2012).

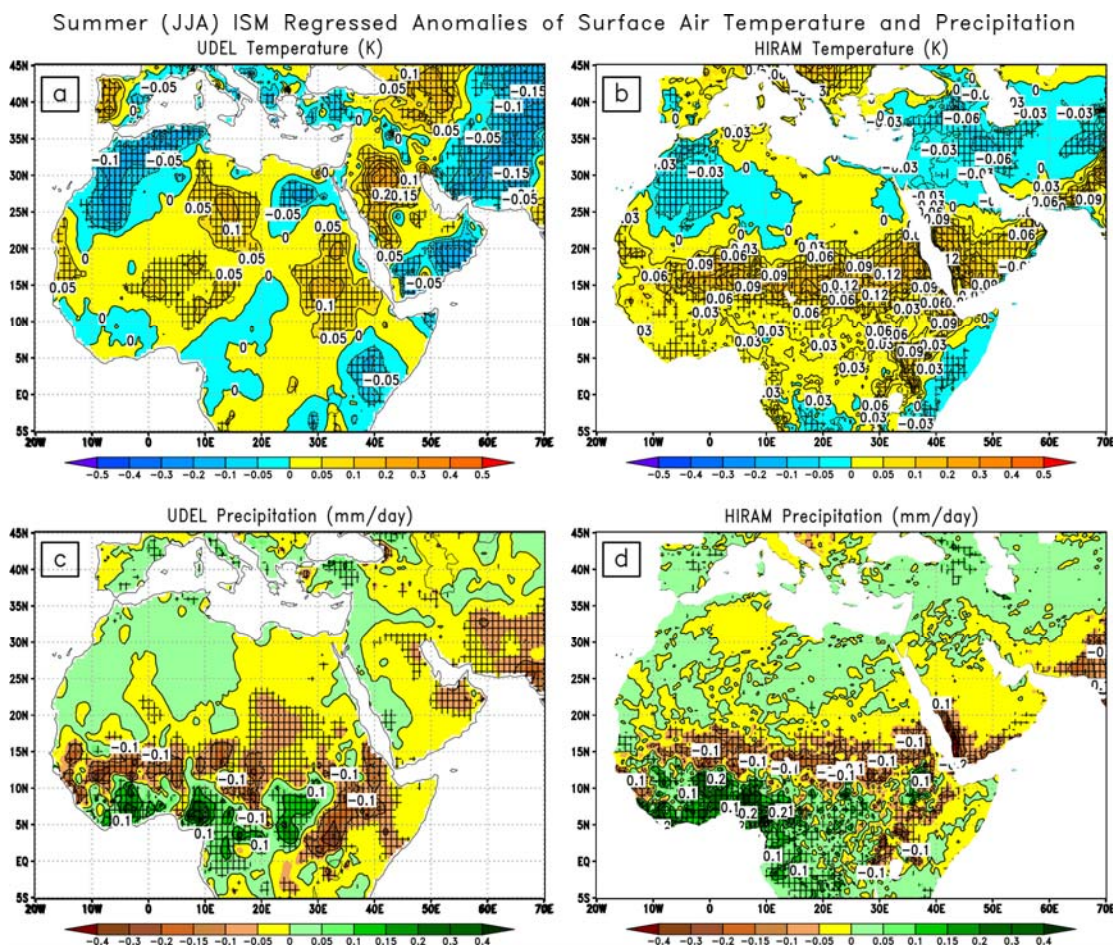


**Figure 4.10:** Anomalies of ISM-regressed surface air temperature (K) and precipitation (mm/day) composited over two summer (JJA) seasons after both the El Chichón and Pinatubo eruptions. The temperature composites are calculated using a) UDEL observations, b) HiRAM output, and precipitation composites using c) UDEL observations, d) HiRAM output. Hatching shows the statistically significant areas with at least 95% confidence level examined by bootstrapping with replacement test.

#### 4.4.6.3. Volcanic direct impacts

Figure 4.11 shows the anomaly of surface air temperature and precipitation in post-eruption

summers regressed on the residual term (volcanic effect; computed by subtracting the regressed impacts of climate trend, ENSO and the Indian monsoon from the corresponding total anomaly). Cooling (Figures 4.11a and 4.11b) is seen over most of the MENA region, except the tropical belt, West Africa and the Horn of Africa, where I see warming in both the model and the observations. This warming is consistent with the southward shift of the ITCZ and suppression of the WAM. Cooling reaching 0.5 K is more pronounced over Western Sahara, Morocco and the Arabian Peninsula (Jordan, Syria, Iraq and Saudi Arabia), both in the model and the observations; I attribute this to the radiative cooling of volcanic aerosol and the associated feedbacks (Atwater, 1970; Mitchell, 1971; Crutzen, 2006; Hatzianastassiou et al., 2007).

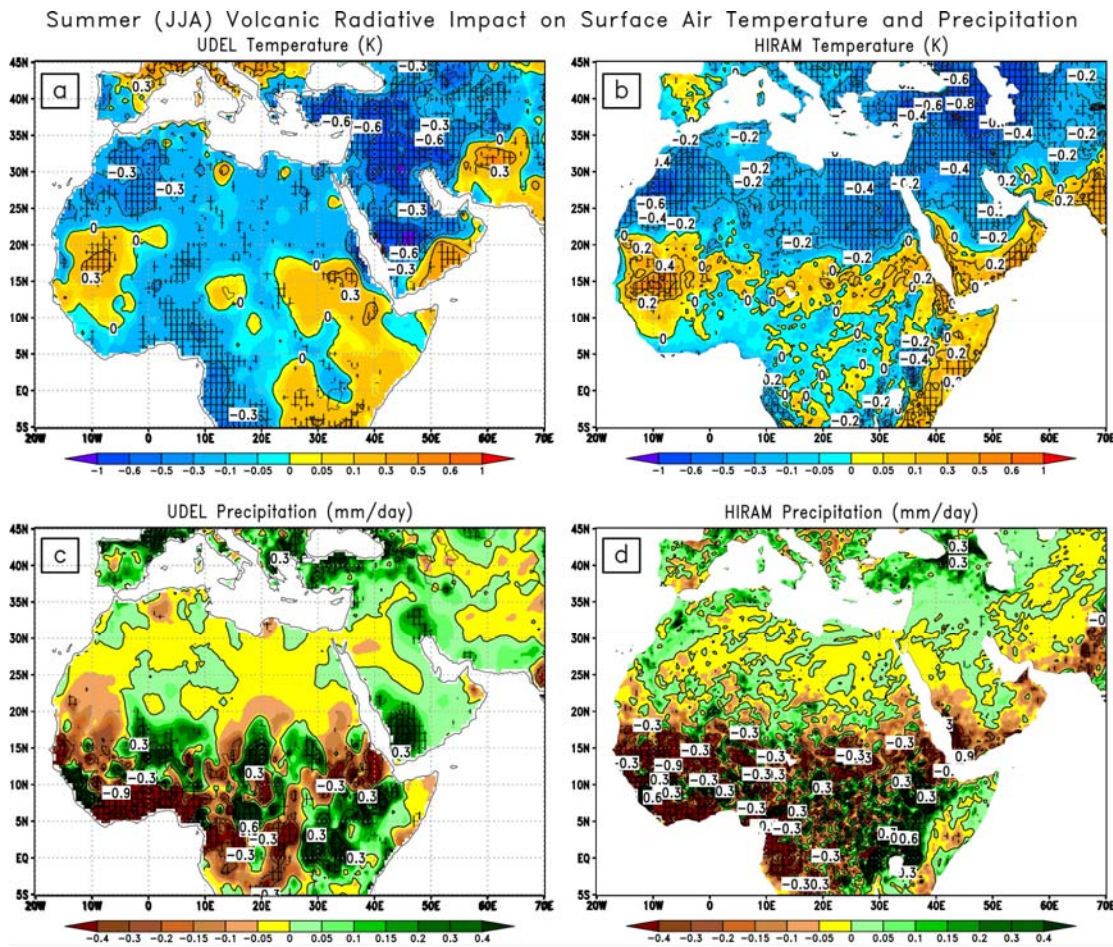


**Figure 4.11:** Summer (JJA) anomalies of surface air temperature (K) and precipitation (mm/day) regressed on the residual term (volcanic effect) composited for two winter seasons following both the El Chichón and Pinatubo eruptions. The temperature composites are calculated using a) UDEL observations, b) HiRAM output, and precipitation composites using c) UDEL observations, d) HiRAM output. Hatching shows the statistically significant areas with at least 95% confidence level examined by bootstrapping with replacement test.

Both the model and the observations depict a significant decrease in precipitation (Figures 4.11c and 4.11d), peaking at -0.6 mm/day (nearly half of the total anomaly), over the African tropical regions south of 20°N, especially during the WAM. The drying in East Africa south of 10°N peaks at -0.5 mm/day. The precipitation anomalies over the Arabian Peninsula are largely inconsistent between the model and the observations. In summer, the ITCZ, associated with the upward branch of the regional Hadley Circulation, moves northward as a result of the seasonal increase of solar heating in the Northern Hemisphere. But solar dimming caused by volcanic aerosols suppresses the northward migration of ITCZ, resulting in a decreased cloud amount and an associated decrease in rainfall over the tropical ITCZ region. The weakening of

WAM in post-eruption summers, seen in Figures 4.11c and 4.11d, is consistent with the decrease in the Hadley vertical mass flux in this region (Figure 4.5). It causes reduced moisture transport to the tropical Saharan rain belt and the summer ITCZ region, amplifying the drying effect.

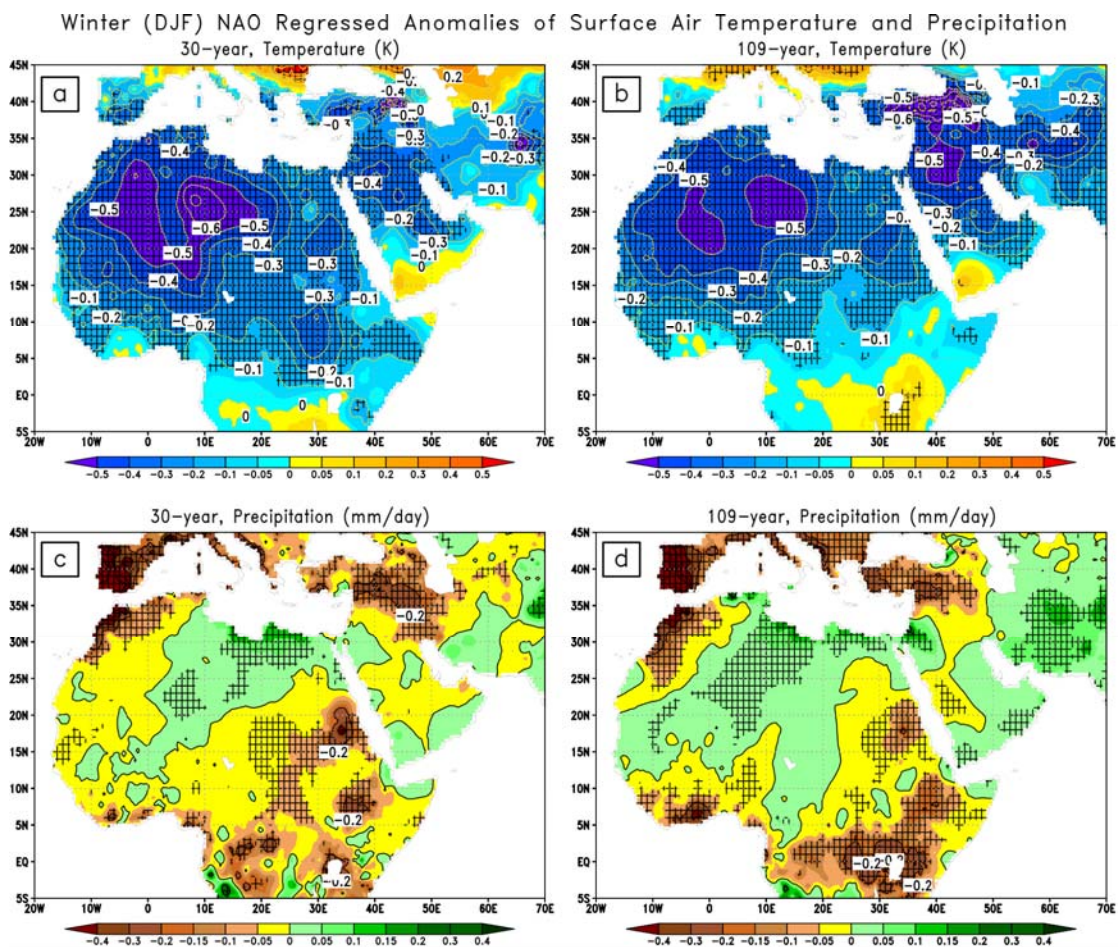
The warming and drying belt at 15°N has a quasi-dipole meridional structure and is formed by the southward retreat of the ITCZ in central and East Africa. Warming along the 15°N belt is caused by a decrease in the cloud amount and a resulting increase in the net shortwave radiation reaching the surface. This belt-like anomaly is better seen in the model than in observations, probably because of natural variability and scarce measurements for this region. Increased precipitation over the Horn of Africa is due to the southward shift of the ITCZ and the increased vertical mass flux  $M_{\phi}$  in this region (Figure 4.5).

#### **4.4.7. Multiple Regression on the 30-Year and 109-Year Datasets**

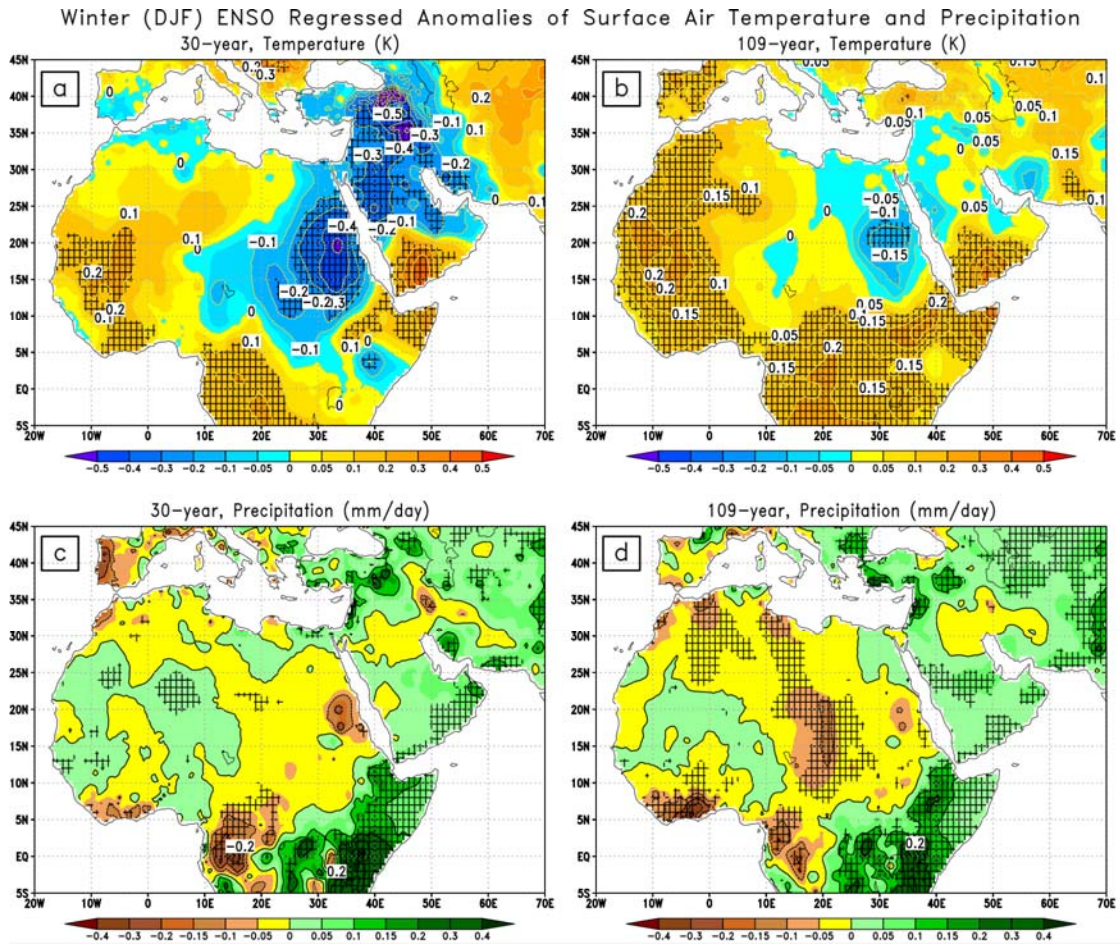
In order to test the robustness and statistical stability of the simulated and observed results shown above, I conduct a multiple regression analysis using UDEL observations over almost the entire period for which they are available (1900-2008 i.e., 109-year). I follow the same multiple regression procedure as is used for the analysis over the 30-year (1979-2008) period; however, the climate trend over the 109-year period is not linear and I have to consider the polynomial trend (see Section 3.3, equations 5-8). For polynomial regression case, the trend index (i.e., standardized year index) as well as NAO, ENSO and ISM indices are extended to 109-year period. As in the main part of the paper, the results are presented as DJF and JJA two-year composites following the El Chichón and Pinatubo tropical eruptions. Assuming that volcanic eruptions and El Niño events are relatively rare, a comparison of the results from the 30-year analysis with those conducted for a considerably longer 109-year period will certainly increase the confidence in these results.

Figure 4.12 shows a comparison of the anomaly patterns for NAO-regressed winter surface temperature and precipitation fields, calculated using the 30 and 109-year observations, following both the eruptions. These plots show that the positive phase of NAO induces consistent surface temperature and precipitation patterns at both time scales, thereby indicating that my 30-year results are robust. The 109-year anomalies are slightly more statistically significant, as expected. Figure 4.13 shows the ENSO-regressed winter anomalies of surface air temperature and precipitation for the 30-year and 109-year periods obtained using UDEL observed dataset. The anomalies are largely consistent; however, the 109-year cooling response over the Arabian Peninsula and East Africa is somewhat weaker and closer to the model prediction (Figure 4.6a and 4.6b) than the 30-year, and both precipitation and temperature anomalies are more

statistically significant in the 109-year analysis. The comparison of the 30-year ENSO-regression analysis during summer with that conducted for a longer 109-year period clearly shows consistent warming and drying anomalies over the tropical region (Figure 4.14), similar to what I see during winter. Figure 4.15 compares the 30-year and 109-year ISM-regressed temperature and precipitation anomalies; they appear to be very consistent with wider areas of statistical significance and a slightly stronger drying in the 109-year analysis.



**Figure 4.12:** Anomalies of NAO-regressed surface air-temperature (K) and precipitation (mm/day) composited over two winter (DJF) seasons following both the El Chichón and Pinatubo eruptions. The temperature composites are calculated using a) UDEL 30-year period, b) UDEL 109-year period, and precipitation composites using c) UDEL 30-year period, d) UDEL 109-year period. Hatching shows the statistically significant areas with at least 95% confidence level examined by bootstrapping with replacement method.



**Figure 4.13:** Anomalies of ENSO-regressed surface air-temperature (K) and precipitation (mm/day) composited for two winter (DJF) seasons following both the El Chichón and Pinatubo eruptions. The temperature composites are calculated using a) UDEL 30-year period, b) UDEL 109-year period, and precipitation composites using c) UDEL 30-year period, d) UDEL 109-year period. Hatching shows the statistically significant areas with at least 95% confidence level examined by bootstrapping with replacement test.

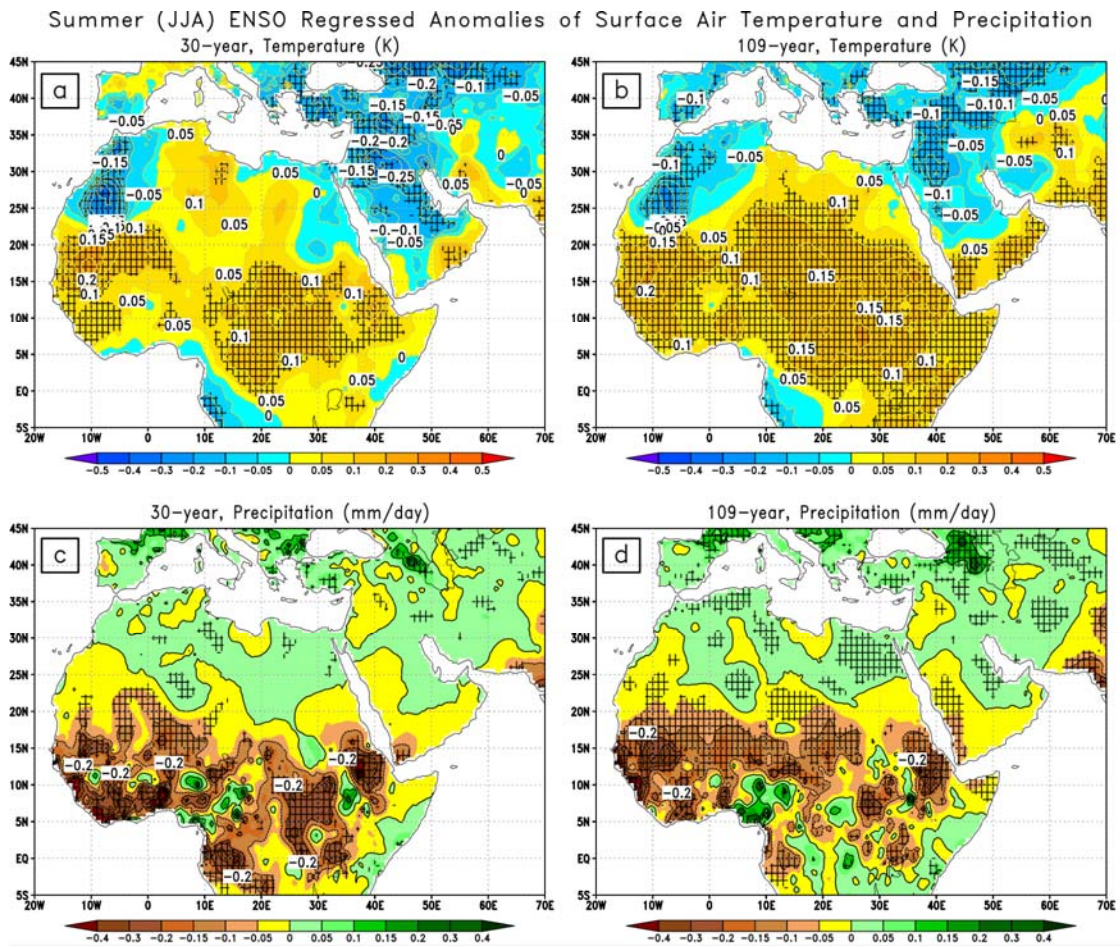


**Figure 4.14:** Anomalies of ENSO-regressed surface air-temperature (K) and precipitation (mm/day) composited for two summer (JJA) seasons following both the El Chichón and Pinatubo eruptions. The temperature composites are calculated using a) UDEL 30-year period, b) UDEL 109-year period, and precipitation composites using c) UDEL 30-year period, d) UDEL 109-year period. Hatching shows the statistically significant areas with at least 95% confidence level examined by bootstrapping with replacement test.

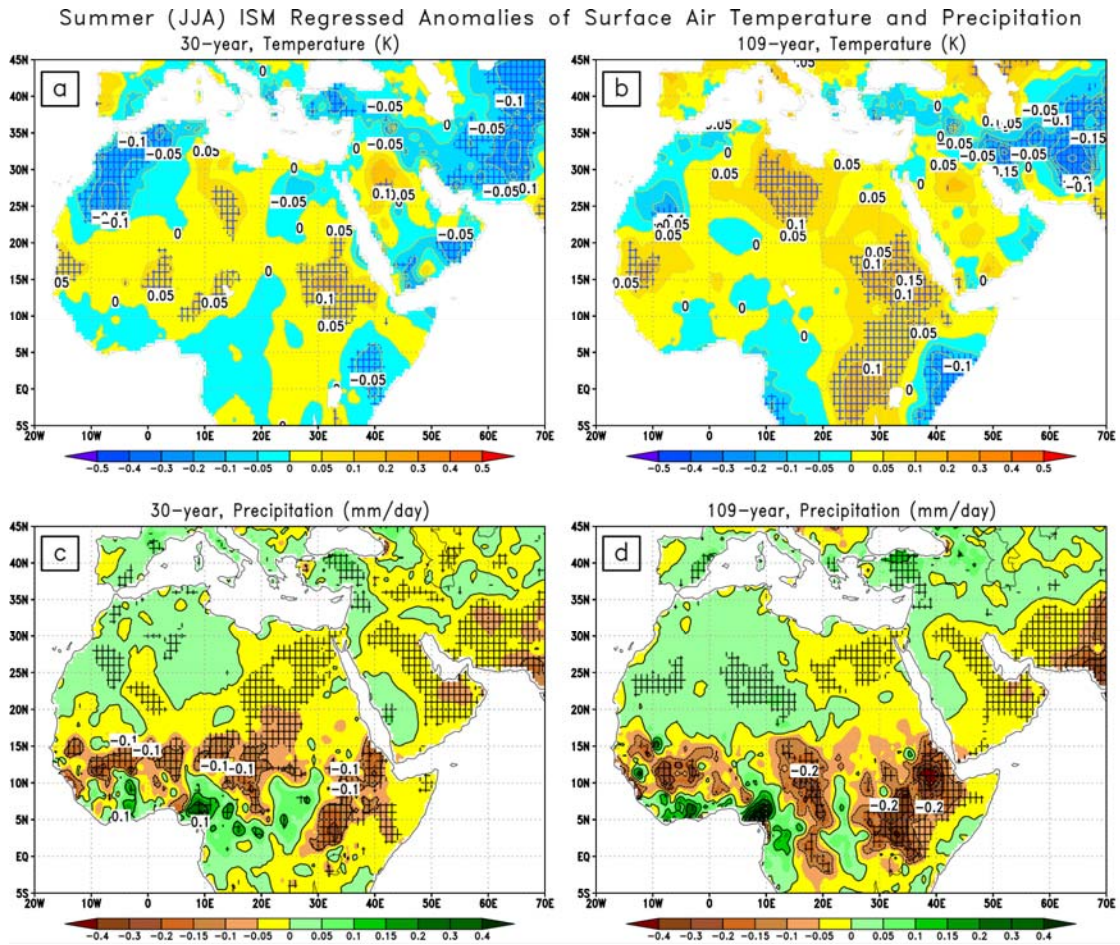


**Figure 4.15:** Anomalies of ISM-regressed surface air-temperature (K) and precipitation (mm/day) composited for two summer (JJA) seasons following both the El Chichón and Pinatubo eruptions. The temperature composites are calculated using a) UDEL 30-year period, b) UDEL 109-year period, and precipitation composites using c) UDEL 30-year period, d) UDEL 109-year period. Hatching shows the statistically significant areas with at least 95% confidence level examined by bootstrapping with replacement test.

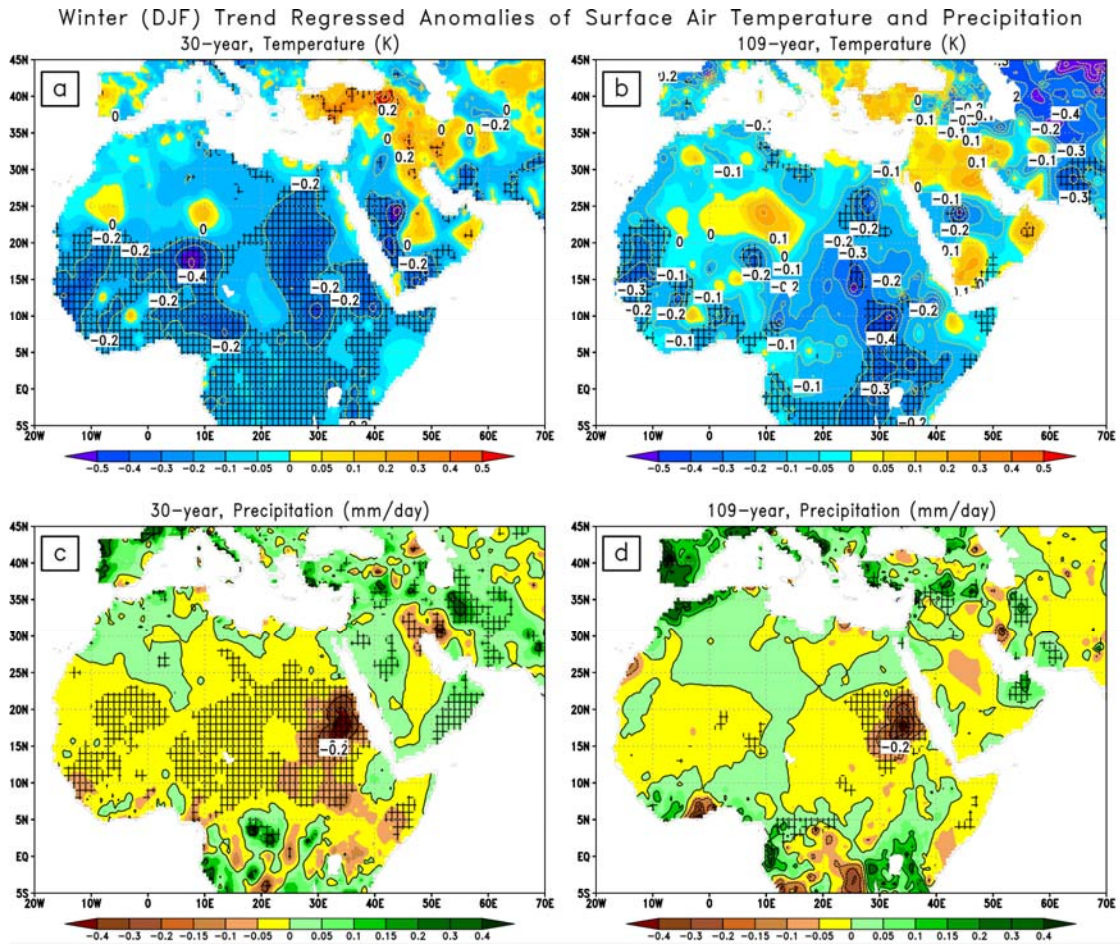


**Figure 4.16:** Anomalies of trend-component-regressed surface air temperature (K) and precipitation (mm/day) composited for two winter (DJF) seasons following both the El Chichón and Pinatubo eruptions. The temperature composites are calculated using a) UDEL 30-year period, b) UDEL 109-year period, and precipitation composites using c) UDEL 30-year period, d) UDEL 109-year period. Hatching shows the statistically significant areas with at least 95% confidence level examined by bootstrapping with replacement test.

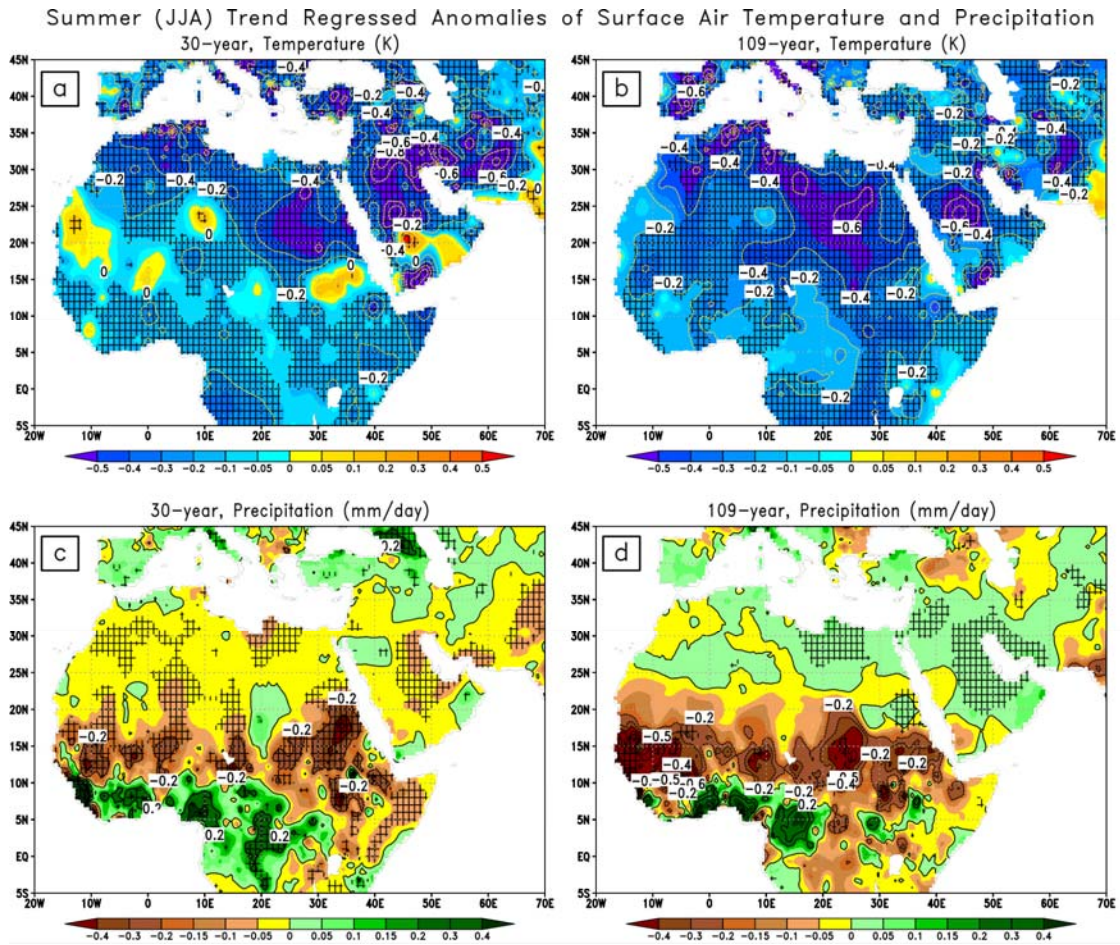


**Figure 4.17:** Anomalies of trend-component-regressed surface air-temperature (K) and precipitation (mm/day) composited for two summer (JJA) seasons following both the El Chichón and Pinatubo eruptions. The temperature composites are calculated using a) UDEL 30-year period, b) UDEL 109-year period, and precipitation composites using c) UDEL 30-year period, d) UDEL 109-year period. Hatching shows the statistically significant areas with at least 95% confidence level examined by bootstrapping with replacement test.

Figures 4.16 and 4.17 show the trend-component-regressed anomalies of surface air temperature and precipitation in post-eruption winter and summer season respectively, calculated using the UDEL observations for the 30-year and 109-year periods. Both the 30-year and 109-year periods compare well for winter and summer seasons. The climate trend contributions to temperature and precipitation changes are quite significant. The trend contributed anomaly effect is more pronounced in post-eruption summer, peaking at  $-0.6$  K and  $-0.5$  mm/day for temperature and precipitation, respectively.

These results give us an estimate of the statistical uncertainty in observations, confirming that it is acceptably small, and demonstrate that the 30-year period is sufficient to draw reliable

statistical conclusions, which I extend to the 30-year model analysis.

I noticed negligibly small differences while comparing the results of longer period with shorter period, especially in the hatching of significant areas among the left panels showing 30 years period i.e., Figure 4.12(a, c) versus Figure 4.7(a, c), Figure 4.13(a, c) versus Figure 4.6(a, c), Figure 4.14(a, c) versus Figure 4.9(a, c), and Figure 4.15(a, c) versus Figure 4.10(a, c). The hatching is different because of the trend component. In the plots where I compared UDEL with the HIRAM results using 30 years period, I removed the linear trend both in the observations and in the HIRAM output. However, the trend, especially over the longer period, need not be linear, therefore, while comparing the long time period (109 years) with the shorter period (30 years) using UDEL observations, I removed polynomial trend which caused slight variations, especially in the hatching of significant areas at 95% confidence level.

#### **4.4.8. Robustness of Climate Responses using Multiple Regression Analysis**

Determining the statistical significance of the differences in climate responses to volcanic eruptions computed using multiple regression analysis is a more demanding statistical test than simply determining the statistical significance of a mean response. Determination of the statistical significance of differences is not always achievable, especially with observations and even with composites as strong volcanic events are rare. Most if not all of the existing “volcanic” studies therefore qualitatively have compared observed and simulated signals without proving the statistical significance of the differences between them (Stenchikov et al., 2002; 2006; 2009).

To avoid possible multi-collinearity between ENSO and volcanic predictor, I followed the residual approach (see Section 3.3 and Section 4.3 for details) to compute volcanic direct impact. The residual signal retain significant portion of the total signal. So testing the robustness of multiple regression analysis used here by conventional statistical methods such as coefficient of determination is not effective. Therefore, I employ an alternative methodology to verify that my regression analysis is meaningful and the contribution of internal noises is negligible compared to the leading climate drivers considered in this analysis. The details are as follows.

The internal variability or climate noise affects not only the residual components but also all components of the multiple linear regression analysis. The internal variability could be split into low frequency, associated with the ocean, and high frequency, associated with the atmosphere. The ocean variability is damped as I use the prescribed observed SST in my simulations. The high-frequency noise is expected to be suppressed by compositing and ensemble averaging to make the volcanic effect statistically significant.

To further estimate the contribution of the internal variability in the response to direct volcanic radiative cooling, I calculated the residual-component-regressed fields for all non-volcanic years in both seasons (see Figure 4.18 and Figure 4.19) and compared them with those in post-eruption years. The residuals calculated for non-volcanic years are almost an order of magnitude smaller than those calculated for post-eruption years (see Figure 4.9 and Figure 4.12), suggesting that the effect of internal variability in this case is relatively small. This analysis lends support that the residual signal mainly contains volcanic impact and is less affected by internal noise and other variabilities, which are not considered in the regression analysis.

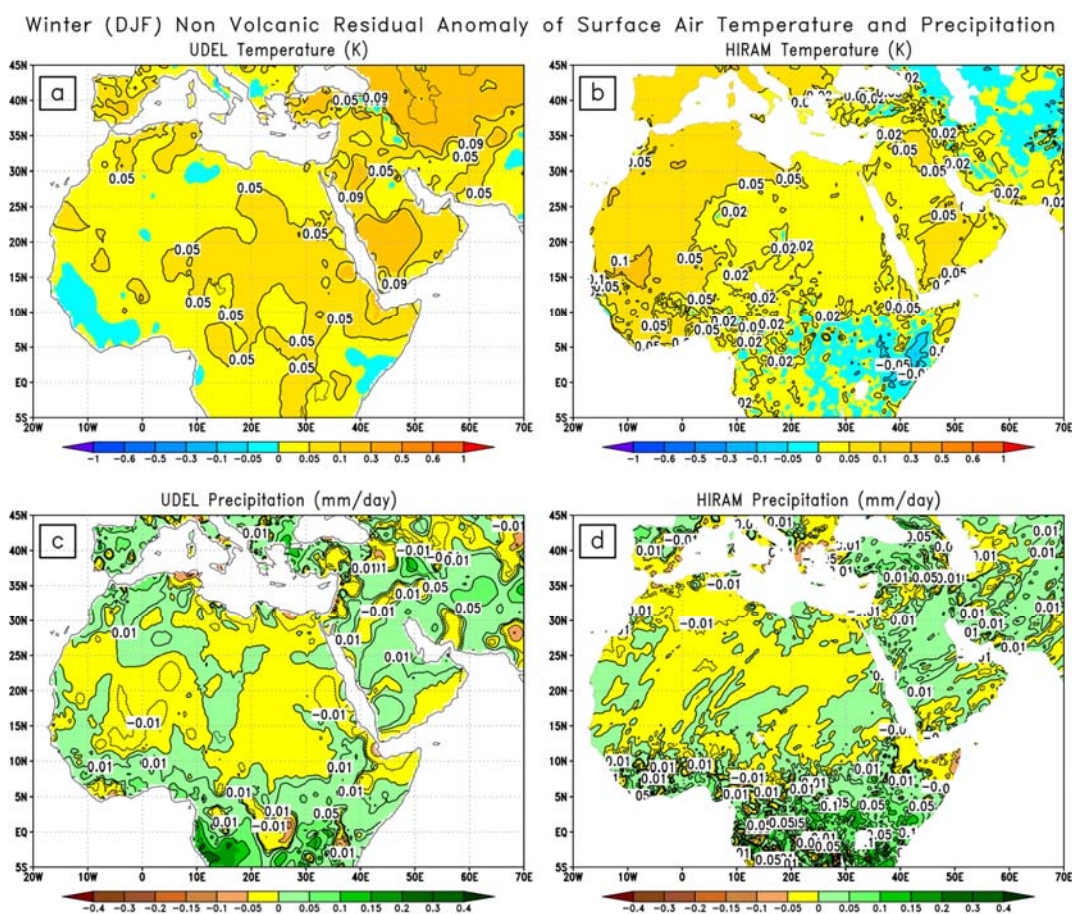


**Figure 4.18:** Anomalies of residual-component-regressed surface air temperature (K) and precipitation (mm/day) calculated for non-volcanic winters using a) UDEL temperature observations, b) HiRAM temperature output, c) UDEL precipitation observations, and d) HiRAM precipitation output.

Summer (JJA) Non Volcanic Residual Anomaly of Surface Air Temperature and Precipitation

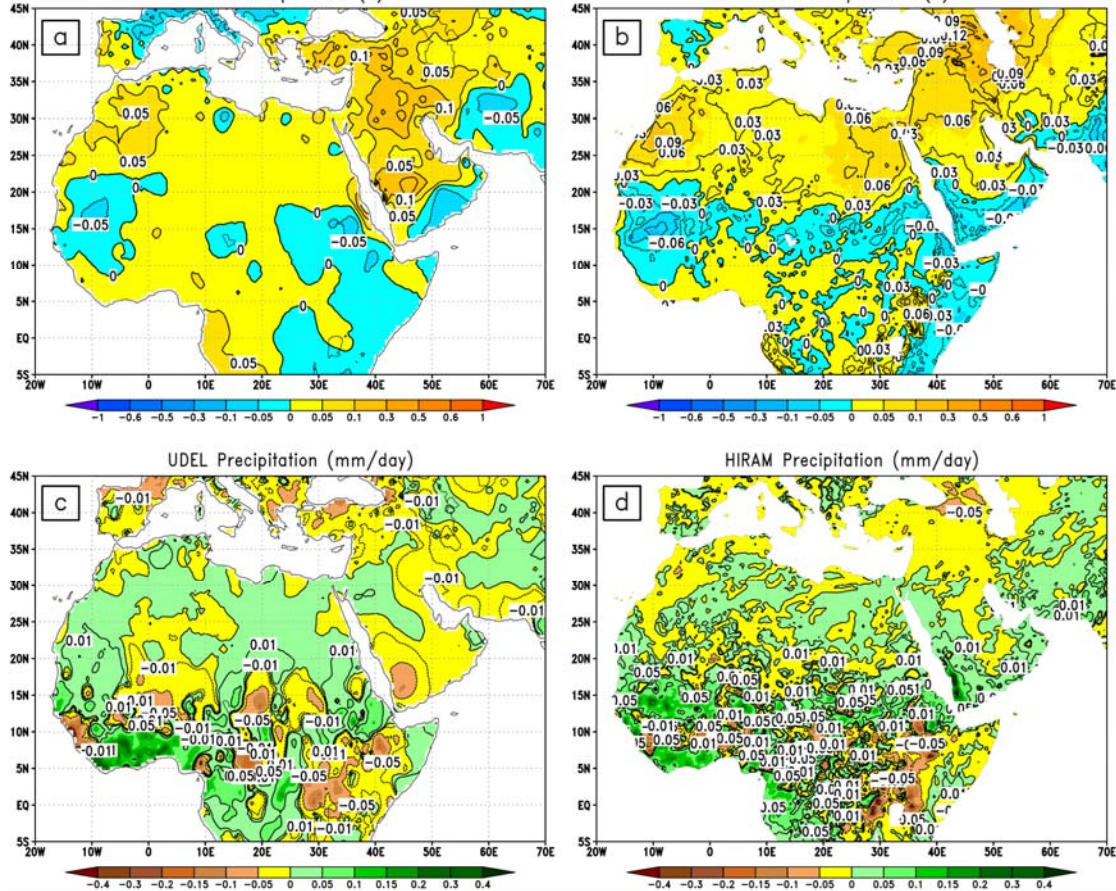


**Figure 4.19:** Same as Figure 4.18 but for summer season.

The further support my findings, a time series plot of the residual component for surface air temperature and precipitation in winter (DJF) averaged over the entire MENA region (Figure 4.20 and Figure 4.21) is shown. A significant decrease in both observed and simulated surface air temperature and precipitation during the time of the El Chichón (1982) and Pinatubo (1991) eruptions strongly suggests that the residual component reflects the effect of eruption. Furthermore, this also suggests the selected factors in multiple linear regression analysis are likely to be the leading modes that affect the MENA climate variability.

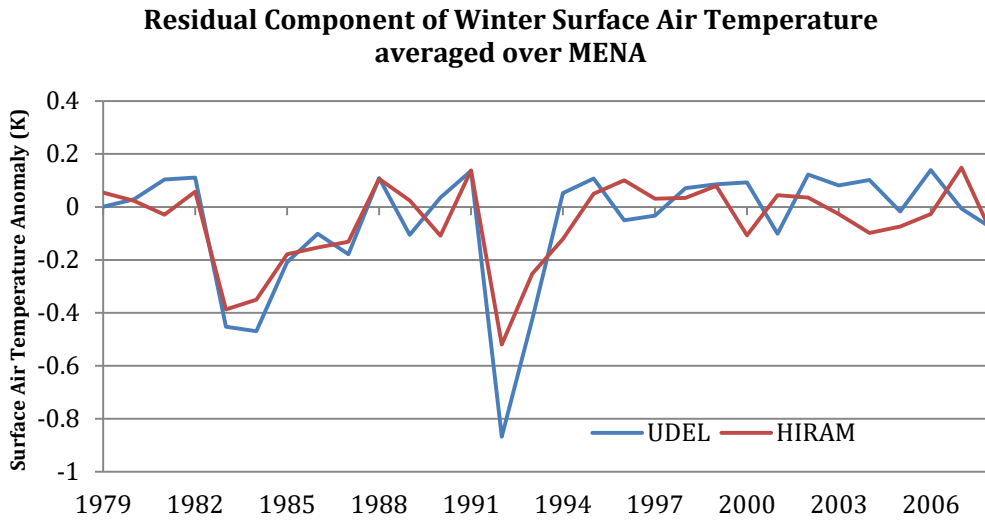


**Figure 4.20:** Time series of the residual component in winter (DJF) surface air temperature averaged over the MENA region (20°W-70°E, 5°S-45°N).

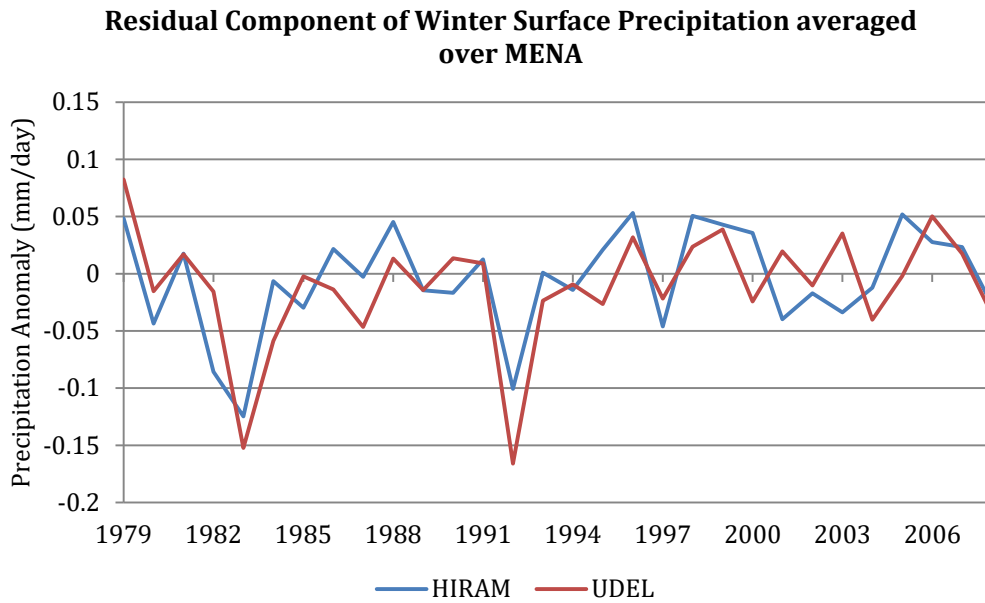


**Figure 4.21:** Time series of the residual component in winter (DJF) surface precipitation averaged over the MENA region (20°W-70°E, 5°S-45°N).

#### 4.5. Summary and Conclusions

The strong regional circulation anomalies, along with direct volcanic aerosol radiative cooling,

could cause an enormously strong climate response over the MENA region. To better quantify these effects, I use UDEL observations, high-resolution (with the effective 38 km grid spacing) CFS reanalysis that accounts for volcanic aerosols and a GFDL global HiRAM with the effective 25 km grid spacing. This chapter focuses on the winter and summer anomalies in two post-eruption years for El Chichón and Pinatubo. I analyze changes in solar radiation, surface temperature, cloud amount and precipitation, comparing the model responses with the UDEL temperature and precipitation observations, and the CFSR solar radiation and vertical mass flux anomalies. The high-resolution global HiRAM simulations and CFSR ensure the grid resolution is amply sufficient for regional climate analysis, with the ability to account for interactions (teleconnections) among processes on the global and regional scales.

I assume that the MENA region is affected by both direct volcanic radiative cooling from within the region and by teleconnections from outside the region, which are partly enforced by the volcanic radiative effect and partly caused by natural variability. The rationale of this study is to decompose, using multiple linear regressions, both the observed and simulated anomalies in post-eruption years into the effects of the direct radiative cooling within the MENA region and external teleconnections, and then use this analysis to evaluate the physical mechanisms of regional climate sensitivity. The external factors I consider include ENSO, NAO and ISM. Climate trends are also included in the multiple regressions. While the volcanic effect on NAO and ISM is expected within the model, ENSO phase (SST) is prescribed using the observations. The residual components of the multiple regression analysis reflect the direct volcanic effect to cooling, as discussed in Section 4.4.4.

I find strong precipitation and temperature anomalies in post-eruption years. The MENA temperature anomalies peak at -1.5 K, which is three times of the observed global cooling after the Pinatubo eruption. In winter, both the observations and the model-based analysis suggest that most of the total post-eruption cooling over the MENA region (predominantly in central and western areas) is contributed by the anomalously positive NAO, and less by the direct regional radiative cooling (see Figures 4.8 and 4.9). Both the direct volcanic effect and the NAO reduce precipitation in tropical Africa, but the positive ENSO enhances precipitation over the Horn of Africa. The observed ENSO effect is relatively strong, causing cooling in eastern and central Africa, the Middle East, and the eastern Mediterranean. This is not well captured by the model.

The positive phase of NAO is observed after major equatorial volcanic eruptions like El Chichón and Pinatubo. It is likely to be forced by heating of the equatorial lower stratosphere by volcanic aerosols and by an increasing equator-to-pole temperature gradient in the lower stratosphere (Stenchikov et al., 2002; 2004, 2006). The NAO in post-eruption years is affected by

internal variability. While up-to-date climate models underestimate the NAO response to volcanic eruptions (see, e.g., Driscoll et al., 2011; Stenchikov et al., 2006), in my simulations and in the observations, this effect is generally statistically significant, suggesting that this post-eruption NAO signal might be less affected by internal variability.

In summer, the decrease in the thermal gradient between the ocean and the MENA landmasses caused by the direct volcanic cooling weakens the African branch of the Hadley Cell and the WAM. The ISM plays a significant role in weakening the Hadley circulation, and in strengthening coastal precipitation both in West Africa and over the Horn of Africa to the east. The overall drying anomaly during summer from radiative cooling is enhanced over the northern border of the rain belt and the Sahel region by a post-eruption reduction of the ISM and WAM rainfall. The cloud amount pattern and associated changes in precipitation over the interior of the African continent suggest a southward shift of the Northern Hemisphere summer ITCZ, facilitated by volcanic cooling and weakening of the ISM. A decrease in cloud amount over the MENA tropical belt in the summer season regionally increases downward solar radiation, worsening drought conditions.

The diagnosis of the regional Hadley Cell vertical mass flux ( $M_\phi$ ) over the MENA region (Figure 4.5) is consistent with these findings and shows a weakening of the large-scale subsidence over the Mediterranean, due to damping of the ISM, weakening vertical mass flux over the Sahara and at the northern border of the ITCZ, and strengthening vertical mass flux south of  $15^\circ\text{N}$ , associated with the southward shift of the ITCZ. The ITCZ shift is more uniform in central and East Africa, while decreased  $M_\phi$  in the WAM is seen in West Africa. It is especially pronounced in the HiRAM simulations. Thus, decreased cloud amount at the northern border of the ITCZ in central and East Africa is caused by the weakening of the local Hadley Cell and a southward shift of the ITCZ, but in West Africa decreased moisture is dominated by the weakening of the WAM.

The HiRAM simulations, with effective 25 km grid spacing, resolve the regional processes in the MENA region and reproduce well the radiative forcing in comparison with the CFSR and previous studies. This high-resolution atmospheric model is an ideal tool for regional impact studies, as it has the spatial resolution of a regional model but interactively accounts for teleconnections. However, I find that HiRAM largely underestimates winter cooling due to a weaker NAO response and generates an incorrect NAO spatial pattern over the MENA region. This is consistent with the finding that global climate models have shown an inability to fully reproduce the seasonal and regional nature of volcano-induced climate change (Stenchikov et al., 2006; Otterå, 2008; Driscoll et al., 2012). The model performs much better in the summer season,

capturing well the volcanic direct radiative impacts over the MENA region and the impact of the ISM on the WAM.

This analysis provides a useful test of the mechanistic regional behavior of the state-of-the-art global high-resolution atmospheric model, HiRAM, in reproducing anomalies in post-eruption years over the MENA region, and evaluates the major teleconnections (ENSO, NAO and ISM) that affect the MENA region. It further emphasizes that the MENA climate regime is highly sensitive to volcanic impacts, and improving simulation of NAO, ENSO and ISM is crucially important for better simulating climate variability and change in the MENA region. Strong low-latitude eruptions have the potential to affect agricultural productivity, especially in the Sahel region, possibly leading to famine and severely influencing the lives of the African inhabitants (Haywood et al., 2013).

## **Chapter 5. Regional Sensitivity of Hadley Circulation to Post-eruption Anomalies**

This chapter is an extension to the research discussed in preceding chapters in which I analyzed the sensitivity of MENA tropical regions to volcanic, NAO, and ENSO forcing. In this chapter, I tried to unfold and better understand the post-eruption mechanisms that affect the Northern Hemispheric updraft branch of Hadley Cell (HC), that is, the Inter-tropical Convergence Zone, in the summer season.

The direct radiative effects of volcanic eruptions resulting in solar dimming, stratospheric warming, global surface cooling and reduction in evaporation are well documented. However, eruptions also cause indirect climatic impacts that are less understood (Timmreck et al., 2012). For example, solar-dimming induced by volcanic aerosols could cause changes in tropical Hadley Cell that in turn largely affect evaporation, cloud distribution, and precipitation patterns. Therefore, understanding the sensitivity of HC to volcanism is essential, as this circulation is directly related to the precipitation changes in the tropics and with other large-scale circulations. Hence, to better understand the post-eruption sensitivity of HC and associated changes in the hydrological cycle, simulations for the El Chichón and Pinatubo tropical eruption are conducted using a High-Resolution Atmospheric Model (HiRAM), effectively at 25 km and 50 km grid spacing and the modeling results are compared with observational and reanalysis products. Both the model and observational analysis show weakening, shrinking and equatorward displacement of the updraft branch of HC in post-eruption years caused by the equatorward shift of midlatitude jets and hemispheric land-sea thermal gradient. As Inter-tropical Convergence Zone (ITCZ) is tightly-coupled to the rising branch of HC, hence post-eruption weakening and equatorward displacement of HC cause weakening of the ITCZ that adversely affects rainfall distribution in the monsoon fed regions, especially the South Asian, Middle Eastern and African tropical rain belt regions. The distribution of cloud contents in post-eruption years produced by the HIRAM model suggests a southward shift of the ITCZ. The HIRAM results are largely in agreement with the reanalysis, observations and previous studies indicating that this model performs reasonably well in reproducing the global and regional-scale dynamic changes caused by volcanic radiative forcing.

### **5.1. Problem Formulation and Motivation**

The Hadley circulation, a global scale meridional overturning circulation in the tropical atmosphere, plays a significant role in the inter-hemispheric distribution of heat and water vapors (Lindzen and Pan, 1994; Oort and Yienger, 1996; Cook, 2004; Webster, 2004; Quan et al., 2004; Seidel and Randel, 2007; Gastine et al., 2009). The Hadley circulation is responsible for the trade

winds in the tropics and control low-latitude weather patterns. An intensification/weakening of the Northern Hemisphere (NH) Hadley circulation in boreal summer leads to an increased/decreased water vapors inflow across the equator into Northern Hemisphere resulting in positive/negative anomalies of precipitation in the NH tropics (Hudsen et al., 2006; Davis and Rosenlof, 2012; Fu and Lin, 2013; Nguyen et al., 2013; Wilcox et al., 2012; Zhou et al., 2011; Fu et al., 2006). A slight perturbation in this large-scale tropical atmospheric circulation by the internal or external climate forcings will have substantial consequences for the hydrologic cycle (Trenberth and Dai, 2007; Trenberth, 2011; Bala et al., 2008; Wild et al., 2008; Dogar and Kucharski et al., 2017). The response of large scale Hadley circulation to anthropogenic greenhouse gas forcing and the resultant variation in the hydrological cycle have largely been studied (Held and Soden, 2006; Vecchi and Soden, 2007; Tao et al., 2016). Focusing in the later part of the 20th century, a large number of studies have shown a widening, strengthening and poleward shift of the HC and associated changes in the tropical belt (Seidel et al., 2008). The observational and model-based studies have linked these changes in HC to global warming (Seidel et al., 2008; Johanson and Fu, 2009; Kang and Lu, 2012), stratospheric ozone depletion (Seidel et al., 2008; Johanson and Fu, 2009; Seidel and Randel, 2007) and associated tropospheric warming and stratospheric cooling (Fu et al., 2006).

The sensitivity of HC to climate forcings such as global warming and circulation changes such as El Niño Southern Oscillations (ENSO) has been largely discussed. However, there are fewer studies available (Trenberth and Dai, 2007; Trenberth, 2011; Iles and Hegerl, 2014; Haywood et al., 2013; Joseph and Zeng, 2011) that discussed the impact of volcanic radiative forcing on HC, especially on the ITCZ and subsequent changes in the water budget over the tropical regions. Some studies have discussed the widening and poleward expansion of the midlatitude jets and HC in the past couple of decades (Hudson et al., 2006; Davis and Rosenlof, 2012; Fu and Lin, 2013; Wilcox et al., 2012; Zhou et al., 2011; Fu et al., 2006; Oman et al., 2006; Barnes and Polvani, 2013). Earlier studies suggested that ozone depletion could be responsible for the recent widening of HC (Polvani and Kushner, 2002; Polvani et al., 2011) as it may induce an equator to pole temperature gradient in the stratosphere that consequently affects HC. Recently it has been established that this expansion of HC is partly attributed to ozone-induced stratosphere cooling, tropospheric heating (caused by global warming) and resultant stratosphere-troposphere temperature gradient (Fu et al., 2006) and associated pressure and wind changes.

It has also been shown in previous studies that stratospheric volcanic aerosols could cause warming in the lower stratosphere as well as cooling in the troposphere and at the surface. Such post-eruption changes consequently initiate equator-to-pole thermal gradient in the lower

stratosphere as well as the hemispheric land-sea thermal gradient at the surface. Therefore, these changes are anticipated to cause a significant effect on Hadley circulation, presumably in an opposite way, as is the case under global warming scenarios (Trenberth, 2011). Hence, understanding the sensitivity of Hadley circulation following volcanic eruptions, such as its meridional movement, strengthening, or weakening is essential for human activities. Moreover, this circulation is directly related to the precipitation activity in the tropics, and with other large-scale circulations that affect human activities through changes in surface winds, precipitation, droughts, etc. Thus, it is important to study the possible changes in the tropical Hadley circulation, and tropical convective activities, under a climate change environment, and the consequences that they would have following explosive tropical eruptions. To better understand such effects, I investigated the response of HC following El Chichón and Pinatubo tropical eruptions.

For this purpose, I used the state of the art global atmospheric model with a very high spatial resolution (at 50 km and 25 km), typically comparable to the resolutions of regional climate models, to study the sensitivity of HC to the radiative perturbations caused by large-scale tropical volcanic eruptions. The idea of choosing two different HIRAM resolutions is to see if there could be any improvement in the simulations of volcanic impacts with improved resolution. Due to their fine grid spacing, important processes such as large-scale condensation, land-sea interaction, and topographical forcing are better resolved in high-resolution GCMs (Boyle & Klein, 2010; Lau & Ploshay, 2009; Harris et al., 2016). Recent studies further emphasized that the regional convective structure and precipitation change are very sensitive to the model horizontal resolution (Bui et al., 2019; Liu et al., 2018). In this chapter, I focus on the following questions.

1. How is the HC anomaly in the post-eruption years?
2. How sensitive is the ITCZ, especially African, Middle Eastern and South Asian ITCZ to volcanic perturbations?
3. How well can HiRAM (effectively at 50 km and 25 km horizontal resolutions) simulate post-eruption HC circulation and ITCZ shift in the post-eruption years?

Rest of the paper is arranged as follows: Data and methodology are discussed in Section 5.2. Post-eruption shortwave radiative response as well as changes in HC using vertical velocity, meridional mass stream function and associated precipitation and wind patterns, are documented in Section 5.3. Section 5.4 concludes this study.

## **5.2. Model, Data and Methodology**

The description of the high-resolution atmospheric model, HiRAM that is used in this study is available in Chapter 2, Section 2.2. I employed Atmospheric Model Intercomparison Project

(AMIP)-style simulations of HiRAM effectively at 50 km and 25 km horizontal resolutions (Zhao et al., 2009). This high-resolution is comparable to the resolutions of regional climate models and is very important to better resolve regional-scale dynamic features that are important especially in the tropics. In these HiRAM-AMIP simulations, the model is forced using Hadley Center observed sea surface temperature (SST) and sea-ice boundary conditions (Rayner et al., 2003). Three different realizations covering the period (1976-2008) were produced using different SST initial conditions that are obtained after several integrations of the atmosphere-only model. First three years of simulation period are excluded from the analysis in order to avoid spin up effects.

The volcanic aerosol forcing data for both the eruptions used in the model is discussed in Chapter 2, Section 2.2. I compared HiRAM results with Climate Forecast System Reanalysis (CFSR), 20th Century Reanalysis (20CR) of National Oceanic and Atmospheric Administration (NOAA) as well as ERA-Interim reanalysis. The details of these data sets are available in Chapter 2 (Section 2.3).

To simulate the impact of volcanic eruptions, I showed anomaly of different climatological parameters by considering their departure from long-term summer (JJA) seasonal mean that is computed using 1979-2008 periods. This seasonal mean summer climatology is computed after excluding two post-eruption summer seasons following both the eruptions. To reduce noise, model results are presented (both for 50 km and 25 km simulations) by averaging over three ensemble members. As large volcanic eruptions induce atmospheric impacts for two-three years, hence, anomalous responses are calculated by averaging over two summer seasons following both the El Chichón and Pinatubo eruptions. A two-tailed student t-test is used to account for post-eruption significant responses at 95% confidence level.

It should be noted that the anomaly of post-eruption years contains both the volcanic effect and the contribution of natural variability caused by ENSO, NAO and other possible internal variability modes. However, a large number of studies show that the ENSO (e.g., Maher et al., 2015; Pausata et al., 2015; Ohba et al., 2013; Predybaylo et al., 2017; Khodri et al., 2017; Adam et al., 2003) and NAO (Stenchikov et al., 2002; 2006, Driscoll et al., 2012; Zambri et al., 2017; Timmreck, 2012; Fischer et al., 2007; Shindel et al., 2004) were modulated by the strong volcanic eruptions, implying that the circulations that happened at the time of eruption contain eruption signal.

### 5.3. Results and Discussion

#### 5.3.1. Vertical Wind and Meridional Mass Stream Function Changes

To quantify the sensitivity of HC to volcanic radiative forcing, zonal-mean omega (vertical wind in Pa/s, displayed in shaded colors) and zonal-mean meridional mass stream function ( $10^8$  kg/s, displayed in contours) are shown in Figure 5.1. The negative and positive values of omega in these plots represent the ascending and descending branch of Hadley Cell respectively. The top panel (Figure 5.1a, b) shows mean pattern and rest of the panels show anomalies (composited over two seasons following both eruption) for the post-eruption El Chichón and Pinatubo cases. The mean pattern is computed using total simulation period (i.e., 1979-2008) after excluding two post-eruption summer seasons both for the 20CR and the HiRAM simulation. Figure 5.1c and 5.1d show Hadley Cell composite anomaly following both the El Chichón and Pinatubo eruptions.

Both the reanalysis and model results depict a weakening of the Northern Hemisphere summer HC and southward migration of its rising branch, the Inter-Tropical Convergence Zone after both the eruptions. Both the El Chichón and Mt. Pinatubo composited anomaly (Figures 5.1c and 5.1h) shows shortening, weakening and equatorward movement of the rising branch of Northern Hadley Cell. The anomalous patterns of both the vertical velocity and associated meridional mass stream function in HiRAM show more pronounced weakening and southward migration of the Hadley Cell (especially for the El Chichón eruption, not shown) than the 20th century reanalysis as the rising and sinking limbs meet at around  $6^{\circ}\text{N}$  in the model compared to 20CR, where they meet at around  $8^{\circ}\text{N}$ . The anomaly of zonal mean vertical velocity and associated meridional mass stream function in the post-eruption years is somehow more compact and southward shift is more obvious in the model simulation compared to 20CR, presumably because the HiRAM has very high resolution and therefore resolves dynamic features of the Hadley circulation reasonably better (especially at regional scales) than 20CR and also because model results are presented by averaging over three realizations which could minimize the effect of internal noise. I also noticed that the El Chichón eruption shows slightly stronger southward shift than Pinatubo eruption (both in the model and 20 CR, not shown) presumably because El Chichón eruption erupted slightly farther northward to equator compared to Pinatubo and therefore produces stronger hemispheric thermal gradient at the surface that produces stronger shift to updraft branch of HC. A slight spatial inconsistency between the model and 20CR especially following Pinatubo eruption (not shown) could be partly accounted for by the contribution of varying pattern caused by internal variability signal that could be different in 20CR and in the model.

To further understand and to see the statistical significance of HC response following both these tropical eruptions, I plotted vertical velocity pattern and associated wind vectors (Figure 5.2) using different reanalysis products. As both the El Chichón and Pinatubo eruptions could roughly induce similar impact (i.e., weakening and southward shift of ITCZ is comparable), I showed composited (averaged over both the eruptions) patterns only. The weakening and southward shift is obvious and the rising and sinking anomalies of the vertical velocity are significant at 95% confidence level in the reanalysis (i.e. ERA-Interim and 20CR), however, both the reanalysis show some spatial differences, such that the rising branch is slightly wider in the reanalysis compared to the model response. The model-produced mean and post-eruption anomaly (both in Figure 5.1 and 5.2) are in good agreement both qualitatively and quantitatively with the 20th century reanalysis product. Post-eruption shrinking of the HC rising branch is, however, more pronounced in HiRAM simulations than in 20CR and ERA-Interim reanalysis. This could be possible due to HiRAM having a much finer resolution compared to 20CR and ERA-INT. Moreover, it shares averaged anomaly produced using three ensemble members, which presumably minimizes the contribution introduced by internal variability. The model at 50 km resolution shows a comparable response to the reanalysis products. The rising branch of HC is, however, more compact in 25 km model resolution compared to reanalysis and 50 km model simulation, suggesting that HiRAM with fine resolution resolves HC feature better compared to its low-resolution counterpart and low-resolution reanalysis products. The location and intensity of the rising and sinking branch can also be seen from the overlay contour plots of meridional mass stream function following both eruptions (Figure 5.1) and these are consistent with vertical wind patterns. The intensities of the wind vectors (Figure 5.2) are comparable between HiRAM and the reanalysis products.

Global zonally averaged Omega (Pa/s, shaded) & Meridional Mass Stream Function ( $10^8$  Kg/sec, contours)

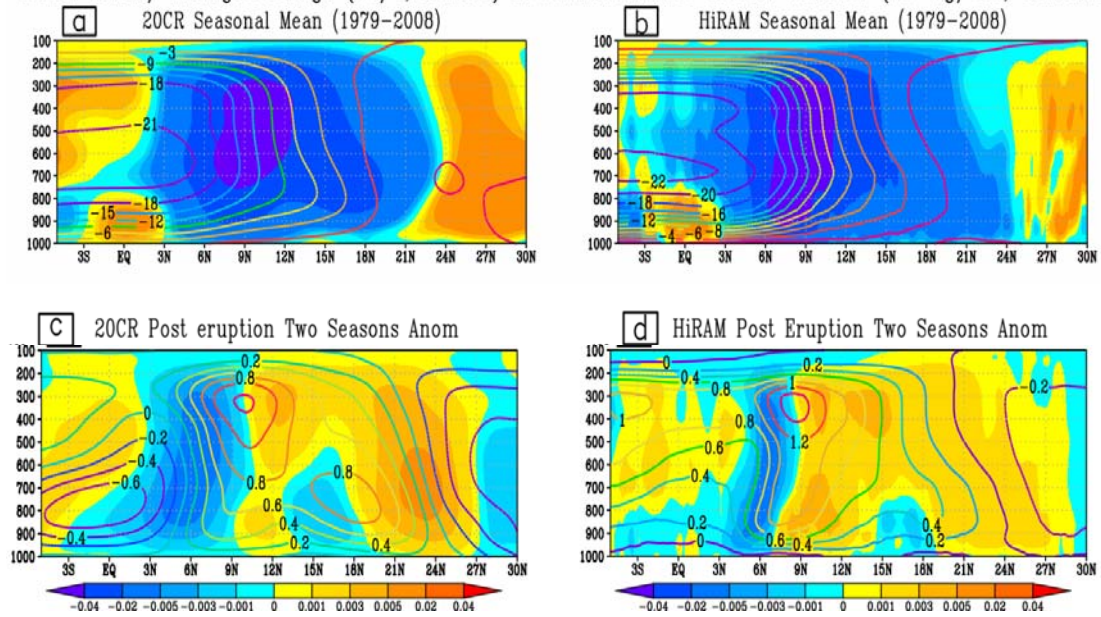


**Figure 5.1:** Zonal-mean omega (vertical velocity in shaded colors; Pa/s) and zonal-mean meridional mass stream function (in contours;  $10^8$  kg/s) mean pattern (a, b) calculated using 1979-2008 period and post-eruption two summer season averaged anomaly pattern following both the El Chichón and Pinatubo eruptions (c, d) from 20th century NOAA reanalysis (left) and HiRAM model at 25 km (right panel). The positive (negative) shaded values in color bar represent the sinking (rising) branch of HC.

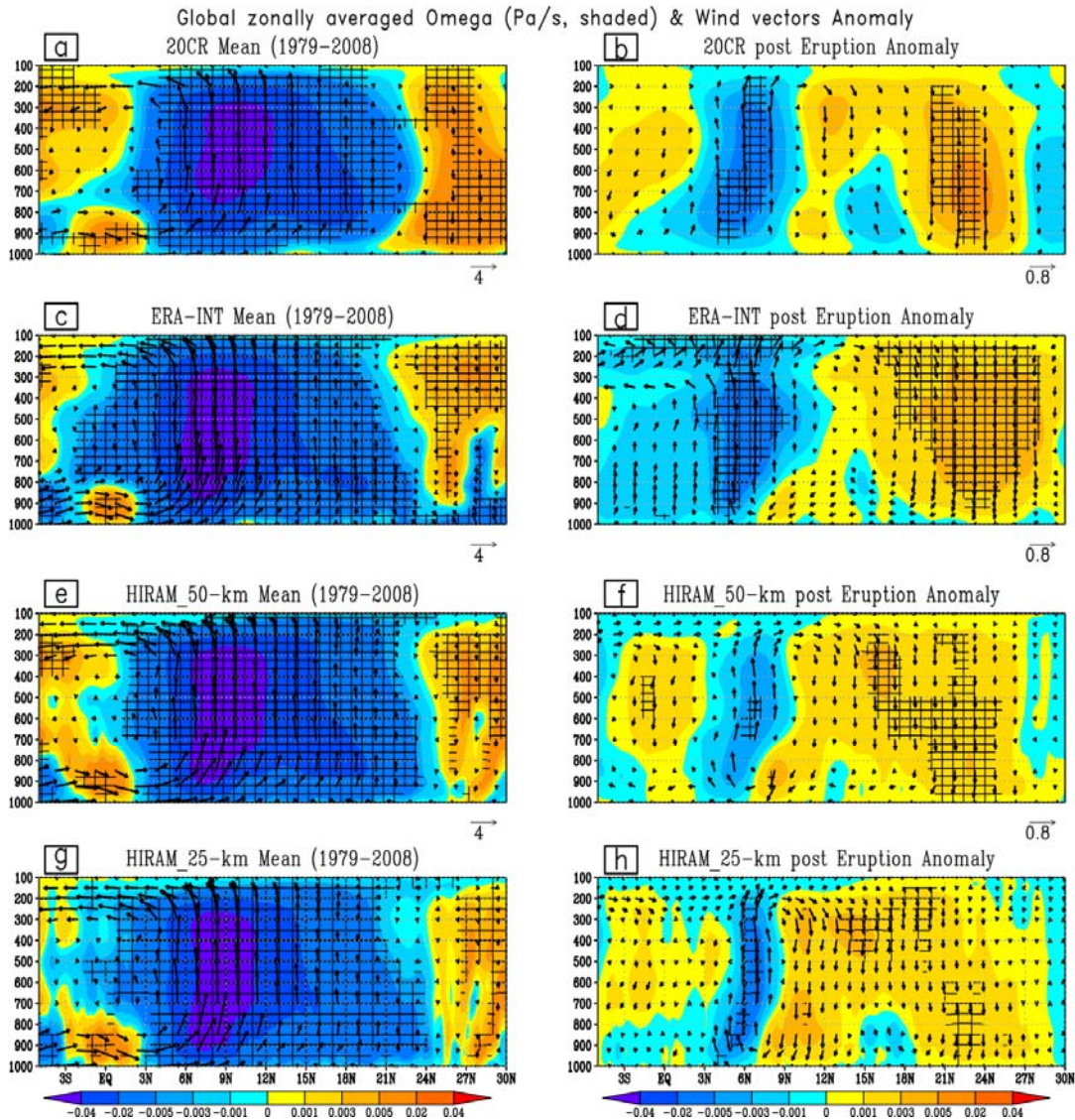


**Figure 5.2:** Mean (left panel) and anomaly (right panel) of zonal-mean Omega (vertical velocity in shaded colors; Pa/s) with overlaid zonal-mean wind vectors ( $v$ ;  $-100 \times \text{Omega}$ ) [m/s;  $100 \times \text{Pa/s}$ ] in the latitude-pressure plane. The mean pattern (calculated using the 1979-2008 period) is shown using a) 20CR, c) ERA-Interim, e) HiRAM at 50 km and g) HiRAM at 25 km and the post-eruption (following both the El Chichón and Pinatubo) two summer seasons averaged anomaly pattern is shown using b) 20CR, d) ERA-Interim, f) HiRAM at 50 km and h) HiRAM at 25 km. Positive shaded values in color bar represent sinking motion whereas negative values represent the rising branch of HC. Hatching shows the areas where the mean and anomaly pattern is significant at 95% confidence interval.

### 5.3.2. Midlatitude Jet Streams Response

To further understand the physical mechanism governing HC changes, I have looked at the zonally averaged zonal velocity (m/s) (Figure 5.3). Both the reanalysis and model results show an

equatorward movement of midlatitude jet streams. HiRAM (especially at 25 km) shows more pronounced features of equatorward displacement of subtropical jets in both the hemispheres, suggesting that volcanic-induced stratospheric and tropospheric thermal gradient could induce changes in zonal wind pattern that affect HC in an opposite way as is explained under global warming scenario (Seidel et al., 2008; Kang and Lu, 2012; Iles and Hegerl, 2014; Joseph and Zeng, 2011; Trenberth, 2011). Both the mean and anomalous patterns (Figure 5.3) of the jet streams are well simulated by HiRAM model.

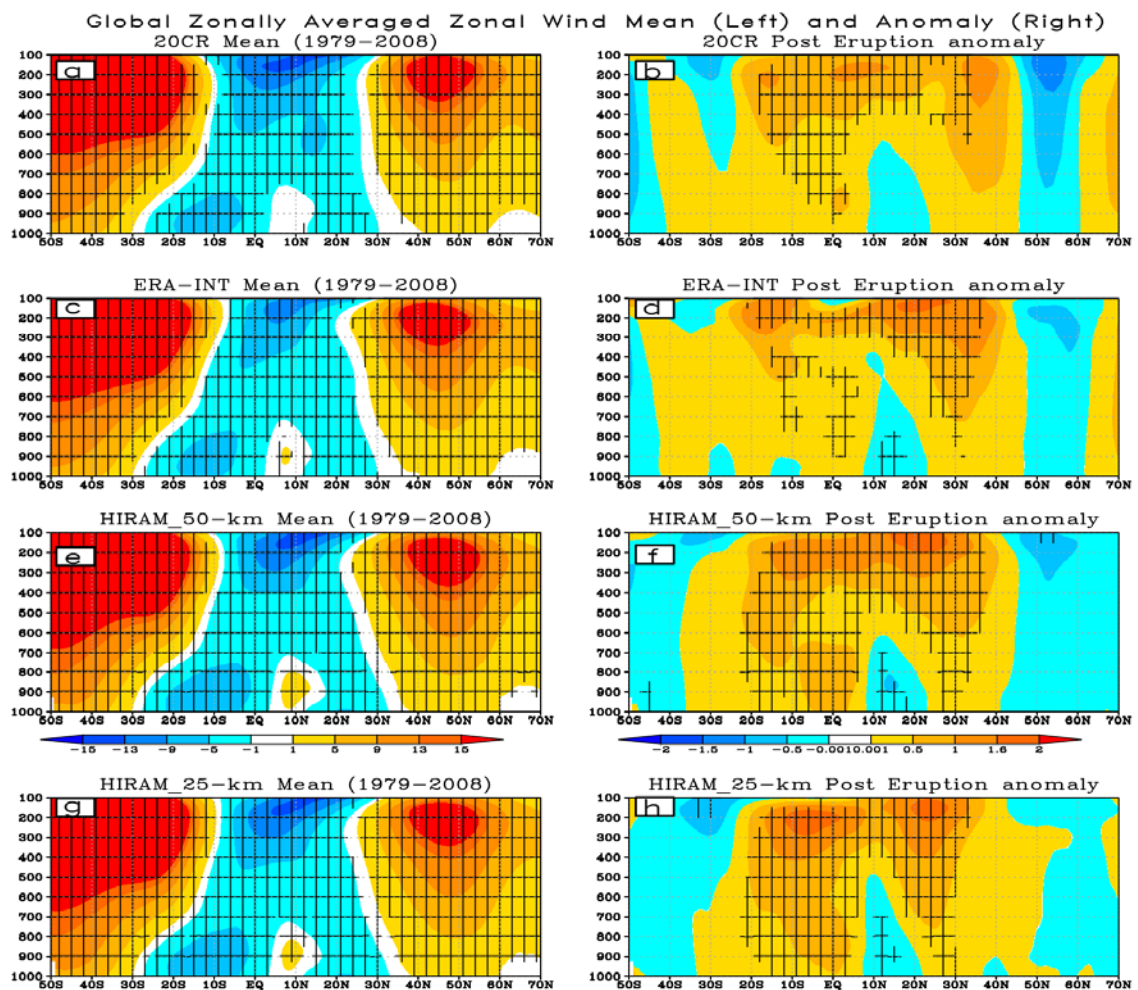


**Figure 5.3:** Global zonally averaged zonal wind (m/s) mean pattern using a) 20CR, c) ERA-Interim, e) HiRAM at 50 km, and g) HiRAM at 25 km and anomaly response (averaged for two summer seasons following both the eruptions) using b) 20CR, d) ERA-Interim, f) HiRAM at 50 km, and h) HiRAM at 25 km. Mean response is calculated using 1979-2008 period after excluding two summer seasons following both the eruptions and anomaly for both the eruptions is calculated using this mean. Hatching shows the areas where the mean and anomaly pattern is significant at 95% confidence interval.

### 5.3.3. Wind, Precipitation and Cloud Response

In this section, I am interested to see how the tropical eruptions affect African, and South Asian monsoonal circulation. Figure 5.4 displays wind vector seasonal mean (left panel) and anomalous responses at 850-hPa for post-eruption (right panel) periods over the African and South Asian regions employing 20CR, ERA-Interim and HiRAM (at 50 km and 25 km horizontal resolutions). Both the African and the Indian monsoon wind patterns show post-eruption (averaged over two seasons following both the El Chichón and the Pinatubo eruptions) weakening in the Indian and the African monsoons (Oman et al., 2006; Iles and Hegerl, 2014). The HiRAM model reproduces cross-equatorial monsoonal current and reversal of the wind (m/s) reasonably well both in the mean plot and anomaly patterns. The model simulation (at both resolutions) nicely captures the mean and post-eruption anomaly pattern of cross-equatorial low-level Somali Jets. Model generated wind anomalous responses show more pronounced weakening patterns both for Indian and African monsoon regions compared to 20CR and ERA-Interim, which show a slightly different pattern over the western part of the central African domain, that could be accounted for by coarse resolution of the reanalysis models together with scarcity of the observational measurements over the African domain. I also looked at post-eruption (averaged over both the El Chichón and Pinatubo eruptions) spatial pattern of precipitation anomaly over the Northern Hadley Cell region in summer season (Figure 5.5). A decreased precipitation anomaly both from the observations and the model is evident over the entire Hadley Cell with a slight increasing pattern over southern parts of India, Central Africa (southward of tropical Sahel rain belt region) and Bangladesh that could be attributed to the southward shift of the rising branch of Hadley Cell (Haywood et al., 2013; Joseph and Zeng, 2011; Oman et al., 2006). The precipitation decrease is caused as a result of weakening of the rising branch of HC (Figure 5.1 and Figure 5.2) and associated decreased cloud amount (Figure 5.6). Similar decreased cloud amount and associated precipitation changes over the tropical regions following high latitude as well as tropical eruptions were also reported in earlier studies (Oman et al., 2006; Joseph and Zeng, 2011). The pattern of precipitation anomaly and cloud amount, especially the low clouds (Figure 5.5 and Figure 5.6 respectively) suggest a weakening and southward shift of the ITCZ as a result of post-eruption weakened thermal gradient between the ocean and inland continents (Oman et al., 2006; Barnes and Polvani, 2013). HiRAM produced composited (averaged over two post-eruption summer seasons) precipitation anomaly pattern following both the eruptions (both at 50 km and 25 km resolutions) are in very good agreement (both qualitatively and quantitatively) with UDEL observations. However, model simulation at 25 km horizontal grid resolution shows more agreement with UDEL, especially over the African region. The precipitation decrease ranges

between -0.5 to -1.5 mm/day both in HiRAM simulations and UDEL observation, indicating drought-like conditions over the African and South Asian tropical convective regions. Figure 5.7 shows global and zonal averaged summer season precipitation anomaly averaged over a selected region (3°S-35°N) that covers mainly the Hadley Cell produced using 20CR and HiRAM simulation (at 25 km) after removing ENSO contribution through regression analysis, as previous studies suggest eliminating possible ENSO signal (Trenberth and Dai, 2007; Robock and Mao, 1995), as both the eruptions occurred at the times when there happened an ENSO event, which could be due to the volcano-induced modulation of ENSO. The ENSO-related contribution is filtered out from the total anomaly field using simple linear regression technique (see, e.g., Trenberth and Dai, 2007; Robock and Mao, 1995; Gujarati, 2009) by using Nino3.4 based SST index as input predictor for the summer season. The decreased precipitation anomaly is evident following both the eruptions, which shows a weakening of moisture inflow towards inland regions caused by weakening of hemispheric thermal gradient between land and ocean (Haywood et al., 2013). This decreased precipitation after both the eruption is consistent with earlier studies (Haywood et al., 2013; Joseph and Zeng, 2011). Both the HiRAM and 20CR product are in good agreement. This plot clearly shows that northern branch of Hadley Cell circulation is weakened as a result of weakened land-sea thermal contrast following both the eruptions that results in a decreased amount of water-laden air driven from ocean surface towards inland regions (Oman et al., 2006). Hence, a decreased inflow of moisture contents towards inland tropical regions results in decreased precipitation over the tropical convective regions in summer.

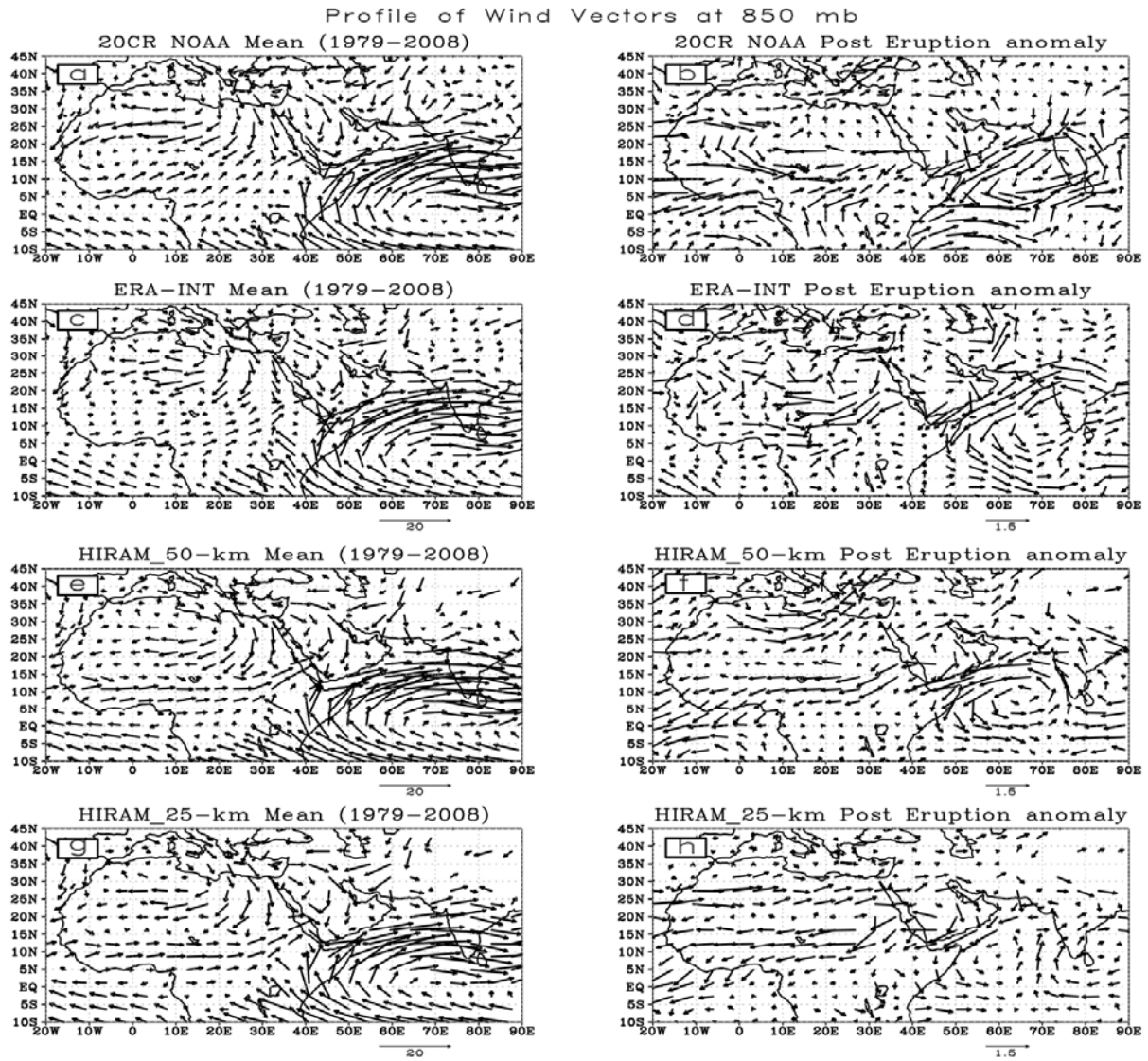


**Figure 5.4:** Summer (JJA) mean and post-eruption two summer seasons averaged wind vector (m/s) anomaly (composited for El Chichón and Pinatubo eruptions) from 20 CR (a, b), ERA-Interim (c, d) and HiRAM at 50 km (e, f) and 25 km (g, h) horizontal resolutions. The mean wind vector plots are computed over the 1979-2008 period after excluding two post-eruption summer seasons and anomaly is shown as a composite averaged over two summers following both the eruptions.

Precipitation anomaly composites (El-Chichon and Pinatubo)

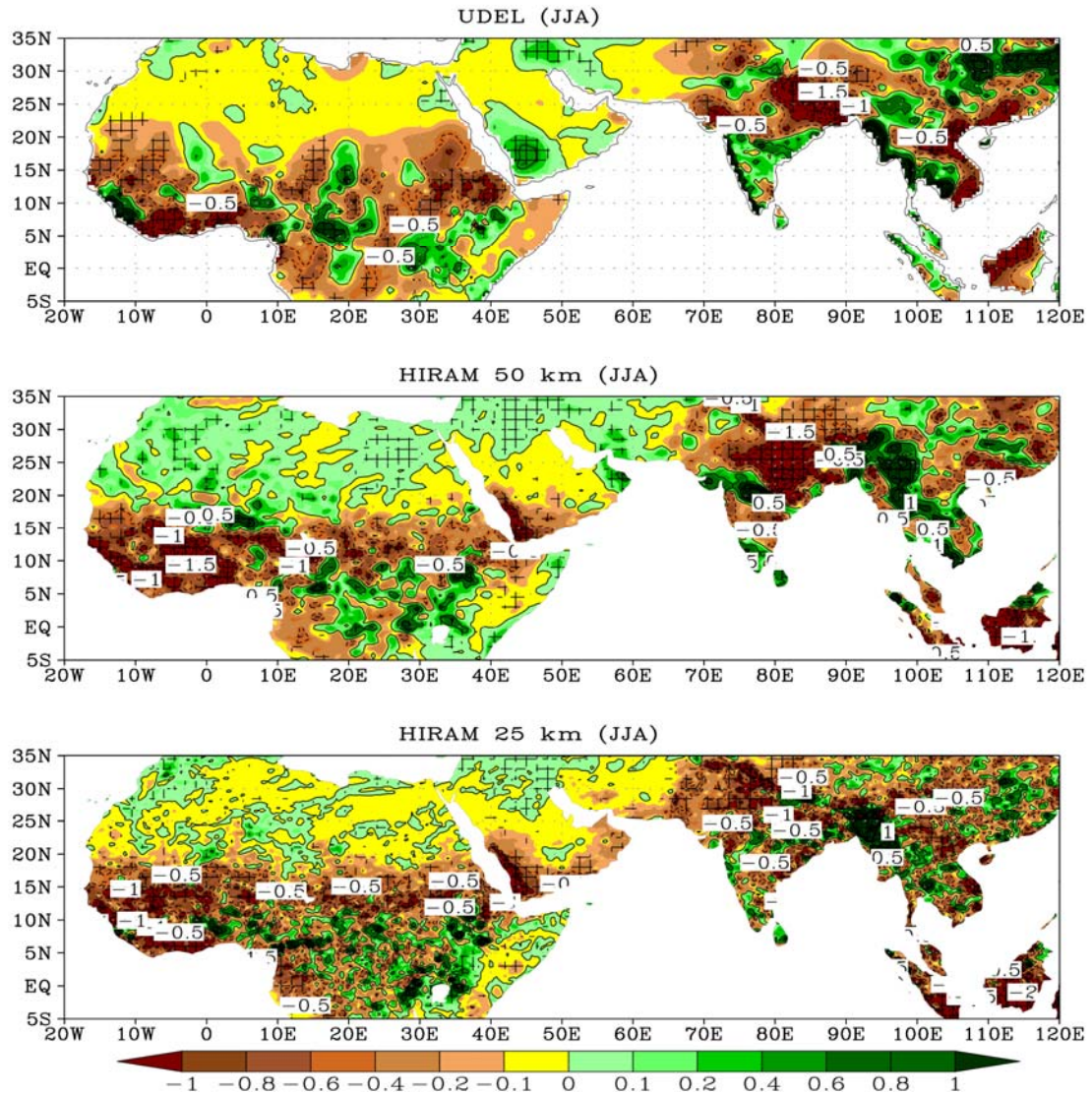


**Figure 5.5:** Composite precipitation anomaly (mm/d) for post-eruption (i.e., El Chichón and Pinatubo) two summer seasons using UDEL (top panel), HiRAM at 50 km (middle panel) and HiRAM at 25 km (bottom panel). Hatching shows the areas where the precipitation anomaly is significant at 95% confidence level.

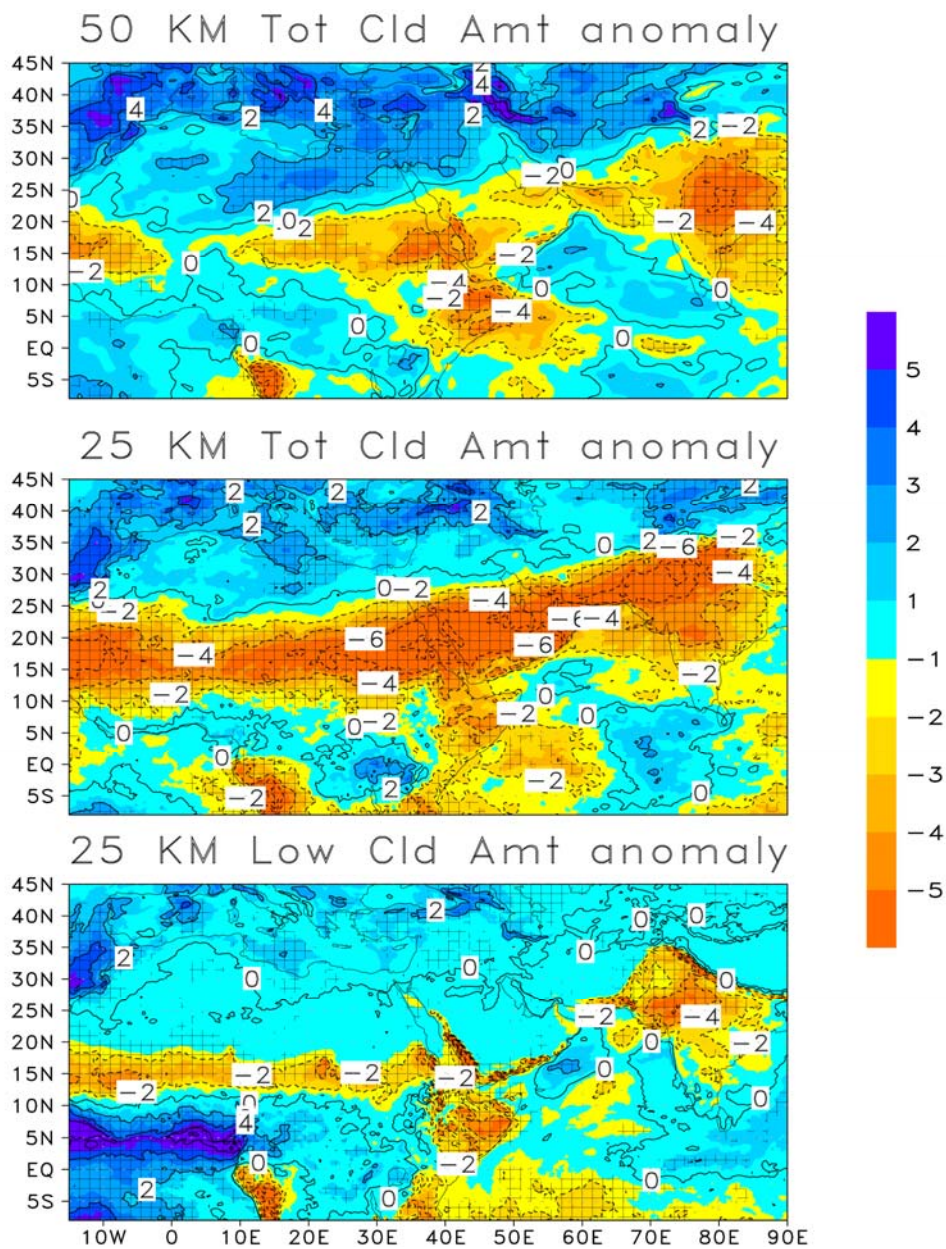


**Figure 5.6:** Total cloud contents anomaly (%) composite for post-eruption two summer seasons following El Chichón and Pinatubo eruptions using HiRAM at 50 km (top panel), at 25 km (middle panel) and low cloud contents anomaly using HiRAM at 25 km (bottom panel). Hatching shows the areas where the cloud contents anomaly is significant at 95% confidence level.

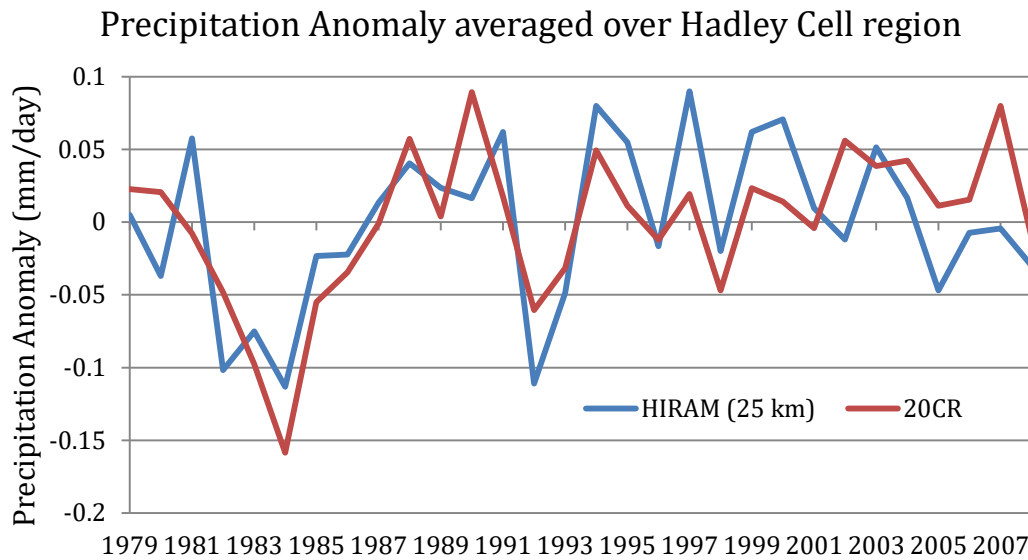


**Figure 5.7:** Summer (JJA) precipitation anomaly (mm/d), after removing ENSO contribution through simple linear regression using Nino3.4 index as input predictor, averaged over the Hadley Cell region (0-360° E, 3°S-35° N).

#### 5.4. Summary and Conclusions

The sensitivity of Hadley Cell to the warming induced by greenhouse forcing has widely been discussed in previous studies. However, Hadley Cell’s response to volcanic aerosol radiative forcing received less attention. In this study, I have analyzed the response of Northern Hemisphere Hadley Cell in post-eruption summer (JJA) season. For this purpose, I conducted simulations of the late 20th century explosive eruptions i.e., El-Chichón and Pinatubo, applying GFDL-HiRAM model effectively at 50 km and 25 km horizontal grid spacing. This high-resolution global modeling system is essential to better resolve post-eruption regional dynamic circulations (such as Asian and African summer monsoons) and their interaction and modulation by global-scale circulations (such as tropical Hadley and Walker circulations) that are important especially in the tropics. This study shows that the massive Northern Hemisphere tropical eruptions could significantly affect mid-latitude jet streams in the boreal summer season that in turn plays a significant role in contracting and displacing the updraft branch of Northern HC towards the equator. The observational and model-produced results further reveal that in the years following tropical eruptions significant surface cooling results into hemispheric thermal gradient as well as weakened land and ocean thermal contrast. This weakened thermal gradient leads to

decreased cloud amount and moisture inflow towards inland tropical convective regions in summer that result into a decreased precipitation, suggesting post-eruption drought-like conditions. HiRAM model effectively simulates a weakening of the NH summer Hadley Cell and a southward displacement of its rising branch (also called ITCZ) in the post-eruption summer season. However, I notice that HiRAM at 25 km horizontal resolution shows more pronounced displacement of mid-latitude jet streams and associated HC response compared to 20CR, ERA-Interim and HiRAM at 50 km resolution. My results clearly reveal that Northern HC circulation and ITCZ in the year following to the eruptions cause weakening in South Asian and African summer monsoon circulation system. The model results are largely consistent with the observations and the reanalysis products that suggest that GFDL-HiRAM can be used effectively to simulate post-eruption dynamic circulation changes. This study indicates that volcanic eruptions could significantly impact Hadley Cell circulation. However, further studies are needed to deepen our understanding of the impacts of volcanic eruptions on HC by using high-resolution coupled modeling approach to better account for post-eruption oceanic feedback and concomitant changes in HC.

It is worthwhile to mention that the anomaly of post-eruption years contains both the volcanic effect and the contribution of natural variability caused by ENSO, NAO and other possible drivers. Therefore, I analyzed the sensitivity of HC circulation to combined anomaly caused by volcanism and the circulations during four post-eruption seasons. I noticed in Chapter 4, that the magnitude of volcanic signal is larger than the signal coming through circulations. Moreover, a large number of studies (e.g., Maher et al., 2015; Pausata et al., 2015; Ohba et al., 2013; Predybaylo et al., 2017; Khodri et al., 2017; Stenchikov et al., 2002, Driscoll et al., 2012; Zambri et al., 2017; Timmreck, 2012; Fischer et al., 2007; Shindel et al., 2004) showed that the ENSO and NAO were forced to their positive phases by the strong volcanic eruptions, implying that the circulations, that happen at the time of eruption, could contain eruption signal. However, this requires further sensitivity experiments to accurately identify these mixed/interfering contributions of eruptions as well as circulations and their mixed interplay.

## **Chapter 6. Summary and Conclusions**

The climate of any region is mainly influenced by the external and internal climate forcing factors. ENSO, NAO, Indian monsoon circulations, and explosive volcanism are considered as important internal or external climate forcing factors that have pronounced global and regional climatic impacts. While ENSO, NAO and monsoon-induced climatic interactions have long been studied, the quantitative and qualitative understanding of the role of post-eruption circulation changes, e.g., ENSO, NAO and Indian monsoon changes and associated climatic impacts, especially at the regional scale is still rudimentary. Similarly, although volcanism is also largely discussed at global scale, their impacts at regional scale, especially, for the Middle East and North Africa (MENA) region are still less understood. This is partly because of the complexity of various dynamic processes involved and the uncertainties associated, and partly because of the lack of modeling and computational capabilities. The present dissertation investigates the direct volcanic radiative and indirect climatic impact (i.e., through circulation changes such as ENSO, NAO and Indian monsoon; see Section 4.4.4) during the time of El Chichón and Pinatubo eruptions on the MENA region, as this region appears to be very sensitive to volcanic radiative forcing. For this purpose, I used a very high-resolution global climate model, HiRAM developed at Geophysical Fluid Dynamics Laboratory (GFDL). In the following sections, the key findings of the dissertation are summarized and future research related to these topics is discussed.

### **6.1. Regional Climatic Impact of Volcanism over MENA**

It is well known that the Middle East climate experiences strong climatic changes following major equatorial explosive eruptions that far exceeded the effects expected from direct radiative forcing of volcanic aerosols. Volcanic-induced climatic impacts over the Middle East region has been generally discussed in previous studies, mostly as direct radiative effect; however, the sensitivity of this region to circulation changes following strong volcanic eruptions have not been explored in detail. This context motivated us to investigate the regional sensitivity of the Middle East and North Africa (MENA) climate to strong volcanism considering both direct radiative and circulation changes. Hence, to better quantify these effects, regional climate response to the El Chichón and Pinatubo volcanic eruptions in the MENA region is analyzed using GFDL global High-Resolution Atmospheric Model (HiRAM) with the effectively 25 km grid spacing. This high-resolution modeling technique ensures ample grid resolution for regional climate analysis with the ability to better account for global and regional responses to volcanic direct radiative and circulation impacts. The main findings of this study are summarized below.

- ENSO and NAO positive phases in the post-eruption years significantly cool the central parts of MENA, especially the Arabian Peninsula region. The positive phase of NAO produces strong cooling in winter over the entire MENA. The resultant direct and indirect (i.e., through circulation changes) winter cooling over the MENA region far exceeds the post-volcanic global mean cooling. The model underestimates the winter cooling response (both for ENSO and NAO); however, the overall pattern is well reproduced by the model. The impact of NAO in summer is small, as the correlation of NAO in summer is much weaker than its winter counterpart.
- The ENSO phase in post-eruption summers produces strong tropical warming and drying both in the model and observations. My results further reveal that the Indian monsoon also produces a strong impact over the MENA region, by impacting the MENA over the ITCZ and associated cloud distribution. A strengthening (weakening) of ISM results in strengthening (weakening) and associated increased (decreased) cloud distribution over MENA tropical rain belt region, resulting in increased (decreased) precipitation. A strengthening/weakening of ISM produces substantial temperature and precipitation changes over MENA, resulting in cooling/warming (wetting/drying) over MENA tropical rain belt regions, suggesting that ISM produces significant climatic impact over MENA tropics in summer. A decreased ISM in the post-eruption summers suggests a southward shift of ITCZ.
- Both the model and observational analysis show weakening, shrinking and equatorward displacement of the updraft branch of Hadley Cell in the post-eruption years caused by the equatorward shift of mid-latitude jets and hemispheric land-sea thermal gradient. As ITCZ is tightly-coupled to the rising branch of HC, the weakening and equatorward displacement of HC cause weakening of the ITCZ that adversely affects rainfall distribution in the monsoon fed regions, especially the South Asian, Middle Eastern and African tropical rain belt regions. The post-eruption distribution of cloud contents suggests a southward shift of the ITCZ.
- The conducted analysis sheds light on the internal mechanisms of MENA climate variability and helps to selectively diagnose the impact of leading teleconnection modes.

## 6.2. Future Research Work

This dissertation develops a sound understanding of the direct and indirect radiative impacts of tropical volcanic eruptions over the MENA region in the winter and summer seasons. In this study, a unified framework that combines the use of high-resolution modeling and multiple regression approach is developed. This study analyzes specifically designed climate model simulations to account for the regional impacts of tropical low-latitude eruptions. However, northern or southern high-latitude eruptions are also important. Past studies suggest that the high latitude eruptions could change the equator-to-pole temperature gradient and could influence the atmospheric general circulation (e.g., Oman et al. 2005; Kravitz and Robock 2011). Moreover, strong high-latitude eruptions also affect the Middle Eastern, African, Indian, and East Asian monsoon system (Thordarson and Self 2003). Therefore, the sensitivity of the MENA and South Asian regions to high latitude eruptions needs to be investigated.

Although in this study, I used a high-resolution atmospheric model, a high resolution coupled modeling approach is desired to better account for the oceanic feedback in modulating global and regional impacts of volcanism. Besides, I considered the major modes of climate variabilities (i.e., ENSO, NAO and Indian monsoon) that strongly affect the MENA region. However, there are few other modes that could potentially affect MENA climate, e.g., post-eruption phases of Indian Ocean Dipole (IOD) and quasi-biennial oscillation (QBO). Likewise, I analyzed the volcanism impact at the surface, while, the postvolcanic variations in the stratosphere and associated climatic impacts are also important. Keeping in mind such ideas, the research done as part of the current dissertation can be extended in the following directions.

- Conduct similar experiments using HiRAM for the study of high-latitude eruptions (both northern and southern) and their associated climatic impacts over MENA.
- Repeat the experiments in the present dissertation with a coupled fully dynamic ocean model or mixed layer model to quantify the role of SST feedback for better understanding of the volcanic forcing's direct and indirect climatic impacts and associated climate interactions, especially in the MENA region to answer how MENA climate could be modulated by volcanic-induced ocean-atmosphere feedbacks.
- Design experiments using coupled model to answer, how sensitive are global oceans to explosive volcanism and how ocean SST and subsurface ocean layers respond to volcanic-induced radiative changes?
- Further coupled model analyses are suggested to understand how the timing of the eruption influences the El Niño-like response and the link with the Indian and West

African monsoon. Moreover, additional sensitivity experiments using coupled models are suggested to better understand the similarities and differences of the climatic impact of classical/conventional ENSO and volcanic-induced ENSO on the MENA region (see, e.g., Khodri et al., 2017).

- The response of volcanism in stratosphere and associated quasi-biennial oscillation (QBO) response need to be studied. This research will highlight how QBO could affect the surface processes following explosive volcanism.
- A control simulation should be conducted with similar experimental design that is used in this dissertation but without including the volcanic aerosol forcing. The anomalies with respect to this control simulation need to be assessed. The results produced with this setup can be compared with the regression analysis approach that is used in the present study. This will help to better understand how effectively this regression-based anomaly approach performs compared to the anomalies produced using control experiments.

## References

1. Abualnaja, Y., V. P. Papadopoulos, S. A. Josey, I. Hoteit, H. Kontoyiannis, and Raitsos, D. E. (2015). Impacts of climate modes on air–sea heat exchange in the Red Sea. *Journal of Climate*, 28(7), 2665-2681.
2. Adames, Á. F., and Wallace, J. M. (2014). Three-dimensional structure and evolution of the MJO and its relation to the mean flow. *Journal of the Atmospheric Sciences*, 71(6), 2007-2026.
3. Adams, J. B., M. E. Mann, and Ammann, C. M. (2003). Proxy evidence for an El Niño-like response to volcanic forcing, *Nature*, 426(6964), 274-278.
4. Almazroui, M., Nazrul Islam, M., Athar, H., Jones, P. D., and Rahman, M. A. (2012). Recent climate change in the Arabian Peninsula: annual rainfall and temperature analysis of Saudi Arabia for 1978–2009. *International Journal of Climatology*, 32(6), 953-966.
5. Aiki, H., K. Takahashi, and Yamagata, T. (2006). The Red Sea outflow regulated by the Indian monsoon, *Continental Shelf Research*, 26(12), 1448-1468.
6. Anchukaitis, K. J., Buckley, B. M., Cook, E. R., Cook, B. I., D'Arrigo, R. D., and Ammann, C. M. (2010). Influence of volcanic eruptions on the climate of the Asian monsoon region. *Geophysical Research Letters*, 37(22).
7. Anderson, J. L., V. Balaji, Broccoli, A. J., and Cooke, W. F. (2004). The new GFDL global atmosphere and land model AM2-LM2: Evaluation with prescribed SST simulations. *Journal of Climate*, 17(24), 4641.
8. Ashok, K., Z. Guan, N. Saji, and Yamagata, T. (2004). Individual and combined influences of ENSO and the Indian Ocean dipole on the Indian summer monsoon. *Journal of Climate*, 17(16), 3141-3155.
9. Ashok, K., Behera, S. K., Rao, S. A., Weng, H., and Yamagata, T. (2007). El Niño Modoki and its possible teleconnection. *Journal of Geophysical Research: Oceans*, 112(C11).
10. Athar, H. (2014). Trends in observed extreme climate indices in Saudi Arabia during 1979–2008. *International Journal of Climatology*, 34(5), 1561-1574.
11. Athar, H. (2015). Teleconnections and variability in observed rainfall over Saudi Arabia during 1978–2010. *Atmospheric Science Letters*, 16(3), 373-379.
12. Athar, H., and Ammar, K. (2016). Seasonal characteristics of the large-scale moisture flux transport over the Arabian Peninsula, *Theoretical and Applied Climatology*, 124(3), 565-578, doi:10.1007/s00704-015-1437-7.

13. Atwater, M. A. (1970). Planetary albedo changes due to aerosols, *Science*, 170(3953), 64-66.
14. Bala, G., Duffy, P. B., and Taylor, K. E. (2008). Impact of geoengineering schemes on the global hydrological cycle. *Proceedings of the National Academy of Sciences*, 105(22), 7664-7669.
15. Barnes, E. A., and Polvani, L. (2013). Response of the midlatitude jets, and of their variability, to increased greenhouse gases in the CMIP5 models. *Journal of Climate*, 26(18), 7117-7135.
16. Barlow, M. A., and Tippett, M. K. (2008). Variability and predictability of central Asia river flows: Antecedent winter precipitation and large-scale teleconnections. *Journal of Hydrometeorology*, 9(6), 1334-1349.
17. Barlow, M., Cullen, H., and Lyon, B. (2002). Drought in central and southwest Asia: La Niña, the warm pool, and Indian Ocean precipitation. *Journal of Climate*, 15(7), 697-700.
18. Barlow, M., Wheeler, M., Lyon, B., and Cullen, H. (2005). Modulation of daily precipitation over southwest Asia by the Madden-Julian oscillation. *Monthly Weather Review*, 133(12), 3579-3594.
19. Barlow, M., Hoell, A., and Colby, F. (2007). Examining the wintertime response to tropical convection over the Indian Ocean by modifying convective heating in a full atmospheric model. *Geophysical Research Letters*, 34(19), L19702.
20. Barlow, M., Zaitchik, B., Paz, S., Black, E., Evans, J., and Hoell, A. (2016). A review of drought in the Middle East and southwest Asia. *Journal of Climate*, 29(23), 8547-8574.
21. Bladé, I., Liebmann, B., Fortuny, D., and van Oldenborgh, G. J. (2012). Observed and simulated impacts of the summer NAO in Europe: implications for projected drying in the Mediterranean region. *Climate Dynamics*, 39(3-4), 709-727.
22. Baldwin, M. P., and Dunkerton, T. J. (1999). Propagation of the Arctic Oscillation from the stratosphere to the troposphere. *Journal of Geophysical Research: Atmospheres*, 104(D24), 30937-30946.
23. Bangalath, H. K., and Stenchikov, G. (2015). Role of dust direct radiative effect on the tropical rain belt over Middle East and North Africa: A high-resolution AGCM study. *Journal of Geophysical Research: Atmospheres*, 120(10), 4564-4584.
24. Bangalath, H. K., and Stenchikov, G. (2016). Sensitivity of the Middle East-North African Tropical Rainbelt to Dust Shortwave Absorption: A High-Resolution AGCM Experiment. *Journal of Climate*, 29(19), 7103-7126.
25. Baran, A. J., and Foot, J. S. (1994). New application of the operational sounder HIRS in

- determining a climatology of sulphuric acid aerosol from the Pinatubo eruption. *Journal of Geophysical Research: Atmospheres*, 99(D12), 25673-25679.
26. Barnes, J. E., and Hofmann, D. J. (1997). Lidar measurements of stratospheric aerosol over Mauna Loa Observatory. *Geophysical Research Letters*, 24(15), 1923-1926.
  27. Bretherton, C. S., McCaa, J. R., and Grenier, H. (2004). A new parameterization for shallow cumulus convection and its application to marine subtropical cloud-topped boundary layers. Part I: Description and 1D results. *Monthly Weather Review*, 132(4), 864-882.
  28. Brönnimann, S., Franke, J., Nussbaumer, S. U., Zumbühl, H. J., Steiner, D., Trachsel, M., Hegerl, G.C., Schurer, A., Worni, M., Malik, A. and Flückiger, J. (2019). Last phase of the Little Ice Age forced by volcanic eruptions. *Nature Geoscience*, 12(8), 650-656.
  29. Bui, H. X., Yu, J. Y., and Chou, C. (2019). Impacts of model spatial resolution on the vertical structure of convection in the tropics. *Climate Dynamics*, 52(1-2), 15-27.
  30. Bourke, W. (1974). A multi-level spectral model. I. Formulation and hemispheric integrations. *Monthly Weather Review*, 102(10), 687-701.
  31. Boyle, J., and Klein, S. A. (2010). Impact of horizontal resolution on climate model forecasts of tropical precipitation and diabatic heating for the TWP-ICE period. *Journal of Geophysical Research: Atmospheres*, 115(D23).
  32. Chakraborty A, Behera SK, Mujumdar M, Ohba R, Yamagata, T. (2006) Diagnosis of tropospheric moisture over Saudi Arabia and influences of IOD and ENSO. *Monthly Weather Review*, 134, 598–617.
  33. Camberlin, P., B. Fontaine, S. Louvet, P. Oettli, and P. Valimba (2010). Climate adjustments over Africa accompanying the Indian monsoon onset. *Journal of Climate*, 23(8), 2047-2064.
  34. Church, J. A., White, N. J., and Arblaster, J. M. (2005). Significant decadal-scale impact of volcanic eruptions on sea level and ocean heat content, *Nature*, 438(7064), 74-77.
  35. Church, J. A., N. J. White, R. Coleman, K. Lambeck, and J. X. Mitrovica (2004). Estimates of the regional distribution of sea level rise over the 1950–2000 period. *Journal of Climate*, 17(13), 2609-2625.
  36. Compo, G. P., Whitaker, J. S., Sardeshmukh, P. D., Matsui, N., Allan, R. J., Yin, X., Gleason, B.E., Vose, R.S., Rutledge, G., Bessemoulin, P. and Brönnimann, S. (2011). The twentieth century reanalysis project. *Quarterly Journal of the Royal Meteorological Society*, 137(654), 1-28.

37. Cook, K. H. (2004). Hadley circulation dynamics. In *The Hadley circulation: present, past and future* (pp. 61-83). Springer, Dordrecht.
38. Crutzen, P. J. (2006). Albedo enhancement by stratospheric sulfur injections: a contribution to resolve a policy dilemma?, *Climatic Change*, 77(3), 211-220.
39. Cullen, H. M., A. Kaplan, P. A. Arkin, and P. B. Demenocal (2002). Impact of the North Atlantic Oscillation on Middle Eastern climate and streamflow, *Climatic Change*, 55(3), 315-338.
40. Croitoru, A. E., and Piticar, A. (2013). Changes in daily extreme temperatures in the extra-Carpathians regions of Romania. *International Journal of Climatology*, 33(8), 1987-2001.
41. Davis, S. M., and Rosenlof, K. H. (2012). A multidiagnostic intercomparison of tropical-width time series using reanalyses and satellite observations. *Journal of Climate*, 25(4), 1061-1078.
42. del Río, S., Anjum Iqbal, M., Cano-Ortiz, A., Herrero, L., Hassan, A., and Penas, A. (2013). Recent mean temperature trends in Pakistan and links with teleconnection patterns. *International Journal of Climatology*, 33(2), 277-290.
43. D'Arrigo, R., Wilson, R., and Tudhope, A. (2009). The impact of volcanic forcing on tropical temperatures during the past four centuries. *Nature Geoscience*, 2(1), 51.
44. Dee, D. P., Uppala, S. M., Simmons, A. J., Berrisford, P., Poli, P., Kobayashi, S., Andrae, U., Balmaseda, M.A., Balsamo, G., Bauer, D.P. and Bechtold, P. (2011). The ERA-Interim reanalysis: Configuration and performance of the data assimilation system. *Quarterly Journal of the Royal Meteorological Society*, 137(656), 553-597.
45. Driscoll, S., Bozzo, A., Gray, L. J., Robock, A., and Stenchikov, G. (2012). Coupled Model Intercomparison Project 5 (CMIP5) simulations of climate following volcanic eruptions. *Journal of Geophysical Research: Atmospheres*, 117(D17).
46. Dogar, M. M., Kucharski, F., and Azharuddin, S. (2017). Study of the global and regional climatic impacts of ENSO magnitude using SPEEDY AGCM. *Journal of Earth System Science*, 126(2), 30.
47. Dogar, M. M., Kucharski, F., Sato, T., Mehmood, S., Ali, S., Gong, Z., Das, D., and Arraut, J. (2019). Towards understanding the global and regional climatic impacts of Modoki magnitude. *Global and Planetary Change*, 172, 223-241.
48. Dutton, E. G., and Christy, J. R. (1992). Solar radiative forcing at selected locations and evidence for global lower tropospheric cooling following the eruptions of El Chichón and Pinatubo. *Geophysical Research Letters*, 19(23), 2313-2316.

49. Efron, B., and R. J. Tibshirani (1994). An introduction to the bootstrap, Vol. 57. Champan & Hall/CRC press, New York and London.
50. Emile-Geay, J., Seager, R., Cane, M. A., Cook, E. R., and Haug, G. H. (2008). Volcanoes and ENSO over the past millennium. *Journal of Climate*, 21(13), 3134-3148.
51. Eyring, V., Butchart, N., Waugh, D.W., Akiyoshi, H., Austin, J., Bekki, S., Bodeker, G.E., Boville, B.A., Brühl, C., Chipperfield, M.P. and Cordero, E. (2006). Assessment of temperature, trace species, and ozone in chemistry-climate model simulations of the recent past. *Journal of Geophysical Research: Atmospheres*, 111(D22), 1-29.
52. Fischer, E. M., J. Luterbacher, E. Zorita, S. F. B. Tett, C. Casty, and Wanner H. (2007). European climate response to tropical volcanic eruptions over the last half millennium. *Geophysical Research Letters*, 34(L05707), 1-6.
53. Flaounas, E., Janicot, S., Bastin, S., Roca, R. and Mohino, E. (2012). The role of the Indian monsoon onset in the West African monsoon onset: observations and AGCM nudged simulations. *Climate Dynamics*, 38(5-6), 965-983.
54. Forsyth, P. (1988). In the wake of Etna, 44 BC, *Classical Antiquity*, 7(1), 49-57.
55. Franklin, B. (1784), *Meteorological imaginations and conjectures*. Manchester Literary and Philosophical Society Memoirs and Proceedings, 2(122), 357–361.
56. Freidenreich, S. M., and V. Ramaswamy, (1999). A new multiple-band solar radiative parameterization for general circulation models. *Journal of Geophysical Research*, 104, 31389-31409.
57. Fu, Q. and Lin, P. (2011). Poleward shift of subtropical jets inferred from satellite-observed lower-stratospheric temperatures. *Journal of Climate*, 24(21), 5597-5603.
58. Fujiwara, M., Hibino, T., Mehta, S. K., Gray, L., Mitchell, D. and Anstey, J. (2015). Global temperature response to the major volcanic eruptions in multiple reanalysis data sets. *Atmospheric Chemistry and Physics*, 15(23), 13507-13518.
59. Fyfe, J. C., Von Salzen, K., Cole, J.N.S., Gillett, N. P. and Vernier, J. P. (2013). Surface response to stratospheric aerosol changes in a coupled atmosphere–ocean model. *Geophysical Research Letters*, 40(3), 584-588.
60. Feng, J. and Li, J. (2013). Contrasting impacts of two types of ENSO on the boreal spring Hadley circulation. *Journal of Climate*, 26(13), 4773-4789.
61. Fu, Q., Johanson, C. M., Wallace, J. M. and Reichler, T. (2006). Enhanced mid-latitude tropospheric warming in satellite measurements. *Science*, 312(5777), 1179-1179.

62. Gastineau, G., Li, L. and Le Treut, H. (2009). The Hadley and Walker circulation changes in global warming conditions described by idealized atmospheric simulations. *Journal of Climate*, 22(14), 3993-4013.
63. Gnanadesikan, A., Dixon, K.W., Griffies, S.M., Balaji, V., Barreiro, M., Beesley, J.A., Cooke, W.F., Delworth, T.L., Gerdes, R., Harrison, M.J. and Held, I.M. (2006). GFDL's CM2 global coupled climate models. Part II: The baseline ocean simulation. *Journal of Climate*, 19(5), 675-697.
64. Gu, G., Adler, R.F., Huffman, G.J. and Curtis, S. (2007). Tropical rainfall variability on interannual-to-interdecadal and longer time scales derived from the GPCP monthly product. *Journal of Climate*, 20(15), 4033-4046.
65. Giannini, A., Biasutti, M., and Verstraete, M. M. (2008). A climate model-based review of drought in the Sahel: Desertification, the re-greening and climate change. *Global and Planetary Change*, 64(3-4), 119-128.
66. Genin, A., Lazar, B. and Brenner, S. (1995). Vertical mixing and coral death in the Red Sea following the eruption of Mount Pinatubo. *Nature*, 377(6549), 507-510.
67. Ginoux, P., Horowitz, L.W., Ramaswamy, V., Geogdzhayev, I.V., Holben, B.N., Stenchikov, G. and Tie, X. (2006). Evaluation of aerosol distribution and optical depth in the Geophysical Fluid Dynamics Laboratory coupled model CM2. 1 for present climate. *Journal of Geophysical Research: Atmospheres*, 111(D22).
68. Graf, H.-F. (1992). Arctic radiation deficit and climate variability, *Climate Dynamics*, 7(1), 19-28.
69. Graft, H.F., Kirchner, I., Robock, A. and Schult, I. (1993). Pinatubo eruption winter climate effects: Model versus observations. *Climate Dynamics*, 9(2), 81-93.
70. Graf, H., Perlwitz, J. and Kirchner, I. (1994). Northern Hemisphere tropospheric mid-latitude circulation after violent volcanic eruptions. *Contributions to Atmospheric Physics*, 67(1), 3-13.
71. Groisman, P. Y. (1992). Possible regional climate consequences of the Pinatubo eruption: An empirical approach. *Geophysical Research Letters*, 19, 1603-1606.
72. Gujarati, D. N. (2009). *Basic econometrics*, Tata McGraw-Hill Education.
73. Handler, P. (1984). Possible association of stratospheric aerosols and El Niño type events. *Geophysical Research Letters*, 11:1121-1124
74. Hansen, J., D. Johnson, A. Lacis, S. Lebedeff, P. Lee, D. Rind, and G. Russell (1981). Climate impact of increasing atmospheric carbon dioxide, *Science*, 213(4511), 957-966.

75. Hansen, J., Ruedy, R., Sato, M. and Lo, K. (2010). Global surface temperature change. *Reviews of Geophysics*, 48(4).
76. Hansen, J., Lacis, A., Ruedy, R. and Sato, M., 1992. Potential climate impact of Mount Pinatubo eruption. *Geophysical Research Letters*, 19(2), 215-218.
77. Hansen, J., Sato, M., and Ruedy, R. (1997). Radiative forcing and climate response. *Journal of Geophysical Research: Atmospheres*, 102(D6), 6831-6864.
78. Hansen, J., Sato, M.K.I., Ruedy, R., Nazarenko, L., Lacis, A., Schmidt, G.A., Russell, G., Aleinov, I., Bauer, M., Bauer, S. and Bell, N. (2005). Efficacy of climate forcings. *Journal of Geophysical Research: Atmospheres*, 110(D18), 1-45.
79. Harris, L. M., Lin, S. J., and Tu, C. (2016). High-resolution climate simulations using GFDL HiRAM with a stretched global grid. *Journal of Climate*, 29(11), 4293–4314.
80. Hatzianastassiou, N., C. Matsoukas, E. Drakakis, P. Stackhouse Jr, P. Koepke, A. Fotiadi, K. Pavlakis, and I. Vardavas (2007). The direct effect of aerosols on solar radiation based on satellite observations, reanalysis datasets, and spectral aerosol optical properties from Global Aerosol Data Set (GADS), *Atmospheric Chemistry and Physics*, 7(10), 2585-2599.
81. Haywood, J. M., A. Jones, N. Bellouin, and D. and Stephenson (2013). Asymmetric forcing from stratospheric aerosols impacts Sahelian rainfall, *Nature Climate Change*, 3, 660-665, doi:10.1038/nclimate1857.
82. Hoell, A., and Funk, C. (2013). The ENSO-related west Pacific sea surface temperature gradient. *Journal of Climate*, 26(23), 9545-9562.
83. Hoell, A., Barlow, M., and Saini, R. (2012). The leading pattern of intraseasonal and interannual Indian Ocean precipitation variability and its relationship with Asian circulation during the boreal cold season. *Journal of Climate*, 25(21), 7509-7526.
84. Hoell, A., Funk, C., and Barlow, M. (2014a). The regional forcing of Northern hemisphere drought during recent warm tropical west Pacific Ocean La Niña events. *Climate Dynamics*, 42(11-12), 3289-3311.
85. Hoell, A., Funk, C., and Barlow, M. (2014b). La Niña diversity and northwest Indian Ocean rim teleconnections. *Climate Dynamics*, 43(9-10), 2707-2724.
86. Horowitz, L. W., S. Walters, D. L. Mauzerall, L. K. Emmons, P. J. Rasch, C. Granier, X. Tie, J. F. Lamarque, M. G. Schultz, and G. S. Tyndall (2003). A global simulation of tropospheric ozone and related tracers: Description and evaluation of MOZART, version 2. *Journal of Geophysical Research: Atmospheres*, 108(D24), 1-25.
87. Hu, Y., Huang, H., and Zhou, C. (2018). Widening and weakening of the Hadley

- circulation under global warming. *Science Bulletin*, 63(10), 640-644.
88. Hudson, R. D., Andrade, M. F., Follette, M. B., and Frolov, A. D. (2006). The total ozone field separated into meteorological regimes—Part II: Northern Hemisphere mid-latitude total ozone trends. *Atmospheric Chemistry and Physics*, 6, 5183–5191.
  89. Hurrell, J. W., and Deser, C. (2010). North Atlantic climate variability: the role of the North Atlantic Oscillation. *Journal of Marine Systems*, 79(3), 231-244.
  90. Hurrell, J. W. (1995). Decadal trends in the North Atlantic Oscillation: regional temperatures and precipitation, *Science*, 269(5224), 676-679.
  91. Hurrell, J. W., Kushnir, Y., Ottersen, G., and Visbeck, M. (2003). An overview of the North Atlantic oscillation, *The North Atlantic Oscillation: climatic significance and environmental impact*. Geophysical Monograph-American Geophysical Union, 134, 1-35.
  92. Held, I., and Soden, B. (2006). Robust response of the hydrological cycle to global warming. *Journal of Climate*, 19, 5686–5699.
  93. Iles, C., and Hegerl, G. (2017). Role of the North Atlantic Oscillation in decadal temperature trends, *Environmental Research Letters*, 12(11), 114010.
  94. Iles, C. E., and Hegerl, G. C. (2014). The global precipitation response to volcanic eruptions in the CMIP5 models. *Environmental Research Letters*, 9(10), 104012.
  95. Iles, C. E., Hegerl, G. C., Schurer, A. P., and Zhang, X. (2013). The effect of volcanic eruptions on global precipitation. *Journal of Geophysical Research: Atmosphere*, 118, 8770–8786.
  96. Iqbal, M., S. Hameed, and Khan, F. (2013). Influence of Azores high pressure on Middle Eastern rainfall, *Theoretical and Applied Climatology*, 111(1-2), 211-221.
  97. Johanson, C. M., and Fu, Q. (2009). Hadley cell widening: Model simulations versus observations. *Journal of Climate*, 22(10), 2713-2725.
  98. Joseph, R., and Zeng, N. (2011). Seasonally modulated tropical drought induced by volcanic aerosol. *Journal of Climate*, 24(8), 2045-2060.
  99. Josey, S. A., S. Somot, and Tsimplis, M. (2011). Impacts of atmospheric modes of variability on Mediterranean Sea surface heat exchange. *Journal of Geophysical Research: Oceans*, 116(C2), 1-15
  100. Kang, S. M., and Lu, J. (2012). Expansion of the Hadley cell under global warming: Winter versus summer. *Journal of Climate*, 25(24), 8387-8393.
  101. Kelly, P. M., Jones, P., and Jia, P. (1996). The spatial response of the climate system to explosive volcanic eruptions. *International Journal of Climatology*, 16(5), 537-550.
  102. Khodri, M., Izumo, T., Vialard, J., Janicot, S., Cassou, C., Lengaigne, M., Mignot, J.,

- Gastineau, G., Guilyardi, E., Lebas, N., and Robock, A. (2017). Tropical explosive volcanic eruptions can trigger El Niño by cooling tropical Africa. *Nature Communications*, 8(1), 778.
103. Kirchner, I., Stenchikov, G. L., Graf, H. F., Robock, A., and Antuña, J. C. (1999). Climate model simulation of winter warming and summer cooling following the 1991 Mount Pinatubo volcanic eruption. *Journal of Geophysical Research: Atmospheres*, 104(D16), 19039-19055.
104. Krishna, L. V. (2014). Long term temperature trends in four different climatic zones of Saudi Arabia. *International Journal of Applied Science and Technology*, 4(5), 233-242.
105. Kravitz, B., Robock, A., and Bourassa, A. (2010). Negligible climatic effects from the 2008 Okmok and Kasatochi volcanic eruptions. *Journal of Geophysical Research: Atmospheres*, 115(D2), 1-16.
106. Kravitz, B., and Robock, A. (2011). Climate effects of high-latitude volcanic eruptions: Role of the time of year. *Journal of Geophysical Research*, 116(D01105), 1-16.
107. Kremser, S., Thomason, L.W., von Hobe, M., Hermann, M., Deshler, T., Timmreck, C., Toohey, M., Stenke, A., Schwarz, J.P., Weigel, R. and Fueglistaler, S. (2016). Stratospheric aerosol—Observations, processes, and impact on climate. *Reviews of Geophysics*, 54(2), 278-335.
108. Krichak, S., Kishcha, P., and Alpert, P. (2002). Decadal trends of main Eurasian oscillations and the Eastern Mediterranean precipitation, *Theoretical and Applied Climatology*, 72(3-4), 209-220.
109. Kodera, K. (1994). Influence of volcanic eruptions on the troposphere through stratospheric dynamical processes in the Northern Hemisphere winter. *Journal of Geophysical Research*, 99, 1273–1282.
110. Kodera, K., and Chiba, M. (1995). Tropospheric circulation changes associated with stratospheric sudden warmings: A case study. *Journal of Geophysical Research: Atmospheres*, 100(D6), 11055-11068.
111. Laakso, A., Kokkola, H., Partanen, A. I., Niemeier, U., Timmreck, C., Lehtinen, K. E. J., Hakkarainen, H., and Korhonen, H. (2016). Radiative and climate impacts of a large volcanic eruption during stratospheric sulfur geoengineering, *Atmospheric Chemistry and Physics*, 16(1), 305-323, doi:10.5194/acp-16-305-2016.
112. Labitzke, K., and McCormick, M. (1992). Stratospheric temperature increases due to Pinatubo aerosols. *Geophysical Research Letters*, 19(2), 207-210.

113. Lamb, H. H. (1970). Volcanic dust in the atmosphere; with a chronology and assessment of its meteorological significance, *Philosophical Transactions of the Royal Society of London. Series A, Mathematical and Physical Sciences*, 266(1178), 425-533.
114. Legates, D. R., and Willmott, C. J. (1990). Mean seasonal and spatial variability in gauge-corrected, global precipitation. *International Journal of Climatology*, 10(2), 111-127.
115. Lim, Y.-K. (2015). The East Atlantic/West Russia (EA/WR) teleconnection in the North Atlantic: climate impact and relation to Rossby wave propagation, *Climate Dynamics*, 44(11-12), 3211-3222.
116. Lindzen, R. S., and Pan, W. (1994). A note on orbital control of equator-pole heat fluxes. *Climate Dynamics*, 10(1-2), 49-57.
117. Liu, F., Chai, J., Wang, B., Liu, J., Zhang, X., and Wang, Z. (2016). Global monsoon precipitation responses to large volcanic eruptions, *Scientific Reports*, 6 (1), 1-11.
118. Liu, H. W., Yu, J. Y., and Chen, C. A. (2018). Changes of tropical precipitation and convective structure under global warming projected by CMIP5 model simulations. *Terrestrial, Atmospheric & Oceanic Sciences*, 29(4), 429-440
119. Lean, J. L., and Rind, D. H. (2008). How natural and anthropogenic influences alter global and regional surface temperatures: 1889 to 2006. *Geophysical Research Letters*, 35(18), 1-6.
120. Lau, N. C., and Ploshay, J. J. (2009). Simulation of synoptic-and subsynoptic-scale phenomena associated with the East Asian summer monsoon using a high-resolution GCM. *Monthly Weather Review*, 137(1), 137-160.
121. Maher, McGregor, N., S., England, M. H., and Gupta, A. S. (2015). Effects of volcanism on tropical variability. *Geophysical Research Letters*, 42(14), 6024-6033.
122. McCracken, M., and Luther, F. (1984). Preliminary estimate of the radiative and climatic effects of the El Chichón eruption. *Geofisica Internacional*, 23-3, 385-401.
123. Malyshev, S., Shevliakova, E., Stouffer, R. J., and Pacala, S. W. (2015). Contrasting local versus regional effects of land-use-change-induced heterogeneity on historical climate: analysis with the GFDL earth system model. *Journal of Climate*, 28(13), 5448-5469.
124. Mariotti, A. (2007). How ENSO impacts precipitation in southwest central Asia. *Geophysical Research Letters*, 34(16), L16706
125. Mariotti, A., Zeng, N., and Lau, K. M. (2002). Euro-Mediterranean rainfall and ENSO—a seasonally varying relationship. *Geophysical Research Letters*, 29(12), 59-1.

126. Mariotti, A., Ballabrera-Poy, J., and Zeng, N. (2005). Tropical influence on Euro-Asian autumn rainfall variability. *Climate Dynamics*, 24(5), 511-521.
127. Mann, M. E., M. A. Cane, S. E. Zebiak, and A. Clement (2005). Volcanic and solar forcing of the tropical Pacific over the past 1000 years. *Journal of Climate*, 18(3), 447-456.
128. Man, W., Zhou, T., and Jungclauss, J. H. (2014). Effects of large volcanic eruptions on global summer climate and East Asian monsoon changes during the last millennium: Analysis of MPI-ESM simulations. *Journal of Climate*, 27(19), 7394-7409.
129. Mass, C. F., and Portman, D. A. (1989). Major volcanic eruptions and climate: A critical evaluation. *Journal of Climate*, 2(6), 566-593.
130. McGregor, S., Timmermann, A., Timm, O. (2010). A unified proxy for ENSO and PDO variability since 1650. *Climate of the Past*, 6, 1–17
131. Meehl, G. A., Washington, W. M., Wigley, T., Arblaster, J. M., and Dai, A. (2003). Solar and greenhouse gas forcing and climate response in the twentieth century. *Journal of Climate*, 16(3), 426-444.
132. Meehl, G. A., Arblaster, J. M., Branstator, G., and van Loon, H. (2008). A coupled air-sea response mechanism to solar forcing in the Pacific region. *Journal of Climate*, 21(12), 2883-2897.
133. Meehl, G. A., Hu, A., and Santer, B. D. (2009). The mid-1970s climate shift in the Pacific and the relative roles of forced versus inherent decadal variability. *Journal of Climate*, 22(3), 780-792.
134. Minnis, P., Harrison, E., Stowe, L., Gibson, G., Denn, F., Doelling, D., and Smith, W. (1993). Radiative climate forcing by the Mount Pinatubo eruption, *Science*, 259(5100), 1411-1415.
135. Mitchell, J. M. (1961). Recent secular changes of global temperature, *Annals of the New York Academy of Sciences*, 95(1), 235-250.
136. Mitchell Jr, J. M. (1971). The effect of atmospheric aerosols on climate with special reference to temperature near the earth's surface. *Journal of Applied Meteorology*, 10(4), 703-714.
137. Moorthi, S., and Suarez, M. J. (1992). Relaxed Arakawa-Schubert. A parameterization of moist convection for general circulation models. *Monthly Weather Review*, 120(6), 978-1002.
138. Morak, S., Hegerl, G. C., and Christidis, N. (2013). Detectable changes in the frequency of temperature extremes. *Journal of Climate*, 26(5), 1561-1574.

139. McCormick, M. P., Thomason, L. W., and Trepte, C. R. (1995). Atmospheric effects of the Mt Pinatubo eruption. *Nature*, 373(6513), 399.
140. Mignot, J., Khodri, M., Frankignoul, C., and Servonnat. (2011). Volcanic impact on the Atlantic Ocean over the last millennium, *Climate of the Past*, 1439-1455.
141. Milly, P., and Shmakin, A. (2002). Global modeling of land water and energy balances. Part I: The land dynamics (LaD) model. *Journal of Hydrometeorology*, 3(3), 283-299.
142. Nguyen, H., Evans, A., Lucas, C., Smith, I., and Timbal, B. (2013). The Hadley circulation in reanalyses: Climatology, variability, and change. *Journal of Climate*, 26(10), 3357-3376.
143. Ohba, M., Shiogama, H., Yokohata, T., and Watanabe, M. (2013). Impact of strong tropical volcanic eruptions on ENSO simulated in a coupled GCM. *Journal of Climate*, 26, 5169–5182.
144. Oman, L., Robock, A., Stenchikov, G., Schmidt, G. A., and Ruedy, R. (2005). Climatic response to high-latitude volcanic eruptions. *Journal of Geophysical Research*, 110(D13103), doi:10.1029/2004JD005487.
145. Oman, L., Robock, A., Stenchikov, G. L., and Thordarson, T., (2006). High-latitude eruptions cast shadow over the African monsoon and the flow of the Nile. *Geophysical Research Letters*, 33, doi:10.1029/2006GL027665.
146. Oort, A. H., and Yienger, J. J. (1996). Observed interannual variability in the Hadley circulation and its connection to ENSO. *Journal of Climate*, 9(11), 2751-2767.
147. Osipov, S. and Stenchikov, G. (2017). Regional effects of the Mount Pinatubo eruption on the Middle East and the Red Sea. *Journal of Geophysical Research: Oceans*, 122(11), 8894-8912.
148. Otterå, O. H. (2008). Simulating the effects of the 1991 Mount Pinatubo volcanic eruption using the ARPEGE atmosphere general circulation model. *Advances in Atmospheric Sciences*, 25(2), 213-226.
149. Papadopoulos, V. P., Abualnaja, Y., Josey, S. A., Bower, A., Raitzos, D. E., Kontoyiannis, H., and Hoteit, I. (2013). Atmospheric forcing of the winter air–sea heat fluxes over the northern Red Sea. *Journal of Climate*, 26(5), 1685-1701.
150. Pausata, F. S., Chafik, L., Caballero, R., and Battisti D. S. (2015). Impacts of high-latitude volcanic eruptions on ENSO and AMOC, *Proceedings of the National Academy of Sciences*, 112(45), 13784-13788.
151. Pausata, F. S., Grini, A., Caballero, R., Hannachi, A., and Seland, Ø. (2015). High-latitude volcanic eruptions in the Norwegian Earth System Model: the effect of different

- initial conditions and of the ensemble size. *Tellus B: Chemical and Physical Meteorology*, 67(1), 26728.
152. Pausata, F. S., Karamperidou, C., Caballero, R., and Battisti, D. S. (2016). ENSO response to high-latitude volcanic eruptions in the Northern Hemisphere: The role of the initial conditions. *Geophysical Research Letters*, 43(16), 8694-8702.
153. Parthasarathy, B. (1995). Monthly and seasonal rainfall series for all India, homogeneous regions and meteorological subdivisions: 1871-1994. Indian Institute of Tropical Meteorology Research Report.
154. Parthasarathy, B., Munot, A., and Kothawale, D. (1994). All-India monthly and seasonal rainfall series: 1871–1993, *Theoretical and Applied Climatology*, 49(4), 217-224.
155. Parthasarathy, B., Kumar, K. R., and Munot, A. A. (1991). Evidence of secular variations in Indian monsoon rainfall–circulation relationships. *Journal of Climate*, 4(9), 927-938.
156. Parthasarathy, B., Kumar, K. R., and Kothawale, D. R. (1992). Indian summer monsoon rainfall indices: 1871-1990. *Meteorological Magazine*, 121(1441), 174-186.
157. Palmer, M. D., McNeall, D. J., and Dunstone, N. J. (2011). Importance of the deep ocean for estimating decadal changes in Earth's radiation balance. *Geophysical Research Letters*, 38(13).
158. Peng, Y., Shen, C., Wang, W. C., and Xu, Y. (2010). Response of summer precipitation over Eastern China to large volcanic eruptions. *Journal of Climate*, 23(3), 818-824.
159. Penner, A., and Binyamin, J. (2013). Climate change associated with global teleconnections, volcanic eruptions, and the Arctic's snow-ice albedo in Godthab, Greenland. *Atmospheric and Climate Sciences*, 3(01), 31.
160. Peterson, T. C., Vose, R., Schmoyer, R., and Razuvaev, V. (1998). Global Historical Climatology Network (GHCN) quality control of monthly temperature data. *International Journal of Climatology*, 18(11), 1169-1179.
161. Polvani, L. M., and Kushner, P. J. (2002). Tropospheric response to stratospheric perturbations in a relatively simple general circulation model. *Geophysical Research Letters*, 29(7), 1-4.
162. Polvani, L. M., Waugh, D. W., Correa, G. J., and Son, S. W. (2011). Stratospheric ozone depletion: The main driver of twentieth-century atmospheric circulation changes in the Southern Hemisphere. *Journal of Climate*, 24(3), 795-812.
163. Portman, D. A., and Gutzler, D. S. (1996). Explosive volcanic eruptions, the El Niño-Southern Oscillation, and US climate variability. *Journal of Climate*, 9(1), 17-33.

164. Predybaylo, E., Stenchikov, G. L., Wittenberg, A. T., and Zeng, F. (2017). Impacts of a Pinatubo - size volcanic eruption on ENSO. *Journal of Geophysical Research: Atmospheres*, 122(2), 925-947.
165. Preethi, B., Sabin, T., Adedoyin, J., and Ashok, K. (2015). Impacts of the ENSO Modoki and other Tropical Indo-Pacific Climate-Drivers on African Rainfall, *Scientific Reports*, 5, 16653.
166. Putman, W. M., and Lin, S. J. (2007). Finite-volume transport on various cubed-sphere grids. *Journal of Computational Physics*, 227(1), 55-78.
167. Quan, X. W., Diaz, H.F., and Hoerling, M. P. (2004). Change of the tropical Hadley cell since 1950, in the Hadley Circulation: Past, Present, and Future. *Advances in Global Change Research*, Springer, Dordrecht, 21, 85-120.
168. Read, W., Froidevaux, L., and Waters, J. (1993). Microwave limb sounder measurement of stratospheric SO<sub>2</sub> from the Mt. Pinatubo Volcano. *Geophysical Research Letters*, 20(12), 1299-1302.
169. Ramachandran, S., Ramaswamy, V., Stenchikov, G. L., and Robock, A. (2000). Radiative impact of the Mount Pinatubo volcanic eruption: Lower stratospheric response. *Journal of Geophysical Research: Atmospheres*, 105(D19), 24409-24429.
170. Randel, W. J. (2010). Variability and trends in stratospheric temperature and water vapor, *The Stratosphere: Dynamics, Transport and Chemistry*, Geophysical Monograph Series, 190, 123-135.
171. Rayner, N., Parker, D. E., Horton, E., Folland, C., Alexander, L., Rowell, D., Kent, E., and Kaplan, A. (2003). Global analyses of sea surface temperature, sea ice, and night marine air temperature since the late nineteenth century. *Journal of Geophysical Research*, 108(D14), 4407, doi:10.1029/2002JD002670.
172. Rind, D., Perlwitz, J., and Lonergan, P. (2005). AO/NAO response to climate change: 1. Respective influences of stratospheric and tropospheric climate changes. *Journal of Geophysical Research: Atmospheres* (1984–2012), 110(D12), 1-15.
173. Robock, A., and Mao, J. (1992). Winter warming from large volcanic eruptions. *Geophysical Research Letters*, 19(24), 2405-2408.
174. Robock, A., and Y. Liu (1994). The volcanic signal in Goddard Institute for Space Studies three-dimensional model simulations. *Journal of Climate*, 7(1), 44-55.
175. Robock, A., and J. Mao (1995). The volcanic signal in surface temperature observations. *Journal of Climate*, 8(5), 1086-1103.
176. Robock, A. (2000). Volcanic eruption and Climate. *Reviews of Geophysics* 38, 191-219.

177. Robock, A. (2001). Stratospheric forcing needed for dynamical seasonal prediction, *Bulletin of the American Meteorological Society*, 82(10), 2189-2192.
178. Robock, A. (2002). The climatic aftermath, *Science*, 295(5558), 1242-1244.
179. Robock, A. (2003). Introduction: Mount Pinatubo as a test of climate feedback mechanisms, *Volcanism and the Earth's atmosphere*, 1-8.
180. Robock, A., L. Oman, and Stenchikov, G. L. (2008). Regional climate responses to geoengineering with tropical and Arctic SO<sub>2</sub> injections. *Journal of Geophysical Research: Atmospheres*, 113(D16), 1-15.
181. Rodwell, M. J., and Hoskins, B. J. (1996). Monsoons and the dynamics of deserts, *Quarterly Journal of the Royal Meteorological Society*, 122(534), 1385-1404.
182. Ropelewski, C. F., and Halpert, M. S. (1986). North American precipitation and temperature patterns associated with the El Niño/Southern Oscillation (ENSO). *Monthly Weather Review*, 114(12), 2352-2362.
183. Saha, S., S. Moorthi, H.-L. Pan, X. Wu, J. Wang, S. Nadiga, P. Tripp, R. Kistler, J. Woollen, and D. Behringer (2010). The NCEP climate forecast system reanalysis, *Bulletin of the American Meteorological Society*, 91(8), 1015-1057.
184. Santer, B. D., et al. (2001). Accounting for the effect of volcanoes and ENSO in comparisons of modeled and observed temperature trends. *Journal of Geophysical Research*, 106, 28,033–28,059, doi:10.1029/2000JD000189.
185. Santer, B. D., Wigley, T., Boyle, J., Gaffen, D. J., Hnilo, J., Nychka, D., Parker, E., and Taylor, K. E. (2000). Statistical significance of trends and trend differences in layer-average atmospheric temperature time series. *Journal of Geophysical Research*, 105(D6), 7337–7356. <https://doi.org/10.1029/1999JD901105>.
186. Santer, B. D., Bonfils, C., Painter, J. F., Zelinka, M. D., Mears, C., Solomon, S., Schmidt, G. A., Fyfe, J. C., Cole, J. N., and Nazarenko, L. (2014). Volcanic contribution to decadal changes in tropospheric temperature, *Nature Geoscience*, 7(3), 185-189.
187. Sato, M., Hansen, J. E., McCormick, M. P., and Pollack, J. B. (1993). Stratospheric aerosol optical depths, 1850–1990. *Journal of Geophysical Research: Atmospheres*, 98(D12), 22987-22994.
188. Schmidt, H., K. Alterskjær, D. Bou Karam, O. Boucher, A. Jones, J. Kristjánsson, U. Niemeier, M. Schulz, Aaheim, A., and Benduhn, F. (2012). Solar irradiance reduction to counteract radiative forcing from a quadrupling of CO<sub>2</sub>: climate responses simulated by four earth system models, *Earth System Dynamics*, 3, 63-78.
189. Schwarzkopf, M. D., and Ramaswamy, V. (1999). Radiative effects of CH<sub>4</sub>, N<sub>2</sub>O,

- halocarbons and the foreign-broadened H<sub>2</sub>O continuum: A GCM experiment. *Journal of Geophysical Research: Atmospheres* (1984–2012), 104(D8), 9467-9488.
190. Schneider, D. P., Ammann, C. M., Otto-Bliesner, B. L., and Kaufman, D. S. (2009). Climate response to large, high-latitude and low-latitude volcanic eruptions in the Community Climate System Model. *Journal of Geophysical Research: Atmospheres*, 114(D15), 1-21.
191. Seidel, D. J., Fu, Q., Randel, W. J., and Reichler, T. J. (2008). Widening of the tropical belt in a changing climate. *Nature Geoscience*, 1(1), 21-24.
192. Seidel, D. J., and Randel, W. J. (2007). Recent widening of the tropical belt: Evidence from tropopause observations. *Journal of Geophysical Research: Atmospheres*, 112(D20), 1-6.
193. Shaheen, R., Abauanza, M., Jackson, T. L., McCabe, J., Savarino, J., and Thiemens, M. H. (2013). Tales of volcanoes and El-Niño southern oscillations with the oxygen isotope anomaly of sulfate aerosol. *Proceedings of the National Academy of Sciences*, 110(44), 17662-17667.
194. Shindell, D. T., G. A. Schmidt, Miller, R. L., and Rind, D. (2001). Northern Hemisphere winter climate response to greenhouse gas, ozone, solar, and volcanic forcing. *Journal of Geophysical Research: Atmospheres* (1984–2012), 106(D7), 7193-7210.
195. Shindell, D. T., Schmidt, G. A., Mann, M. E., and Faluvegi, G. (2004). Dynamic winter climate response to large tropical volcanic eruptions since 1600. *Journal of Geophysical Research: Atmospheres*, 109(D5).
196. Shukla, J. (1975). Effect of Arabian sea-surface temperature anomaly on Indian summer monsoon: A numerical experiment with the GFDL model. *Journal of the Atmospheric Sciences*, 32(3), 503-511.
197. Sigurdsson, H. (1982). Volcanic pollution and climate: the 1783 Laki eruption. *Eos, Transactions American Geophysical Union*, 63(32), 601-602.
198. Simkin, T. (1993). Terrestrial volcanism in space and time. *Annual Review of Earth and Planetary Sciences*, 21(1), 427-452.
199. Simpson, I. R., Seager, R., Shaw, T. A., and Ting, M. (2015). Mediterranean summer climate and the importance of Middle East topography. *Journal of Climate*, 28(5), 1977-1996.
200. Soden, B. J., Wetherald, R. T., Stenchikov, G. L., and Robock, A. (2002). Global cooling after the eruption of Mount Pinatubo: A test of climate feedback by water vapor. *Science*, 296(5568), 727-730.

201. Stenchikov, G. L., Kirchner, I., Robock, A., Graf, H. F., Antuna, J. C., Grainger, R., Lambert, A., and Thomason, L. (1998). Radiative forcing from the 1991 Mount Pinatubo volcanic eruption. *Journal of Geophysical Research: Atmospheres* (1984–2012), 103(D12), 13837-13857.
202. Stenchikov, G., Hamilton, K., Stouffer, R. J., Robock, A., Ramaswamy, V., Santer, B., and Graf, H. F. (2006). Arctic Oscillation response to volcanic eruptions in the IPCC AR4 climate models. *Journal of Geophysical Research: Atmospheres*, 111(D7).
203. Stenchikov, G., Robock, A., Ramaswamy, V., Schwarzkopf, M. D., Hamilton, K., and Ramachandran, S. (2002). Arctic Oscillation response to the 1991 Mount Pinatubo eruption: Effects of volcanic aerosols and ozone depletion. *Journal of Geophysical Research*, 107(D24). doi: 10.1029/2002JD002090.
204. Stenchikov, G., T. L. Delworth, Ramaswamy, V., Stouffer, R. J., Wittenberg, A., and Zeng, F. (2009). Volcanic signals in oceans. *Journal of Geophysical Research*, 114(D16104), doi:10.1029/2008JD011673.
205. Stenchikov, G. (2009). Chapter 4—The role of volcanic activity in climate and global change, in *Climate Change: Observed Impacts on Planet*, edited by T. M. Letcher, pp. 77–102, Elsevier, Amsterdam.
206. Sultan, B., and Janicot, S. (2000). Abrupt shift of the ITCZ over West Africa and intra-seasonal variability. *Geophysical Research Letters*, 27(20), 3353-3356, doi:10.1029/1999GL011285.
207. Saha, S., Moorthi, S., Pan, H.-L., Wu, X., Wang, J., Nadiga, S., Tripp, P., Kistler, R., Woollen, J., and Behringer, D. (2010). The NCEP climate forecast system reanalysis, *Bulletin of the American Meteorological Society*, 91(8), 1015-1057.
208. Singh, P., Chowdary, J. S., and Gnanaseelan, C. (2013). Impact of prolonged La Niña events on the Indian Ocean with a special emphasis on southwest Tropical Indian Ocean SST. *Global and Planetary Change*, 100, 28-37.
209. Seager, R., Harnik, N., Kushnir, Y., Robinson, W., and Miller, J. (2003). Mechanisms of hemispherically symmetric climate variability. *Journal of Climate*, 16(18), 2960-2978.
210. Smith, T. M., Reynolds, R. W., Peterson, T. C., and Lawrimore, J. (2008). Improvements to NOAA's historical merged land–ocean surface temperature analysis (1880–2006). *Journal of Climate*, 21(10), 2283-2296.
211. Sterl, A., van Oldenborgh, G. J., Hazeleger, W., and Burgers, G. (2007). On the robustness of ENSO teleconnections. *Climate Dynamics*, 29(5), 469-485.

212. Schwendike, J., Govekar, P., Reeder, M. J., Wardle, R., Berry, G. J., and Jakob, C. (2014). Local partitioning of the overturning circulation in the tropics and the connection to the Hadley and Walker circulations. *Journal of Geophysical Research: Atmospheres*, 119(3), 1322-1339.
213. Tao, L., Hu, Y., and Liu, J. (2016). Anthropogenic forcing on the Hadley circulation in CMIP5 simulations. *Climate Dynamics*, 46(9-10), 3337-3350.
214. Timmreck, C., H.-F. Graf, D. Zanchettin, S. Hagemann, T. Kleinen, and K. Krüger (2012). Climate response to the Toba super-eruption: Regional changes, *Quaternary International*, 258, 30-44.
215. Trenberth, K. E., G. W. Branstator, D. Karoly, A. Kumar, Lau, N. C., and Ropelewski, C. (1998). Progress during TOGA in understanding and modeling global teleconnections associated with tropical sea surface temperatures. *Journal of Geophysical Research: Oceans*, 103(C7), 14291-14324.
216. Trenberth, K. E., and Caron, J. M. (2000). The Southern Oscillation revisited: Sea level pressures, surface temperatures, and precipitation. *Journal of Climate*, 13(24), 4358-4365.
217. Trenberth, K. E. (2011). Changes in precipitation with climate change. *Climate Research*, 47(1-2), 123-138.
218. Trenberth, K. E., and Dai, A. (2007). Effects of Mount Pinatubo volcanic eruption on the hydrological cycle as an analog of geoengineering. *Geophysical Research Letters*, 34, L15702, doi:10.1029/2007GL030524.
219. Timmermann, A., Oberhuber, J., Bacher, A., Esch, M., Latif, M., and Roeckner, E. (1999). Increased El Niño frequency in a climate model forced by future greenhouse warming. *Nature*, 398(6729), 694.
220. Tandon, N. F., Gerber, E. P., Sobel, A. H., and Polvani, L. M. (2013). Understanding Hadley cell expansion versus contraction: Insights from simplified models and implications for recent observations. *Journal of Climate*, 26(12), 4304-4321.
221. Thompson, D. W., and Wallace, J. M. (1998). The Arctic Oscillation signature in the wintertime geopotential height and temperature fields. *Geophysical Research Letters*, 25(9), 1297-1300.
222. Thompson, D. W., and Wallace, J. M. (2000). Annular modes in the extratropical circulation. Part I: month-to-month variability. *Journal of Climate*, 13(5), 1000-1016.

223. Thompson, D. W., J. M. Wallace, P. D. Jones, and J. J. Kennedy (2009). Identifying signatures of natural climate variability in time series of global-mean surface temperature: Methodology and insights. *Journal of Climate*, 22(22), 6120-6141.
224. Thordarson, T., and Self, S. (2003). Atmospheric and environmental effects of the 1783–1784 Laki eruption: A review and reassessment. *Journal of Geophysical Research: Atmospheres*, 108(D1), AAC-7.
225. Timmreck, C. (2012). Modeling the climatic effects of large explosive volcanic eruptions. *Wiley Interdisciplinary Reviews: Climate Chang*, 3(6), 545–564. doi: 10.1002/wcc.192
226. Timmermann, A., J. Oberhuber, A. Bacher, M. Esch, M. Latif, and E. Roeckner (1999). Increased El Niño frequency in a climate model forced by future greenhouse warming, *Nature*, 398(6729), 694-697.
227. Turco, R., R. Whitten, and O. Toon (1982), Stratospheric aerosols: Observation and theory, *Reviews of Geophysics*, 20(2), 233-279.
228. van Loon, H., and Rogers, J. C. (1978). The seesaw in winter temperatures between Greenland and northern Europe. Part I: General description, *Monthly Weather Review*, 106(3), 296-310.
229. van Loon, H., Meehl, G. A., and Shea, D. J. (2007). Coupled air-sea response to solar forcing in the Pacific region during northern winter. *Journal of Geophysical Research: Atmospheres*, 112(D2), 1-8.
230. van Loon, H., Meehl, G. A., and Arblaster, J. M. (2004). A decadal solar effect in the tropics in July–August. *Journal of Atmospheric and Solar-Terrestrial Physics*, 66(18), 1767-1778.
231. van Loon, H., and Meehl, G. A. (2008). The response in the Pacific to the sun’s decadal peaks and contrasts to cold events in the Southern Oscillation. *Journal of Atmospheric and Solar-Terrestrial Physics*, 70, 1046–1055.
232. Vecchi, G. A., and Soden, B. J. (2007). Global warming and the weakening of the tropical circulation. *Journal of Climate*, 20(17), 4316-4340.
233. VINOJ, V., Rasch, P. J., Wang, H., Yoon, J. H., Ma, P. L., Landu, K., & Singh, B. (2014). Short-term modulation of Indian summer monsoon rainfall by West Asian dust. *Nature Geoscience*, 7(4), 308-313.
234. Wild, M., Grieser, J., and Schär, C. (2008). Combined surface solar brightening and increasing greenhouse effect support recent intensification of the global land-based hydrological cycle. *Geophysical Research Letters*, 35(17), 1-5.

235. Wilson, R., Cook, E., D'Arrigo, R., Riedwyl, N., Evans, M. N., Tudhope, A., and Allan, R. (2010). Reconstructing ENSO: the influence of method, proxy data, climate forcing and teleconnections. *Journal of Quaternary Science*, 25(1), 62-78.
236. Wittenberg, A. T., Rosati, A., Lau, N. C., and Ploshay, J. J. (2006). GFDL's CM2 global coupled climate models. Part III: Tropical Pacific climate and ENSO. *Journal of Climate*, 19(5), 698-722.
237. Wallace, J. M., and Gutzler, D. S. (1981), Teleconnections in the geopotential height field during the Northern Hemisphere winter, *Monthly Weather Review*, 109(4), 784-812.
238. Wegmann, M., Brönnimann, S., Bhend, J., Franke, J., Folini, D., Wild, M., and Luterbacher, J. (2014). Volcanic Influence on European Summer Precipitation through Monsoons: Possible Cause for “Years without Summer. *Journal of Climate*, 27(10), 3683-3691.
239. Wang, C. (2002). Atmospheric circulation cells associated with the El Niño–Southern Oscillation. *Journal of Climate*, 15(4), 399-419.
240. Wanner, H., Brönnimann, S., Casty, C., Gyalistras, D., Luterbacher, J., Schmutz, C., Stephenson, D. B., and Xoplaki, E. (2001). North Atlantic Oscillation—concepts and studies, *Surveys in Geophysics*, 22(4), 321-381.
241. Webster, P. J., The elementary Hadley circulation, in *The Hadley Circulation: Present, Past and Future*, edited by H. F. Diaz and R. S., 2004, Bradley, pp. 9–60, Springer, New York.
242. Wilcox, L. J., Hoskins, B. J., and Shine, K. P. (2012). A global blended tropopause based on ERA data. Part II: Trends and tropical broadening. *Quarterly Journal of the Royal Meteorological Society*, 138(664), 576-584.
243. Wu, R., and Kirtman, B. P. (2005). Roles of Indian and Pacific Ocean air–sea coupling in tropical atmospheric variability. *Climate Dynamics*, 25(2-3), 155-170.
244. Xie, S. P., Deser, C., Vecchi, G. A., Ma, J., Teng, H., and Wittenberg, A. T. (2010). Global warming pattern formation: Sea surface temperature and rainfall. *Journal of Climate*, 23(4), 966-986.
245. Xu, K.-M. (2006). Using the bootstrap method for a statistical significance test of differences between summary histograms, *Monthly Weather Review*, 134(5), 1442-1453.
246. Yoshioka, M., Mahowald, N. M., Conley, A. J., Zender, C. S., Coleman, D. B. (2007). Impact of Desert Dust Radiative Forcing on Sahel Precipitation: Relative Importance of

- Dust Compared to Sea Surface Temperature Variations, Vegetation Changes, and Greenhouse Gas Warming. *Journal of Climate*, 20, 1445-1467.
247. Yu, R., and Zhou, T. (2004). Impacts of winter-NAO on March cooling trends over subtropical Eurasia continent in the recent half century. *Geophysical Research Letters*, 31(12), doi:10.1029/2004GL019814.
248. Zhang, W., Jin, F. F., Zhao, J. X., Qi, L., and Ren, H. L. (2013). The possible influence of a nonconventional El Niño on the severe autumn drought of 2009 in Southwest China. *Journal of Climate*, 26(21), 8392-8405.
249. Zhang, W., Wang, L., Xiang, B., Qi, L., and He, J. (2015). Impacts of two types of La Niña on the NAO during boreal winter. *Climate Dynamics*, 44(5-6), 1351-1366.
250. Zeng, N. (2003). Drought in the Sahel, *Science*, 302(5647), 999-1000.
251. Zhao, M., I. M. Held, S.-J. Lin, and G. A. Vecchi (2009). Simulations of global hurricane climatology, interannual variability, and response to global warming using a 50-km resolution GCM. *Journal of Climate*, 22(24), 6653-6678.
252. Zhang, D., Blender, R., and Fraedrich, K. (2013). Volcanoes and ENSO in millennium simulations: Global impacts and regional reconstructions in East Asia. *Theoretical and Applied Climatology*, 111(3-4), 437-454.
253. Zhou, Y. P., Xu, K. M., Sud, Y. C., and Betts, A. K. (2011). Recent trends of the tropical hydrological cycle inferred from Global Precipitation Climatology Project and International Satellite Cloud Climatology Project data. *Journal of Geophysical Research: Atmospheres*, 116(D9), 1-16
254. Zambri, B., LeGrande, A. N., Robock, A. and Slawinska, J. (2017). Northern Hemisphere winter warming and summer monsoon reduction after volcanic eruptions over the last millennium. *Journal of Geophysical Research: Atmospheres* 122, 7971-7989.

## Appendices

### A. Post-eruption QBO Impact and Limitation of This Study

We note a few caveats and possibilities for improvements to this study. We considered the major modes of climate variabilities (ENSO, NAO and Indian monsoon) that strongly affect MENA region. There are, however, few other modes that could potentially affect MENA climate, e.g., post-eruption phases of Indian Ocean Dipole (IOD) and quasi-biennial oscillation (QBO).

It has been argued in earlier studies that the stratospheric QBO could modulate the strength of polar vortex (Baldwin et al., 2001; Stenchikov et al., 2006), which in turn controls the NAO phase and associated surface climate. Post-eruption NAO circulation changes therefore could be linked with this QBO phases. Although the NAO and ENSO indices considered here potentially include the effect of QBO. However, this requires a separate experiment to determine post-eruption QBO role in global and regional climatic changes, and therefore this research work could be extended in this direction to find the role of QBO in modulating NAO or ENSO circulations and associated impact on the climate variability, especially in the MENA region. Therefore, the simulations in this study should be extended with experiments that could account for the effect of QBO, as it changes due to the post-volcanic atmospheric response (e.g., Thomas et al., 2009) and its self-modulation by strong volcanic eruptions (Aquila et al., 2014). For this purpose, one needs to use coupled model with very high top, to fully account for QBO strength. Another aspect is that the QBO phase during which an explosive volcanic eruption happens may have a huge importance on the e-folding time of the aerosol cloud and on its zonal distribution. Together with the magnitude, this might help to predict what kind of climatic impact a future eruption might have on the global and regional climate. The importance of the QBO-aerosol cloud interaction might also be rather important when considering sulfate geoengineering experiments.

### B. Robustness of Climate Responses using Multiple Regression Analysis

To further support the robustness of the residual approach that is implemented to see the volcanic direct impact in the MENA region (Section 4.4.5.3 and Section 4.4.6.3), this appendix provides additional analysis in which I included the volcanic AOD index as a predictor of the multiple regression analysis along with with other predictors (i.e., ENSO, NAO and ISM). The AOD index is the total stratospheric aerosol optical depth (AOD) at 550 nm as a function of time, zonally averaged over the MENA region (Figure 4.1). I computed the AOD-index-regressed anomalies averaged over the two post-eruption winter or summer seasons following both eruptions (Figures

S1 & S2). The spatial pattern of volcanic impact both in the UDEL and HIRAM model is largely similar to the results using the residual component (Figures 4.8 & 4.11). There is, however, a slight magnitude difference, which is possibly because of the correlation between the ENSO, and AOD index due to which they could somehow fetch some signal of each other. This magnitude difference could also be accounted for by some contribution coming through internal variability due to the climate forcing factors that are not included in multiple regression analysis. Keeping in mind this multicollinearity constraint, I preferred residual approach in this study. The similarity among the results produced by two different approaches lends support that the residual approach is effective.

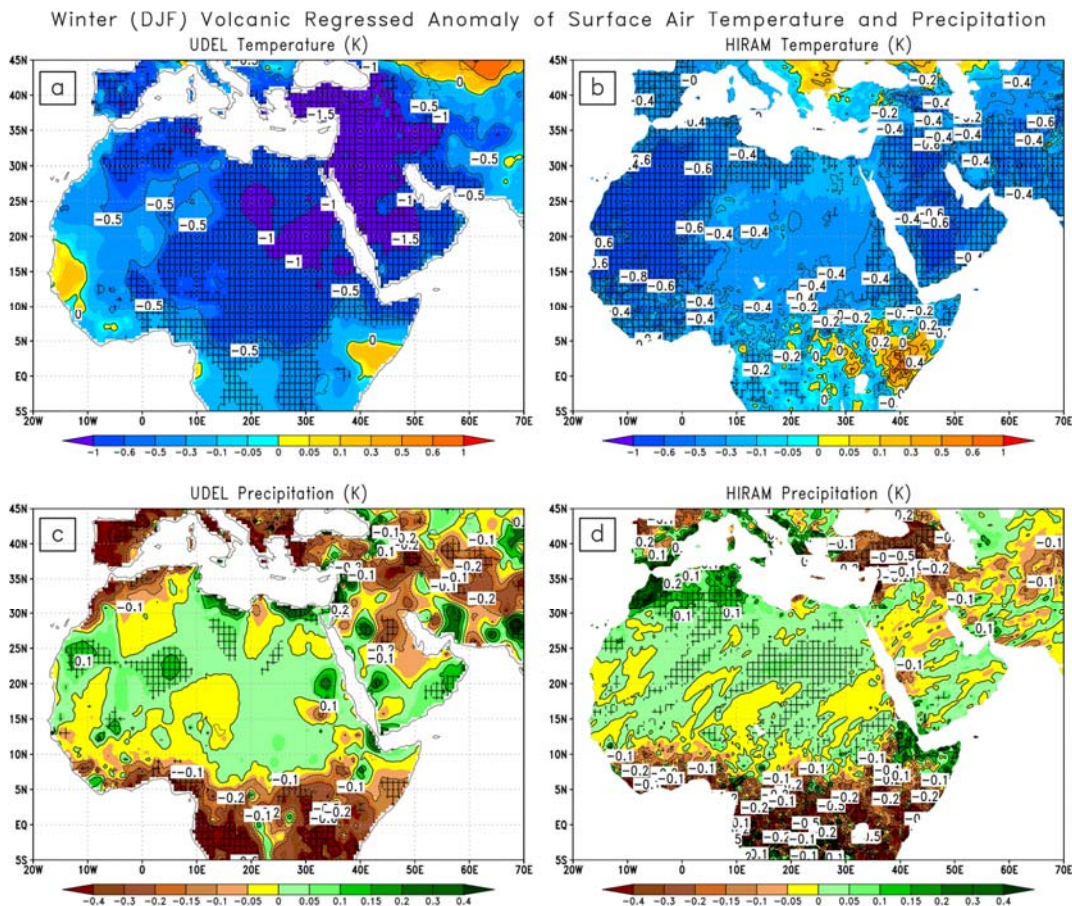


**Figure S1:** Anomalies of AOD-index-regressed surface air temperature (K) and precipitation (mm/day) composited over two winter (DJF) seasons after both the El Chichón and Pinatubo eruptions. The temperature composites are calculated using a) UDEL observations, b) HiRAM output, and precipitation composites using c) UDEL observations, d) HiRAM output. Hatching shows the statistically significant areas with at least 95% confidence level examined by bootstrapping with replacement test.

Summer (JJA) Volcanic Regressed Anomaly of Surface Air Temperature and Precipitation

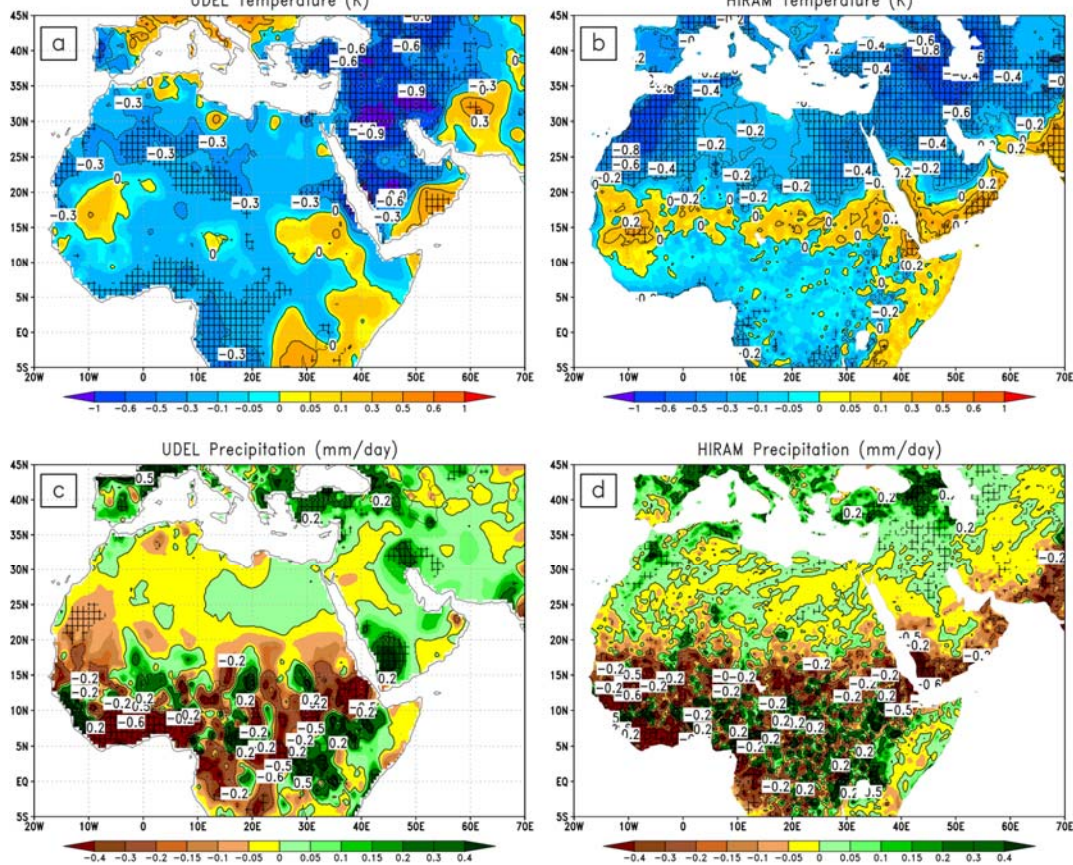


Figure S2: Same as in Figure S1 but for summer (JJA) season.